広島大学 学位論文

Film growth by aerosol deposition method and powder synthesis by mechanochemical solid-state reaction for ferroelectric lead-containing perovskites evaluated using synchrotron-radiation X-ray diffraction

放射光Ｘ線回折により評価した鉛を含むペロブスカイト型強誘電体のエアロゾルデポジション法による膜成長とメカノケミカル固相反応による粉末合成

2021 年

広島大学大学院理学研究科
物理科学専攻

Lin Wu

目　次

１．主論文

Film growth by aerosol deposition method and powder synthesis by mechanochemical solid-state reaction for ferroelectric lead-containing perovskites evaluated using synchrotron-radiation X-ray diffraction

Lin Wu

２．公表論文

Synthesis of Pb(Zr, Ti)O_3 fine ceramic powder at room temperature by dry mechanochemical solid-state reaction evaluated using synchrotron radiation X-ray diffraction.

Lin Wu, Sangwook Kim, Chikako Moriyoshi, Yoshihiro Kuroiwa, Muneyasu Suzuki, Kentaro Shinoda, Rintaro Aoyagi, and Jun Akedo:

Japanese Journal of Applied Physics **60**, SFFA02 (2021).

３．参考論文

Synchrotron radiation X-ray diffraction evidence for nature of chemical bonds in $Bi_4Ti_3O_{12}$ ceramic powders and grain-orientation mechanism of their films formed by aerosol deposition method.

Tomohiro Abe, **Lin Wu**, Chikako Moriyoshi, Yoshihiro Kuroiwa, Muneyasu Suzuki, Kentaro Shinoda, Rintaro Aoyagi, and Jun Akedo,

Japanese Journal of Applied Physics **59**, SPPA04 (2020).

主論文

Abstract

Ferroelectric perovskite materials are nowadays one of essential components for functioning of many electronic parts involved with the electrical products. Since lead-containing ferroelectrics such as Pb(Zr, Ti)O_3 (PZT) exhibit excellent piezoelectric properties, although there are concerns about their negative impact on the environment, they are widely used as a film or ceramic form in industries. Various methods have been proposed for fabricating lead-containing perovskite ceramics and their films, such as sol-gel reaction, spray drying, conventional solid-state reaction, chemical vapor deposition and hydrothermal method, etc. In this study, the film growth and powder synthesis for ferroelectric lead-containing perovskites fabricated using mechanical energy are evaluated using synchrotron-radiation X-ray diffraction (SXRD). The mechanism of film growth and the validity of powder synthesis have been revealed by the state-of-the-art SXRD method.

Firstly, many studies of $PbTiO_3$ (PT) films, which is the end members of PZT, have been conducted to understand the properties of non-solid-solutions. However, the mechanism of the film growth has not been sufficiently understood. In this work, PT film was fabricated by the aerosol deposition (AD) method on a glass plate to evaluate the film growth. The AD method enables us to coat metal or glass materials with thick and dense ceramics at room temperature (RT). In the process, fine powder mixed with gas, which form an aerosol, are sprayed through a nozzle to form the polycrystalline film. The preferred orientation along *c*-axis of PT AD film was detected by SXRD experiments at RT in the as-deposited state. According to the electron charge density distribution study, the tetragonal PT powder has a layered structure consisting of two-dimensional (2D) covalent bonding network, stacked along the *c*-axis at RT. We consider that the preferred orientation of the PT AD film is attributed to the layered characteristics. The weak bonds of PT between layers easily give rise to cleavage or deformation between layer-to-layer. The highest probability of recombination occurs when the particles of PT film recombine and grow with the unique 2D interfaces in the AD process, resulting in PT film exhibiting a *c*-axis oriented at RT without any post-annealing. Once the PT film was heated up to 1000 K in the paraelectric phase with the cubic structure, the *c*-axis orientation observed at the as-deposited state disappears at 1000 K and at RT after heating owing to the degree of freedom of the crystal axis on the phase transition. Therefore, we provide direct experimental evidence that the film growth is due to the layered structure of PT at RT. To validate the aforementioned analysis of the film growth, $Bi_4Ti_3O_{12}$ (BiT) film deposited by the AD method has been studied. SXRD experiments demonstrate that the BiT film with the preferred orientation along the *c*-axis is formed not only at the as-deposited state but also at 1100 K and RT after heating. The electron density distribution study of the BiT powder is conducted, revealing that the crystal structure of BiT powder is layered structure consisting of 2D covalent bonding network, stacked along *c*-axis at RT (the ferroelectric phase) and 1100 K (the paraelectric

phase). Thus, we concluded that the particles of PT film preferentially recombine and grow with the 2D interface (the *ab* plane) at RT due to the layered structure of PT stacking along the *c*-axis.

In another hand, fine ferroelectric perovskite ceramic powder, lead zirconate titanate PZT, was synthesized by mechanochemical solid-state reaction. Mechanochemical solid-state reaction is activated by mechanical energy rather than thermal energy required in the conventional process, thus, has attracted extensive research interest as an environmentally friendly method of synthesis at RT without any post-annealing. SXRD experiments were conducted to examine the validity of PZT synthesis from a mixture of $PbZrO_3$ (PZ) and PT powders by the mechanochemical solid-state reaction using dry ball milling at RT. The starting powder is consisting of a mixture of PZ and PT powders with a molar ratio of 1 : 1. Based on the observation of scanning electron microscope-energy dispersive X-ray spectroscopy (SEM-EDX), the red (PT powder) and green (PZ powder) were transformed into yellow area in the ball-milled samples. To confirm the yellow area was composed of PZT phase or a mixture of fine PZ and PT particles, the crystal structure of the ball-milled samples have been successfully investigated by analyzing the SXRD data using the Rietveld method, revealing that the yellow in SEM-EDX is composed of PZT phase. The powder synthesis by mechanochemical solid-state reaction was mostly completed in a considerably short time of 4 h. In the 8 h sample, only a single phase of PZT with a composition of $Pb(Zr_{0.485(1)}Ti_{0.515(1)})O_3$, can be detected. Considering that there is almost no composition deviation in the ball milling process, we hypothesize that PZT with any Zr/Ti composition we want can be synthesized by changing the molar ratio of PZ and PT powders.

In addition, the spontaneous lattice strain of PT film deposited by the AD method at RT is smaller than that of the starting powder. However, the phase transition temperature (T_C) is 100 K higher than that of the powder in the first heating process from the as-deposited state. It has been found that the PT film fabricated using mechanical energy stabilizes the ferroelectricity up to higher temperature, although the spontaneous polarization is suppressed. Similarly, the spontaneous lattice strain of PZT ceramic powder fabricated using mechanical energy is significantly smaller than that of PZT ceramic fabricated using thermal energy, and resembles a cubic structure even at RT. Additionally, the T_C is 100 K higher than that of PZT ceramic fabricated using thermal energy in the first heating process from the as-synthesized state. Therefore, we consider that ferroelectric materials fabricated using mechanical energy mainly may have common properties of low ferroelectricity but higher T_C.

Contents

Chapter 1

Introduction

1.1 Mechanochemical solid-state reaction

Mechanochemical reaction was originally invented to improve the mechanical properties of alloys, such as strength and wear resistance, which are achieved by mechanical activation derived from mechanical forces.[1,2] The widely accepted definition of mechanochemistry is that the mechanochemistry is the branch of chemistry that studies the chemical and physicochemical changes in various aggregation produced by mechanical activation energy.[1] The mechanochemical reactions produce changes in the composition, morphology or structure of the reactants. The process of mechanochemistry is complicated, including the accumulation of defects, forming new surface and recombination, etc. Several theories and models have been considered in the past years to understand the mechanism of the mechanochemical reaction, such as hot-spot theory, the magma-plasma model, the theory of short-living active centers and kinetic model, etc. Although the reaction temperature of mechanochemical solid-state synthesis is at room temperature, the theoretical simulation revealed that this process is not only in mechanical but also in combination with thermal activation.[1] They suggest that the surface atoms of particle powder generate instantaneous high temperature and pressures under the mechanical forces of other powders or media.

Subsequently, the mechanochemical solid-state reaction was introduced in the synthesis of organic,[3,4] polymer,[5] and oxides,[6,7] etc. In particular, this method has been widely used in the synthesis of complicated oxides because of its advantages of room temperature reaction and free post-treatment. The synthesis of perovskite compounds has attracted extensive interest due to the unique dielectric, piezoelectric, ferroelectric and thermoelectric properties of lead-based perovskite materials such as $PbTiO_3$, $PbMg_{1-x}Nb_xO_3$ and $Pb_{1-x}Sr_xTiO_3$.[1,8] There are many methods of their synthesis, including solution-based synthesis,[7] hydrothermal process,[9] sol-gel process,[10] chemical vapor deposition,[11] electron/ion beam evaporation,[12] rf magnetron sputtering[13] and pulsed laser deposition,[14] etc. Compared to these means, the advantages of mechanochemical solid-state reaction are simplicity, one-step operation, low-cost and reaction at room temperature.[6-8]

1.2 Ferroelectric $PbTiO_3$ and $Bi_4Ti_3O_{12}$

Ferroelectric materials mean that these materials possess spontaneous polarization and will change their polarization direction to along the direction of electric field when were imposed by an external electric field.[15-18] From an energy viewpoint, ferroelectric materials directly transfer the electrical energy from the applied electric field to the mechanical energy we want to obtain. The ferroelectricity comes from the dipole and non-centrosymmetric crystal structure in the materials.[18] Because of the ferroelectricity, these materials can be widely used in electronic devices and micro-systems, such as sensors, transducers, actuators.[19-24] The first discovery of ferroelectric material is single crystal Rochelle salt in 1921.[18,25] Then, starting from the early 1940s, the most important types of ferroelectric material groups were discovered, the perovskite group,[26] the tungsten-bronze,[27] and the Aurivillius group.[18] Here, we will introduce two typical kinds of ferroelectric materials, that is, perovskite $PbTiO_3$ and Aurivillius $Bi_4Ti_3O_{12}$.[28,29] Hereinafter, we briefly explain the meaning of perovskite and Aurivillius as you can see anywhere.

Firstly, perovskite material, named from $CaTiO_3$ mineral,[30] is one of the most widely used materials in modern society because of its excellent properties derived from the crystal structure and related electron distribution. Therefore, material with a chemical formula ABX_3 usually is described as a perovskite material. The A and B sites, named as cation atoms, are generally occupied by alkaline/alkali and transition metal ions, respectively. Herein, A sites with larger ions size while B sites with smaller ions size. Other hand, the X sites, named as anion atoms, are oxygen ions or halide ions. For most perovskite materials, the prototype crystal structure is a cubic phase with $Pm\bar{3}m$ space group. In this crystal, the A site is located at the special Wyckoff position of (0, 0, 0) and the related equivalent positions are occupying the eight corners of this crystal. At the same time, the B site occupies the body center of this crystal, (1/2, 1/2, 1/2), while six X sites occupy the face center of this crystal, (1/2, 1/2, 0).[28]

On the other hand, the Aurivillius materials are the oxides with the general formula $(Bi_2O_2)^{2+}(A_{n-1}B_nO_{3n+1})^{2-}$, which are composed of perovskite-like $A_{n-1}B_nO_{3n+1}$ units and Bi_2O_2 layers.[31-35] Here, the A sites are alkali or alkaline earth cation ions while B sites are transition metal ions. Then, the details of two typical materials, $PbTiO_3$ and $Bi_4Ti_3O_{12}$, will be introduced in next section.

1.2.1 Crystal structure and phase transition of $PbTiO_3$ and $Bi_4Ti_3O_{12}$

Crystal structure and phase transition of $PbTiO_3$

$PbTiO_3$ and $BaTiO_3$ are most typical perovskite structure ferroelectric materials up to now.[28] In 1950, Slater first studied the ferroelectricity of $BaTiO_3$ and suggested that it come from the ionic polarization of Ti atom.[36,37] To honor the contribution of Slater, the polarization type of $BaTiO_3$ is named Slater mode. Since the 1990s, the important roles of the electronic structures of these materials in ferroelectricity has been investigated by *ab initio* calculations, as Cohen pointed out that the covalent bonding of Pb-O and Ti-O derived from the hybridizations between Pb and O and between Ti and O electron orbitals will lead to the polarization of $PbTiO_3$.[38] Then, Kuroiwa et al. first provided experimental evidence that the Pb-O bond is covalent state in tetragonal $PbTiO_3$ at room temperature. So far, there is enough information on the origin of ferroelectricity of $PbTiO_3$ for our basic research and industrial applications.[28]

The cations in perovskite structure can be widely used in the metallic elements in the periodic table, such as Pb, Ba, Bi, Fe, Zr, Ti, Mn, Co, Ni, Zn, etc. The cation sites (*A* site and *B* site) occupied by different elements exhibit different physical, chemical properties and thermal stability.[39-41] There are many reasons to explain this phenomenon, especially for ions radii and electron structure, such as valence balance and ionic/covalent states for electron structures. However, elucidating perovskites in terms of their electronic structure is not a quick and easy way. Therefore, the tolerance factor *t* was extracted to describe the structural stability in a simple method, providing an empirical formula. The ions radius of *A* site, *B* site, and O ion are labelled as R_A, R_B, and R_O, respectively. According to the geometric correlation of ideal cubic phase, there is a simple relationship among the radius:$R_A + R_O = \sqrt{2}(R_B + R_O)$. Then, this formula can be rewrite as follow:

$$t = \frac{R_A + R_O}{\sqrt{2}(R_B + R_O)}. \tag{1-1}$$

The tolerance factor *t*[42,43] for an ideal cubic symmetry is 1. Most actual perovskite material in nature have tolerance factors that can't perfectly match the value of 1 and will deviate this value. Explaining this deviation of the actual tolerance factor from the ideal value of 1 in terms of crystal distortion and octahedral skewing has a key role; crystal distortion and octahedral skewing reduce the geometric symmetry in the perovskite crystals. Generally, the value of the tolerance factor greater than 1 indicates that there is a spatial clearance around the *B* site, while smaller than 1 implies that there is a spatial clearance around the *A* site. For the $PbTiO_3$ perovskite, the value of R_A, R_B, and R_O calculated with 12, 6, and 2 coordination, are 1.49, 0.605, and 1.35 Å, respectively. Thus, the value of tolerance factor *t* can be calculated as 1.027, which means that there is a spatial clearance around the *B* site.

Next, crystal structure and related phase transition will be described in detail. As mentioned above, the prototype crystal structure of $PbTiO_3$ is $Pm\bar{3}m$ at high temperature, and the related schematic diagram is shown in Fig. 1-1 (a). In this crystal structure, the lattice parameters along the directions of *x*, *y*, and *z* have the same value of about 3.98 Å. Here, the six oxygen atoms occupy the equivalent positions at a cubic phase, which will lead to six Ti-O bonds in the same. Therefore, there is no ferroelectricity at cubic phase, which is named as paraelectricity. As the temperature decreases, a phase transition from the cubic to the tetragonal phase occurs at about 763 K.[44-46] Below this temperature of 763 K, if the position of Pb is assumed to be the original position, Ti and O will be displaced along the *c* direction, resulting in two kinds of Pb-O bonds, named Pb-O1 and Pb-O2, and two kinds of Ti-O bonds, also called Ti-O1 and Ti-O2, respectively. In this condition, the centrosymmetry in the cubic phase will be broken, leading to non-centrosymmetry in the electron and lattice distributions, resulting in dipoles and polarizations that exhibit ferroelectricity. Due to the displacement of the *c* direction, the lattice parameters along the *x* and *y* directions keep the same values, shorter than that of the *c* direction. To describe this special property, the tetragonality, i.e., the value of c/a, is extracted. Because the lattice parameter c is greater than a, the value of c/a usually is greater than 1. The larger value of c/a, the better tetragonality, indicating strong ferroelectricity. Here, the crystal structure of tetragonal $PbTiO_3$ is *P*4*mm* shown in Fig. 1-1 (b). At room temperature, the lattice parameter a is about 3.9 Å, while c is about 4.15 Å, indicating a tetragonality of about 1.065. According to the assumption, the atom position of Pb also remains at (0, 0, 0), while the Ti ion occupies (1/2, 1/2, 1/2 + δ), where δ means the displacement of the Ti ion. At the tetragonal phase, six oxygen ions split into two kinds of oxygen atoms because of the chemical atmosphere, named O1 and O2. Four oxygen atoms, called O2, are parallel to the *ab* plane and two O1 atoms parallel to the *c* direction.

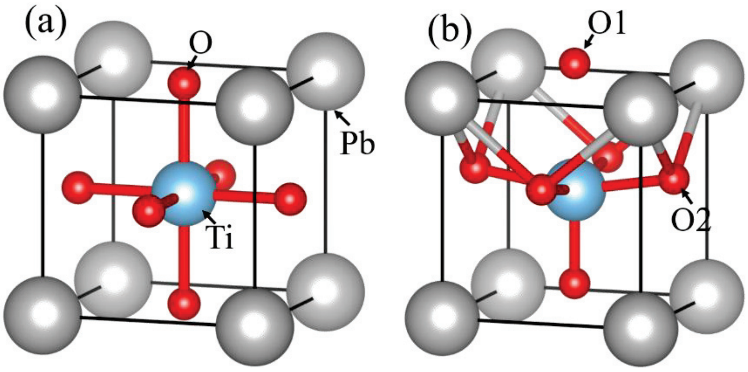

Fig. 1-1 Schematic image of (a) cubic and (b) tetragonal $PbTiO_3$.

As mentioned above, from high to low temperatures, the paraelectricity disappears and ferroelectricity appears in $PbTiO_3$. Among this process, what should be emphasized is volume shrinkage in ferroelectric phase.[47,48] From room temperature to phase transition temperature, Curie temperature T_C, the $PbTiO_3$ material exhibits the negative thermal expansion (NTE) phenomenon over this wide temperature range. This special phenomenon, NTE, is an intriguing property in condensed matter physics and a valuable application in functional materials. According to many published literatures, especially in recent years, it is revealed that the NTE comes from the hybridization between the 3d electron orbital of the Ti ion and the 2p orbital of O and between the 6s orbital of Pb and the 2p orbital of O, which lead to a strong covalent bonding of Ti-O1(and Ti-O2) and Pb-O2 and the related large polarization and ferroelectricity, resulting in the formation of NTE in tetragonal phase.[49,50] The stronger covalent bonds of Pb-O2 and Ti-O1 will cause a large NTE among the tetragonal temperature, especially when temperature is close to T_C.

The phase transition behavior of $PbTiO_3$ perovskite is different from that of $BaTiO_3$ and should be clearly pointed out here, although they are both typical perovskite materials. To clearly explain the difference between these two kinds of perovskite materials, a "soft mode" should be introduced. As the temperature cools, from the high symmetry phase (cubic phase) to the low symmetry phase (tetragonal phase), the phonon is softened, i.e., the fundamental vibrational frequency decreases. Here, the soft fundamental vibration is named "soft mode". From physical viewpoint, there are two kinds of soft modes, one is at the center of the Brillioun zone, named Γ_{15} mode, and the another one is at the boundary of the Brillioun zone, called M_3 and R_{25}. Here, as shown in Fig. 1-2, the notation of Γ, M, and R means that the phonon contributions come from the corresponding reciprocal point in the Brillioun zone.

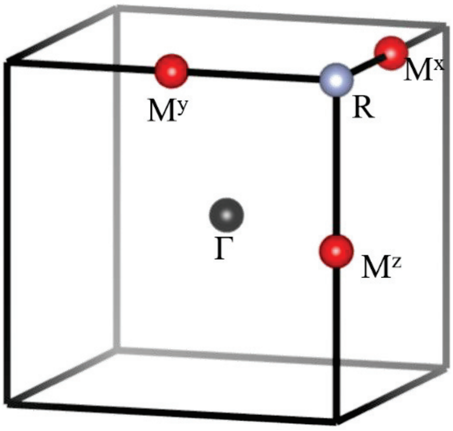

Fig. 1-2 The center and boundary point in Brillouin zone of cubic perovskite phase.

The center point of the Brillioun zone, Γ_{15}, is the optical wave mode. With the soften and frozen in this mode, the atomic displacement gives rise to along the direction of the *c* axis, that is [001] direction, resulting in a phase transition. In this mode, there are three kinds of displacement patterns along [001] direction, as shown in Fig. 1-3. As mentioned above, due to the contribution of Slater in $BaTiO_3$, the phase transition from cubic to tetragonal of $BaTiO_3$ was named Slater mode.[36] In Slater mode, as plotted in Fig. 1-3(a), the displacement direction of oxygen and *B* site ions are opposite along the *c* axis. Due to the same reason, to honor the contribution of Last and Axe in Γ_{15} mode, the last two patterns was called Last mode and Axe mode, respectively.[51] In the Last mode, as plotted in Fig. 1-3(b), the *B* site ions and oxygen ions are displaced along the same direction, while the *A* site ions are displaced in the opposite direction. It is important to emphasize here that the displacement of the oxygen octahedron BO_6 is opposite to that of the O ion because the displacement of *B* ion is shorter than that of the O ion. In the Axe mode shown in Fig. 1-3(c), the two kinds of oxygen, O1 and O2, are displaced in opposite directions along the [001] direction.

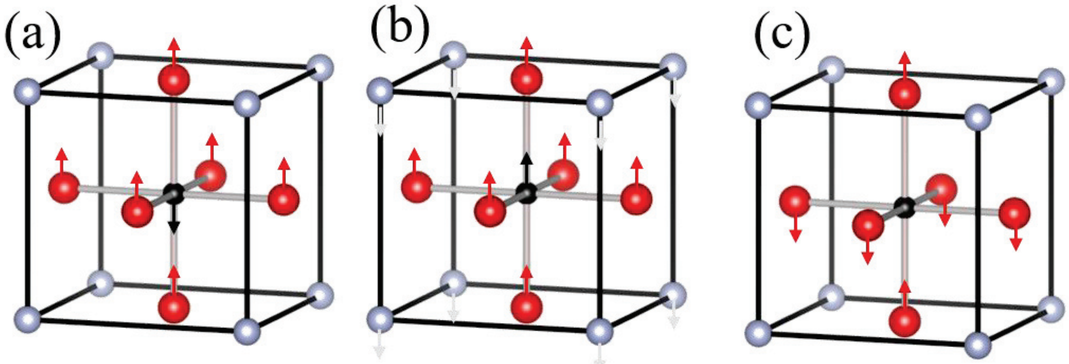

Fig. 1-3 Atomic displacement patterns of (a) Slater mode, (b) Last mode, and (c) Axe mode when Γ_{15} is soften and frozen.

$BaTiO_3$ is the Slater mode, while $PbTiO_3$ is a combination of the Slater mode and the Last mode, which is different from $BaTiO_3$. Due to the difference in Γ_{15} mode during phonon softening and freezing, $BaTiO_3$ and $PbTiO_3$ show different phase transition behaviors when the temperature decreases from high to low. In $BaTiO_3$, there is a successive phase transitions from the cubic to tetragonal, orthorhombic, and rhombohedral with temperature decreasing through 403, 278, and 198 K.[52] However, only one phase transition for $PbTiO_3$ gives rise to at 763 K from cubic to tetragonal phase. To analyze the origin of the different behavior between $PbTiO_3$ and $BaTiO_3$, Abe et al. investigated the valence charge density distribution of $PbTiO_3$ and $BaTiO_3$ and pointed out that the presence of covalent state in Pb-O2 bond and ionic state in Ba-O2 bond is due to the large electronic polarization in Pb derived from its lone-pair electron in p-like orbital in $PbTiO_3$, as shown in Fig. 1-4.[52]

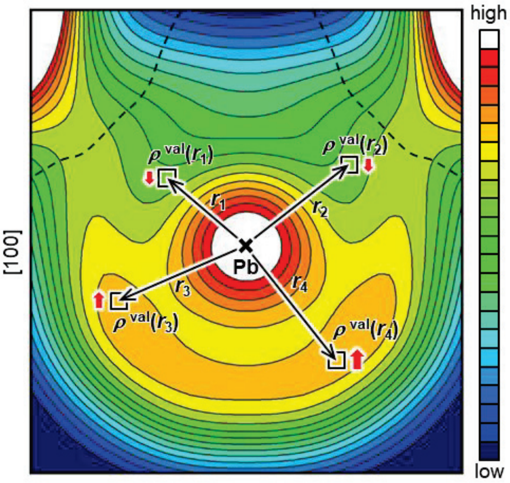

Fig. 1-4. Schematic image of the dipole moment of the Pb atom in tetragonal $PbTiO_3$.[52]

Crystal structure and phase transition of $Bi_4Ti_3O_{12}$

Ferroelectric material $Bi_4Ti_3O_{12}$, which has the physical properties of Aurivillius phase, has been reported in many studies.[35,53] In the Aurivillius phase, the perovskite-like $A_{n-1}B_nO_{3n+1}$ units and Bi_2O_2 layers stack along the c direction to form the crystal structure. For $Bi_4Ti_3O_{12}$ ferroelectric material, the n in the formula of $(Bi_2O_2)^{2+}(A_{n-1}B_nO_{3n+1})^{2-}$ is 3, while A site and B site are Bi and Ti ions, respectively, indicating there are three units of perovskite-like in this crystal structure. The prototype structure of $Bi_4Ti_3O_{12}$ is tetragonal phase with the space group $I4/mmm$ at high temperature displayed in Fig. 1-5.[53] At high temperature, the mirror plane of the prototype parent structure is perpendicular to and through the center of the c axis, resulting in no spontaneous polarization along [001] direction. Since the other mirrors are perpendicular to [100] and [110] directions, the prototype crystal structure exhibits a paraelectric characteristic at tetragonal phase, which is different from $PbTiO_3$ which has ferroelectric properties at tetragonal phase. Due to the stacking of perovskite-like units and Bi_2O_2 layers along the [001] direction, the lattice parameter c_T is much larger than a_T (b_T), where the subscript "T" indicates tetragonal phase. According to the symmetric operation of $Bi_4Ti_3O_{12}$ at tetragonal phase, the lattice parameter a_T is equal to b_T, about 3.86 Å, while lattice parameter c_T is about 33.3Å. In this condition, there are two kinds of Bi ions, in the ionic (labelled Bi(1)) and covalent state (labelled Bi(2)), and two kinds of Ti ions, in the 6-fold oxygen coordination (labelled Ti(1)) and 5-fold oxygen coordination (labelled Ti(2)), respectively. Specially, in tetragonal $Bi_4Ti_3O_{12}$, there are 5 kinds of oxygen ions. In $Ti(1)O_6$ octahedron, the four oxygen ions perpendicular to the c axis are labelled O(1) and the other two parallel to the c axis are labelled O(3). In $Ti(2)O_5$ octahedron, the four oxygen ions perpendicular to the c axis are labelled O(5) and the other oxygen ion is labelled O(4). In $Bi(2)O_4$ tetrahedron, these four oxygen ions are labelled O(2).

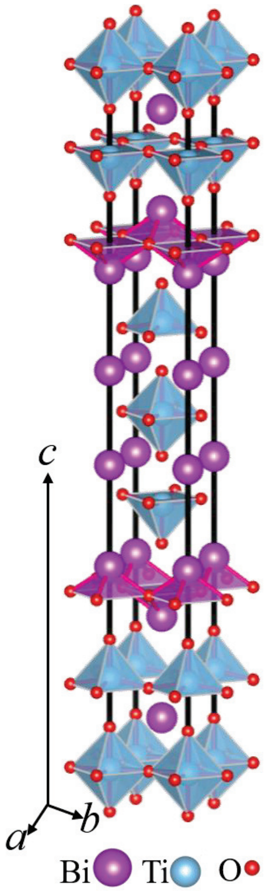

Fig. 1-5 Polyhedral model of tetragonal $Bi_4Ti_3O_{12}$.

As the temperature decreases from high to low, the symmetry of the crystal structure reduces from tetragonal with space group *I*4/*mmm* to orthorhombic with space group *B*2*cb* at about 695 ℃ (968 K).[35] Among this phase transition process from *I*4/*mmm* to *B*2*cb*, a complex combination of atomic displacements and octahedral tilting occurs, resulting in ferroelectric phase at room temperature. However, some evidences from group theory, first-principles calculations, symmetry operation analysis, and experimentally observations of high-resolution synchrotron radiation or high-resolution powder neutron diffraction suggest that atomic displacement and octahedral tilting cannot occur at the same time and reveal that an intermediate phase connecting *I*4/*mmm* and *B*2*cb* should exist.[53,54] Therefore, the intermediate phase presented by Qingdi Zhou et al. is the ferroelectric orthorhombic phase with a space group of *Fmmm* in a narrow temperature range of 695 ~ 670 ℃ (below Curie temperature), while the tetragonal paraelectric phase with a space group of *P*4/*mbm* at about 685 ℃ (above Curie temperature) is proposed by Yuanyuan Guo.[35,53] In their literature, the Curie temperatures determined were 695 and 675 °C, respectively, due to the different experimental methods of Qingdi Zhou and Yuanyuan Guo.

Ferroelectricity with a spontaneous polarization direction along [100] direction occurs at room temperature due to the displacement of Bi ions along [100] direction and the tilting of TiO_6 octahedral. The spontaneous polarization P_S is about 50 μC/cm^2 along [100] direction. By hysteresis experiments, a small P_S value of about 4 μC/cm^2 was observed along the [001] direction.[31] To explain this phenomenon, some researchers have proposed that the crystal structure of $Bi_4Ti_3O_{12}$ is monoclinic at room temperature, however, J. F. Dorrian et al. suggested that the lone-pair electrons of Bi(1) are being reoriented to induce the polarization along c-axis.[31]

At room temperature, the crystal structure of $Bi_4Ti_3O_{12}$ is orthorhombic with space group of $B2cb$. The tilt of TiO_6 octahedral can be notated as $a^-a^-c^0$ in Glazer notation. The Glazer notation system describes the rotation of octahedral using three axes. For example, the $a^-a^-c^0$ notation of $Bi_4Ti_3O_{12}$ indicates (1) the same rotation about a-axis and b-axis and no rotation about c-axis, and (2) the superscript "-" exhibit the opposite rotation between the adjacent octahedral. Due to the characteristics of tilt of TiO_6 octahedral, the $\boldsymbol{a}_O$ and $\boldsymbol{b}_O$ axes of the orthorhombic structure need be rewrite as $\boldsymbol{a}_T + \boldsymbol{b}_T$ and $\boldsymbol{a}_T - \boldsymbol{b}_T$, respectively,[32] where the subscript "T" means the tetragonal phase. That is, the lattice parameter of orthorhombic phase, $a_O \approx b_O \approx \sqrt{2}a_T, c_O \approx c_T$. Due to the different bond lengths of the Ti(2)-O(5) and Ti(2)-O(6) bonds, the oxygen labeled O(5) at the tetragonal phase will split into two types of oxygen labeled O(5) and O(6) at the orthorhombic phase.[34] To describe the degree of deviation between the lattice parameters a and b, the orthorhombicity factor is proposed as $2\frac{a-b}{a+b}$, where a was defined as greater than b. The value of orthorhombicity indicates the orthorhombic distortion, and a larger value means greater distortion. Generally, for $Bi_4Ti_3O_{12}$ at room temperature, the orthorhombicity value is about 7×10^{-3}.

1.2.2 Aerosol deposition (AD) method

Ferroelectric materials are widely used in modern society, such as ferroelectric memories, piezoelectric devices, micro sensors, etc. Specially in micro devices, ferroelectric material will be coated as thin films on the surface of these devices. In the last two decades, ferroelectric thin films have attracted significant interest not only in industrial applications, but also in fundamental research.[55-58] To meet the dramatically increasing demand for ferroelectric thin films, various means such as chemical, physical, and bio-physical methods have been investigated. Including chemical vapor deposition, physical vapor deposition, electron/ion beam evaporation, sol-gel method, rf magnetron sputtering, pulsed laser deposition, hydrothermal method, and metalorganic chemical vapor deposition, etc.[21,24,55,59-69]

Among them, although they have many aspects of excellent performance in the deposition of ferroelectric thin films, most of them require a temperature risen to between 500 and 800 °C, which constrains the rapid industrialization of ferroelectric thin film applications. Recently, Jun Akedo et al. developed a new method for depositing thin films or dense ceramics at room temperature using mechanochemical solid-state reaction without any post-heat treatment, which was named aerosol deposition (AD) method.[70-75]

This mechanochemical solid-state reaction, i.e., the AD method, as shown in Fig. 1-6,[76] provides a synthetic method with simplicity, low-cost, solvent-free, and no heat treatment history. In this process, starting powders with particle sizes between submicron and several microns are first mixed with a gas, such as He, N_2, and air, to generate an aerosol in the aerosol chamber. Next, accelerated by the pressure difference derived from the low pressure (0.05 ~ 2 kPa) in the deposition chamber caused by the vacuum pump, the aerosol is ejected at a speed of 100 to 500 m/s through a nozzle with a rectangular-shaped orifice of 10 mm × 400 μm size to impact vertically onto the substrate. The distance between the substrate and the nozzle orifice is 1 to 40 mm. At the same time, the substrate stable moves along the *xy*-stages to form a scan area, which is named deposited area.

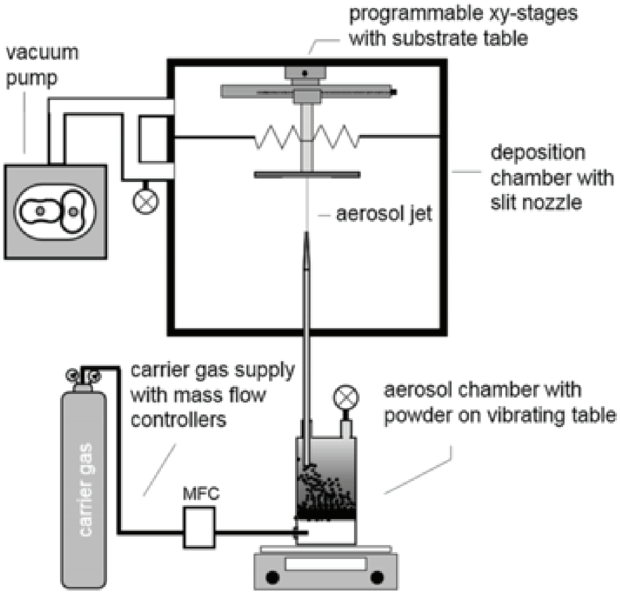

Fig. 1-6. Schematic imagine of AD method.[76]

Submicron starting powders are impacted on a substrate to generate dense and hard thin films or ceramics at room temperature by the AD method. The grain size of as-deposited thin films or dense ceramics is about 100 to 200 nm, which is a great smaller than that of the starting powders. During this impact process, the kinetic energy is converted into thermal energy and mechanical energy. The thermal energy drives the temperature up, softening the surface of the particles and producing the plastic flow between the particles and the substrate and at the point of collision between the particles and the particles. At the same time, the instantaneous high-stress at the collision-point exceeds the hardness of the particles, causing them to break into small pieces of grain sizes. Due to this process deposited at room temperature, Akedo et al. named this unique phenomenon “room temperature impact consolidation”.

Since the new approach for depositing thin films by AD method is proposed by Akedo et al., many related researches in ferroelectric material have been investigated. Initially, Akedo et al. investigated the synthesis of Al_2O_3 and TiO_2 materials by AD method. Among these two types of materials, Al_2O_3 and TiO_2 AD films exhibit high strength, dense, non-porous, smooth, and transparent properties compared to conventional means.[71,75,77] Then, this novel method, the AD method, was introduced into ferroelectric materials. Crack-free piezoelectric material $Pb(Zr_{0.52}Ti_{0.48})O_3$ films were formed on stainless-steel and $Pt/Ti/SiO_2/Si$ substrate by the AD method, and their mechanical and piezoelectric properties were comparable to those of other means of film deposition.[78] Nano size grains $PbTiO_3$ films with crack-free were deposited by the AD method and exhibited a greater high thermal stability than that of powders or bulk, indicating good performance for high temperature application. Also, the AD method can be used to synthesize films with dielectric properties, such as $BaTiO_3$, $PbTiO_3$, $(Pb_{0.91}La_{0.09})(Zr_{0.65}Ti_{0.35})O_3$, $(Bi_{0.5}Na_{0.5})TiO_3$, and $Bi_4Ti_3O_{12}$ materials. Compared to conventional methods, the AD films of $BaTiO_3$, $PbTiO_3$, $(Pb_{0.91}La_{0.09})(Zr_{0.65}Ti_{0.35})O_3$, and $(Bi_{0.5}Na_{0.5})TiO_3$, have enhanced dielectric property, electro-optical property, and polarization property, respectively.[70,79-81]

Up to now, the AD films of Pb-based ferroelectric perovskite-type materials have been widely studied, especially $PbTiO_3$ material.[45] One of the important reasons is to avoid the negative thermal expansion of $PbTiO_3$ materials during the phase transition. Among the AD method, the ferroelectric thin films can be deposited at room temperature without a phase transition, which is different from conventional means. In conventional means, such as sintering, $PbTiO_3$ ferroelectric thin films synthesized at high temperature, usually higher than 800 °C, and then cooling to room temperature. However, the large volume contraction at the phase transition from cubic to tetragonal phase makes it difficult to avoid generating crack in $PbTiO_3$ ferroelectric thin films. Therefore, the AD method has a great advantage in fabricating crack-free $PbTiO_3$ ferroelectric films, which avoid the large volume shrinkage during the phase transition because it is deposited at room temperature.

1.2.3 Purposes

$PbTiO_3$ ferroelectric thin films have been widely investigated, however, until now, the mechanism of the film growth has not been clearly revealed in $PbTiO_3$ thin films. Due to most $PbTiO_3$ thin films generated by various methods exhibit a *c*-axis preferred orientation, this intriguing phenomenon provides a clue for us to understand the film growth.

As shown in Fig. 1-7, XRD patterns of $PbTiO_3$ powders, $PbTiO_3$ thin films formed by RF-magnetron sputtering method at 10 Pa and at 1 Pa are plotted in Fig. 1-7(a), (b), and (c), respectively.[82] Because the lattice *a* and *b* are the same, the ratio of the intensity of (*h*00) and (00*h*) should be 2:1 for randomly orientation $PbTiO_3$ material, such as the powder sample shown in Fig. 1-7(a). However, as shown in Fig. 1-7(c), the intensity ratio of (100) and (001) in $PbTiO_3$ thin film is opposite to that of powder, that is, the intensity of the (001) diffraction peak is higher than that of the (100) peak. In addition, the intensity peak of the (101), (110), and (111) cannot be observed in $PbTiO_3$ thin film. These observations provide evidence of the *c*-axis preferred orientation in $PbTiO_3$ ferroelectric thin film.

This interesting phenomenon appears not only in the $PbTiO_3$ thin film deposited by RF-magnetron sputtering method, but also in the $PbTiO_3$ thin films deposited by metalorganic chemical vapor deposition, chemical vapor deposition, pulsed laser deposition and hydrothermal methods, etc.[67,83-85] For instance, $PbTiO_3$ ferroelectric thin films with (001)-orientation were synthesized on the substrate of $LaAlO_3$ at 650 °C using metalorganic chemical vapor deposition.[83] (001)-oriented $PbTiO_3$ ferroelectric thin films were deposited on the Pt-coated Si wafer substrate at a deposition temperature between 550 and 690 °C by chemical vapor deposition.[84] Sun-Hwa Lee et al. obtained *c*-axis oriented $PbTiO_3$ ferroelectric thin films formed on MgO (001) by the means of pulsed laser deposition.[67] In the hydrothermal method, $PbTiO_3$ ferroelectric thin films synthesized on the substrate of $SrRuO_3$ / $SrTiO_3$ (100) at 150 °C also exhibit the preferred orientation along *c*-axis.[85]

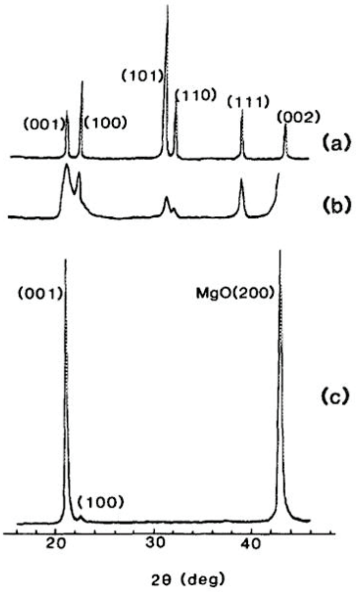

Fig. 1-7. XRD patterns of $PbTiO_3$ (a) powders and thin films formed at (b) 10 Pa and (c) 1 Pa.[82]

This unique phenomenon, preferred orientation along *c*-axis, not only occur at $PbTiO_3$ ferroelectric thin films synthesized by various means, but also in Pb-based ferroelectric perovskite-type materials, such as $0.67PbMg_{1/3}Nb_{2/3}O_3$–$0.33PbTiO_3$ thin films deposited on $LaNiO_3$-coated SiO_2/Si substrates by the RF magnetron sputtering technique.[86] Furtherly, recently, *c*-axis oriented ferroelectric thin films also were formed in $Bi_4Ti_3O_{12}$ material by AD method.[87]

Due to $PbTiO_3$ ferroelectric thin films deposited by various means exhibit the preferred orientation along *c*-axis, a strong coupled relationship between the preferred orientation and the film growth in $PbTiO_3$ is naturally considered. Therefore, understanding the origin of the preferred orientation in $PbTiO_3$ ferroelectric thin films is crucial to clarify the mechanism of the film deposition and growth in the deposited process. However, the origin of preferred orientation has not been effectively understood. For example, to explore the origin of this intriguing phenomenon, Suzuki et al. considered that the plate-shape particles of starting powders in $Bi_4Ti_3O_{12}$ material were an important factor in the synthesis of *c*-axis oriented AD films.[87] On the other hand, from the viewpoint of crystal structure, $Bi_4Ti_3O_{12}$ material also can be considered as a layered-structure material with alternating Ti-O layer and Bi-O layer along the *c*-axis.

Therefore, in this study, we focus on the crystal structure and related charge density distribution in *A*-O bond and *B*-O bond to extract the physical reason why the preferred orientation along the *c*-axis and then to further clarify the mechanism of film growth in $PbTiO_3$ ferroelectric thin films and $Bi_4Ti_3O_{12}$ ferroelectric thin films. The substrate of other published papers is single crystal or multi-coated, which has a significant impact on the deposited material. To avoid this effect, we choose the amorphous-state glass as the substrate. Thus, $PbTiO_3$ ferroelectric thin films are fabricated on a glass substrate by the AD method to evaluate the crystal structure, preferred orientation in the growth. Based on the same approach, $Bi_4Ti_3O_{12}$ AD thin films were studied to examine the validity of the film growth mechanism in $PbTiO_3$ AD films. The AD film is consisting of the film with several microns thickness and the glass substrate with several millimeters thickness. The thickness of the glass substrate is a thousand times higher than that of the film. In order to avoid the glass substrate effect during the synchrotron-radiation X-ray diffraction experiments, we peel the AD film from the substrate and call the film without substrate a "self-supported film" to perform a precise phase transition behavior experiment and study the structural characteristics. Here, we assume the self-supported film maintains the structural characteristics of the AD film. Based on the structural characteristics of the AD films and the chemical bonding of the starting powders, the mechanism of the film growth and the preferred orientation is discussed. We comprehensively studied the temperature-dependence of the structural characteristics to illuminate the origin of the phase transition behavior of the self-supported film.

1.3 Piezoelectric perovskite $Pb(Zr_{1-x}Ti_x)O_3$

Piezoelectricity refers to the ability of the material with non-center-symmetry to generate either an electric polarization proportional to the externally applied mechanical stress (named direct piezoelectric effect) or a mechanical strain proportional to the externally applied electric field (named inverse piezoelectric effect).[18] In terms of energy conservation, piezoelectric phenomena refers to the transfer of energy from mechanical to electrical energy (named direct piezoelectric effect) or from electrical to mechanical energy (named inverse piezoelectric effect). Therefore, the perovskite-type material with piezoelectric property are referred to as piezoelectric perovskite, such as $Pb(Zr_{1-x}Ti_x)O_3$, which is studied in this work.

The first piezoelectric material is quartz discovered by Curie brothers in 1880.[18] In piezoelectric material, some piezoelectric and related properties are important, such as dielectric permittivity, piezoelectric coefficient, frequency constant, which are widely used in modern society.

1.3.1 Ferroelectric $PbTiO_3$ and anti-ferroelectric $PbZrO_3$

Ferroelectricity is the material with spontaneous polarization that can be reoriented along crystallographic directions, such as [001], [100], and [111], when stimulated by an externally the applied electric field. In ferroelectric materials, the delicate balance between repulsion force and Coulomb interaction plays a key role in the favorable or unfavorable ferroelectric state. As last section mentioned, $PbTiO_3$ perovskite is a ferroelectric material in the tetragonal phase and a paraelectric material in the cubic phase. As the temperature decreases from cubic to tetragonal phase, the orbital hybridization between Pb (6s, 6p) electrons and O 2p electrons produced by Coulomb interactions and crystal field effects will shorten the bond length of Pb-O2 and form Pb-O2 covalent bonds when it is below the Curie temperature (phase transition temperature). The same phenomenon also occurs in Ti-O1 bond, where the hybridization between the Ti (3d, 4s) orbital electrons and O 2p electrons under the crystal field and Coulomb interaction leads to one shorter and one longer Ti-O1 bonds which is a strong covalent bond for the shorter Ti-O1 bond.

The crystal structure of $PbTiO_3$ perovskite is displayed in Fig.1-8. To clearly elucidate the origin of ferroelectricity in $PbTiO_3$, the Pb-O2 covalent bond and Ti-O1 covalent bond was specially extracted, as shown in Fig. 1-8 (b) and (c), respectively. As can be observed in Fig. 1-8(b), the red and blue arrows indicate the Pb-O2 dipoles located in *ac* and *bc* planes, respectively. Since the space group of PbTiO3 is *P*4*mm*, where the symmetry operation "4" indicates that the 4-fold rotation axis is perpendicular to the *ab* plane, this leads to no component of the Pb-O2 dipole in the *ab* plane, i.e., the dipole of Pb-O2 only has a component along the *c* axis. Thus, the direction of Pb-O2 dipole is along *c*-axis. For the shorter Ti-O1 bond, the dipole momentum is stronger than that of the longer Ti-O1 bond; therefore, the total dipole momentum of Ti-O1 is oriented along the direction of the shorter Ti-O1 dipole momentum. Meanwhile, the dipoles of Ti-O2 are canceled because of the symmetric operation of $PbTiO_3$. Hence, as shown in Figure 1-8(c), the dipole of Ti-O bond can be reduced to the Ti-O1(the shorter one) dipole. Therefore, the dipole of $PbTiO_3$ is along the *c*-axis and generate the spontaneous polarization oriented along [001] direction.

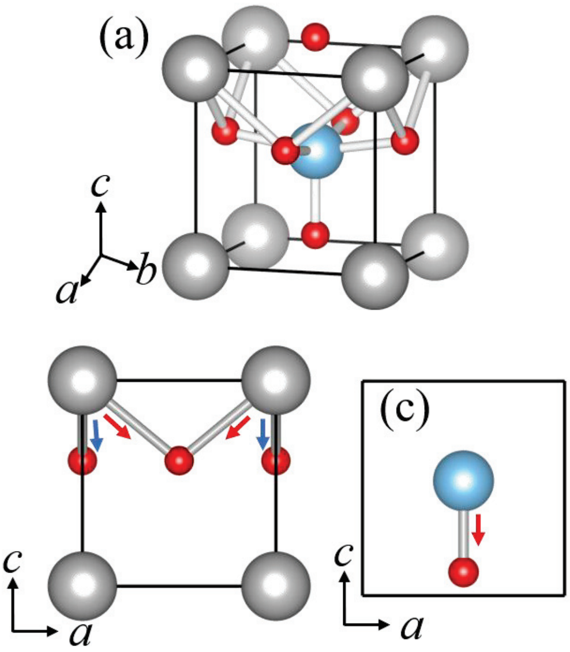

Fig. 1-8**.** Ball-and-stick model of tetragonal $PbTiO_3$. (a) three-dimensional model crystal structure of tetragonal $PbTiO_3$. Two-dimensional model crystal structure of (b) Pb-O2 and (c) Ti-O1. Blue and red arrows in (b) and (c) indicate the dipoles.

Since the early 1950s, the antiferroelectricity was noted, the lead zirconate $PbZrO_3$ with a perovskite-type structure attracts attention from many researchers.[88-94] Due to the perovskite structure, the prototype structure of $PbZrO_3$ is $Pm\bar{3}m$ at high temperature as the same as other perovskites, such as $PbTiO_3$ and $BaTiO_3$.[95] The details of the cube structure have been described in the previous section and do not need to be repeated here. From high temperature decreases to low temperature, the crystal structure transfer from cubic with space group of $Pm\bar{3}m$ to orthorhombic with space group of *Pbam* at about 505 K.[90] Meanwhile, this single-phase transition undergoes from paraelectric phase (cubic phase) to antiferroelectric phase (orthorhombic phase). The mechanism of this phase transition in $PbZrO_3$ perovskite is remained debatable. Z. G. Fthenakis et al. proposed that this phase transition is associated with two lattice modes, namely, Pb ions antipolar vibration and oxygen octahedron tilts dynamics.[91] However, A. K. Tagantsev et al. revealed that this phase transition is derived from the softening of a single lattice mode by flexoelectric coupling.[92]

The phase transition from paraelectric phase to antiferroelectric phase is coupled with antipolar of Pb ions and the tilt of the oxygen octahedron.[90] The former leads to the splitting of Pb into two types Pb ions at antiferroelectric phase, labelled Pb1 and Pb2. While later leads to the splitting of oxygen ions into five kinds of oxygen ions at antiferroelectric phase, labelled O1, O2, O3, O4, and O5, respectively. Due to the complicated crystal structure in orthorhombic phase, the lattice parameters $\boldsymbol{a}_\mathrm{O}$, $\boldsymbol{b}_\mathrm{O}$, and $\boldsymbol{c}_\mathrm{O}$ are rewrite as: $\boldsymbol{a_O} = \boldsymbol{a_C} + \boldsymbol{b_C}, \boldsymbol{b_O} = 2(\boldsymbol{a_C} - \boldsymbol{b_C})$, and $\boldsymbol{c_O} = \boldsymbol{2c_C}$ respectively, where $\boldsymbol{a}_\mathrm{C}$, $\boldsymbol{b}_\mathrm{C}$, and $\boldsymbol{c}_\mathrm{C}$ are the lattice parameters of cubic phase (here, $\boldsymbol{a}_\mathrm{C}$, $\boldsymbol{b}_\mathrm{C}$, and $\boldsymbol{c}_\mathrm{C}$ are the same value, about 4.13 Å). Hence, the values of lattice parameters a_O, b_O, and c_O are about $\sqrt{2}a_\mathrm{C}$, $2\sqrt{2}a_\mathrm{C}$, and $2a_\mathrm{C}$, respectively. The crystal structure of antiferroelectric phase $PbZrO_3$ is shown in Fig. 1-9. To elucidate the origin of antiferroelectricity of $PbZrO_3$ at orthorhombic phase, Fig. 1-9 (b) and (c) is extracted. As shown in Fig. 1-9 (b), the ball-and-stick model of Pb2-O3 was plotted in *ab* plane, where the red and blue arrows indicate dipole in different direction. Evidently, the two adjacent red arrows are in opposite directions, leading to zero total dipoles in red. The same phenomenon also occurs in the blue arrows, which means that the total dipoles in blue is zero. Meanwhile, as shown in Figure 1-9 (c), the Zr-O3 and Zr-O5 dipoles also exhibit the same characteristics of Pb2-O3 dipoles. Therefore, in the orthorhombic $PbZrO_3$ perovskite material, the adjacent dipoles are oriented in opposite directions, resulting in no spontaneous polarization and exhibiting antiferroelectricity.

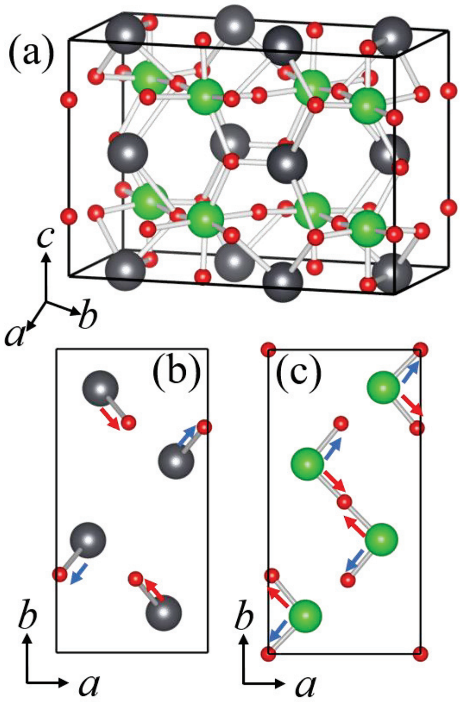

Fig. 1-9. Ball-and-stick model of orthorhombic $PbZrO_3$. (a) three-dimensional map crystal structure

of orthorhombic $PbZrO_3$. Two-dimensional map crystal structure of (b) Pb2-O3 dipoles and (c) Zr-O3 and Zr-O5 dipoles. Blue and red arrows in (b) and (c) indicate the dipoles.

The ferroelectric and antiferroelectric properties show distinctly different characteristics in ferroelectric hysteresis loop.[18,96] As shown in Fig. 1-10 (a), a linear correlation between the polarization *P* and external applied electric field *E* is observed in the low electric field. This reason is the low electric field can't switch the orientation of any ferroelectric domain, which is a uniformly polarized regions with the scales ranging from several nanometers to several ten microns. As the external applied electric field increases, the orientation of ferroelectric domains switch to the electric field direction and the polarization increases rapidly. When all domain finish switching, the polarization saturates and is named spontaneous polarization. While electric field decreases to zero, some domains are still along the electric field direction and the residual polarization is named as remnant polarization. However, in antiferroelectric materials, these domains have two processes of switching toward the electric field and two processes of rapidly increasing polarization because the adjacent domains are in opposite directions. In detail, at first, there is also a linear relationship between the polarization and electric field since the low electric field can't switch the direction of any domains. Then, as electric field increases, the domains at an acute angle to the direction of the applied electric field switch to the electric field direction and the polarization increases rapidly. Next, as electric field increases further, the domains at an obtuse angle to the direction of the applied electric field switch to the electric field direction and the polarization increases rapidly again. Therefore, for antiferroelectric material as shown in Fig. 1-10 (b), there are two rapidly increasing polarizations, i.e., the *P*-*E* hysteresis loop exhibits double hysteresis loop characteristics.

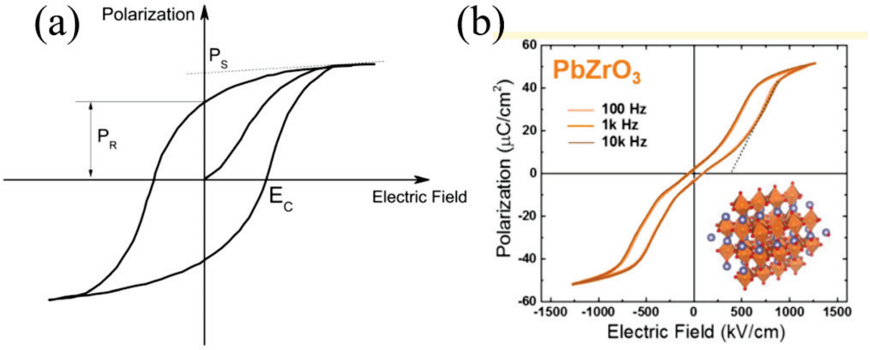

Fig. 1-10. Typical polarization hysteresis loop in (a) ferroelectric and (b) antiferroelectric materials.[18,96]

1.3.2 Synthesis of $Pb(Zr_{1-x}Ti_x)O_3$

Perovskite-type oxides have attracted the most interest among the studies of ferroelectric and piezoelectric materials. Remarkably, among these perovskite-type structure materials, lead zirconate titanate $Pb(Zr_{1-x}Ti_x)O_3$ is one of the most widely used piezoelectric materials because its unusual ferroelectric and piezoelectric properties depend on the stoichiometric component of the Ti ions contained in the *B*-site.[97-100] The phase diagram of $Pb(Zr_{1-x}Ti_x)O_3$ is displayed in Fig. 1-11, where the horizontal coordinate is the stoichiometric composition of the Ti ions.[99,101] As shown in Fig. 1-11(a), with increasing x content from 0 to 1 at room temperature, the members of perovskite lead zirconate titanate $Pb(Zr_{1-x}Ti_x)O_3$ family will undergo successive phase transition in orthorhombic, low temperature rhombohedral, high temperature rhombohedral, and tetragonal phase, corresponding to the space groups *Pbam*, *R*3*c*, *R*3*m*, and *P*4*mm*, respectively.[99,102,103] In particular, the presence of both rhombohedral (*R*3*m*) and tetragonal (*P*4*mm*) phases in $Pb(Zr_{1-x}Ti_x)O_3$ in the narrow range of x approximately equal to 0.475 shown in Fig. 1-11(b) is defined as the morphological phase boundary (MPB). Notably, in this region, $Pb(Zr_{1-x}Ti_x)O_3$ exhibits a very high piezoelectric response, since the polarization easily changes direction between [001] and [111]. Meanwhile, the phase transition temperature of $Pb(Zr_{1-x}Ti_x)O_3$ from ferroelectric to paraelectric phase is between that of $PbTiO_3$ and $PbZrO_3$ and shows a sensitive temperature-dependence of the Ti content change, which implies that the composition of $Pb(Zr_{1-x}Ti_x)O_3$ can be confirmed by the phase transition temperature read from the phase diagram. Because of these excellent piezoelectric, ferroelectric, and thermal stability properties, $Pb(Zr_{1-x}Ti_x)O_3$ ceramics, especially those with MPB compositions, are one of the most typical and widely used in industrial piezoelectric-ferroelectric material, such as transducer, actuator, electromechanical sensor.

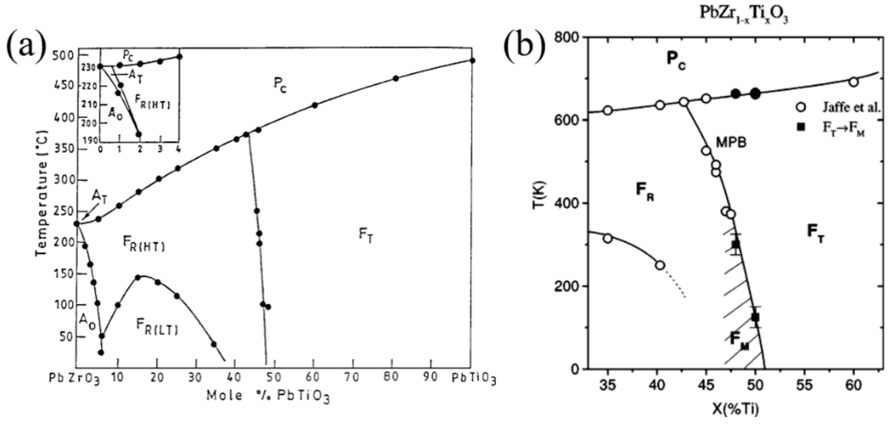

Fig. 1-11. Phase diagram of $Pb(Zr_{1-x}Ti_x)O_3$ system.[99,101]

Recently, B. Noheda et al.[101] and D. M. Hatch et al.[104] pointed out that the space group in $Pb(Zr_{0.52}Ti_{0.48})O_3$ perovskite in the region of MPB is *Cc* at low temperature by synchrotron x-ray powder diffraction and powder neutron diffraction, respectively. As shown in Fig. 1-11(b), they reveal the existence of a monoclinic phase with a space group of *Cc* between the previously established tetragonal phase and rhombohedral phase. In addition, the monoclinic phase can be commented as a bridge between the tetragonal and rhombohedral phases due to the displacement direction of monoclinic structure is along the [110] direction. The crystal structure of $Pb(Zr_{1-x}Ti_x)O_3$ solid-solution system perovskite can be seen anywhere in details. For tetragonal structure in the Ti-rich region, the crystal structure of $Pb(Zr_{1-x}Ti_x)O_3$ is similar to that of $PbTiO_3$, and the *B*-site is composed of Zr and Ti ions.

Since $Pb(Zr_{1-x}Ti_x)O_3$ has such a variety of excellent dielectric and thermal properties, the synthesis of $Pb(Zr_{1-x}Ti_x)O_3$ ferroelectric material in simplicity, controllability, fast-reacting, one-step operation and low-cost has been widely studied. Up to now, various methods such as sol-gel method, hydrothermal synthesis, high-energy ball milling method, self-propagation high-temperature synthesis, microwave processing, and other related means, have been proposed for synthesizing $Pb(Zr_{1-x}Ti_x)O_3$ ceramics and their films.[1,7-10,105-108] Although these methods are widely applied in synthesizing $Pb(Zr_{1-x}Ti_x)O_3$ material, there are still some demerits need to overcome. For instance, sol-gel reaction needs very expensive alkoxides as the raw materials, which is not stable in moisture atmosphere. Most of them require a calcination at high temperature.[6,8,105]

Recently, mechanochemical process has been successfully used to synthesize $Pb(Zr_{1-x}Ti_x)O_3$ ceramic powder. High pure PbO, ZrO_2, and TiO_2 powders as the raw materials were used to synthesize $Pb(Zr_{1-x}Ti_x)O_3$ ceramics by means of high-energy ball milling, which is the method of mechanochemical reaction.[6,109] However, this process also has some imperfection, the obtained $Pb(Zr_{0.52}Ti_{0.48})O_3$ phase has some PbO residuals after 80 hours of ball milling.[6,109] In addition, they also didn't provide evidence to explain why this component of $Pb(Zr_{1-x}Ti_x)O_3$ phase is $Pb(Zr_{0.52}Ti_{0.48})O_3$. Nevertheless, their work exhibits an interesting clue to further investigate an easily controlled and low-cost mechanochemical process means to synthesize $Pb(Zr_{1-x}Ti_x)O_3$ material. Our work further considers to synthesize $Pb(Zr_{1-x}Ti_x)O_3$ ceramic powder by dry ball milling a mixture of $PbTiO_3$ and $PbZrO_3$ powders as the starting powders.

1.3.3 Purposes

In this study, we synthesized $Pb(Zr_{1-x}Ti_x)O_3$ ceramic powders by mechanochemical solid-state reaction at room temperature using dry ball milling to grind the mixture of $PbTiO_3$ and $PbZrO_3$ powders with a molar ratio of 1 : 1. Synchrotron-radiation X-ray powder diffraction experiments were carried out to determine the structural characteristics and phase transition behavior of $Pb(Zr_{1-}$

${}_x$Ti$_x$)O$_3$ ceramic powders. Based on the diffraction patterns, crystal structure and phase transition behavior of Pb(Zr$_{1-x}$Ti$_x$)O$_3$, the validity of the synthesis of mechanochemical solid-state reaction is discussed. The composition of as-synthesized Pb(Zr$_{1-x}$Ti$_x$)O$_3$ has been investigated by the phase diagram and the crystal structure analysis using the Rietveld method.

Chapter 2

Experimental method

2.1 Sample synthesis

2.1.1 $PbTiO_3$ AD film

The starting powders of $PbTiO_3$ were synthesized by conventional solid-state reaction using 73.6473 g of PbO (purity 99.99%, Kojundo Chemical Lab. Co., Ltd.) and 26.3527 g of TiO_2 (purity 99.99%, Kojundo Chemical Lab. Co., Ltd.) at 850 °C for 4 h in air after 1 h of ball milling. The calcined starting powders of $PbTiO_3$ were selected a particle size about 1 μm for AD process. The AD film with 3−5 μm thickness was deposited on the glass substrate. The starting powder mixed with dried air (the carrier gas) in the aerosol chamber to form the aerosol flow, which was sprayed through a nozzle with rectangular shaped orifice of 10 mm × 400 μm size. The pressures in the deposition chamber was around 100 Pa during the deposited process.

2.1.2 $Bi_4Ti_3O_{12}$ AD film

The $Bi_4Ti_3O_{12}$ starting powders were synthesized by conventional solid-state reaction at 800 °C for 2 hours of ball milling using high quality Bi_2O_3 (purity: 99.9999 %, RARE METALLIC Co., Ltd.) and TiO_2 (purity: 99.99 %, Kojundo Chemical Lab. Co., Ltd.) as the raw materials. Then, to obtain the $Bi_4Ti_3O_{12}$ starting powders with non-plate-like shape, the starting powders were milled in ethanol for 1 hour with a planetary ball media and then dried at 80 °C in air. In the AD process, the particle size of the calcined $Bi_4Ti_3O_{12}$ starting powders are selected to be around 1 μm.

The $Bi_4Ti_3O_{12}$ AD film was deposited on a glass substrate. The thickness of as-deposited AD film is about 5 μm. In the AD process, a mixture of $Bi_4Ti_3O_{12}$ powders and dry air is accelerated by a pressure difference and ejected through a nozzle with an aperture of 10 mm × 400 μm to impact on the glass substrate. The pressure difference between the aerosol chamber and the deposition chamber was around 100 Pa.

2.1.3 $Pb(Zr_{1-x}Ti_x)O_3$ powder

Ceramic powders of PZ and PT with a particle diameter of approximately 1 μm were prepared using a conventional solid-state reaction with commercially available ZrO_2 (purity: 98%, Kojundo Chemical Lab. Co., Ltd), PbO (purity: 99.99%, Kojundo Chemical Lab. Co., Ltd), and TiO_2 (purity: 99.99%, Kojundo Chemical Lab. Co., Ltd.) powders. These originally synthesized PZ and PT powders were mixed well at a molar ratio of 1 : 1 as the starting powder with ethanol and dry ball-milled using a planetary ball mill system (P-6 classic line, Fritsch Japan Co., Ltd). Sample mixtures of 20 g were ball-milled in an Ar gas atmosphere for 4, 8, 16 and 32 h, where the milling was stopped every 30 min for cooling, and labeled as 4h PZ–PT, 8h PZ–PT, 16h PZ–PT, and 32h PZ–PT, respectively. A 500 mL zirconia bowl and SiC balls (mixture of 50 large balls with diameter of 10 mm, and small balls weighting 50 g with diameter of 5 and 2 mm, respectively) were used as the milling media. The milling speed was set at 450 rpm.

2.2 Synchrotron radiation X-ray diffraction

Synchrotron radiation is an advanced high-energy light source that can be widely used for structural characterization and phase identification of materials at the atomic level. The synchrotron radiation light is produced by the deflection of relativistic particles (electrons or positrons) in a magnetic field.[110-114] For a third-generation synchrotron radiation light source, such as SPring-8 in Japan,[110] the schematic diagram of synchrotron radiation generation by relativistic electrons under the applied bending magnet is shown in Fig. 2-1. The relativistic electrons were accelerated to near the speed of light and then emit the synchrotron radiation light under an applied bending magnetic field. Therefore, the synchrotron radiation light source has main features shown in follow: high intensity, ultra-bright, high pure, high degree of polarization, very broad and continuous spectral range, quasi-monochromatic, linearly or circularly polarized, pulsed with controlled intervals, and high degree of collimation. In detail, for the feature of high intensity, the intensity of the third-generation synchrotron radiation light is a hundred billion times higher than that of the laboratory X-ray light. In addition, in contrast to laser, synchrotron light is concentrated in a narrow direction and almost all of the light is in a parallel beam. There are many other advantages of third-generation synchrotron light, which you can read about in detail anywhere, and we will not cover them here.

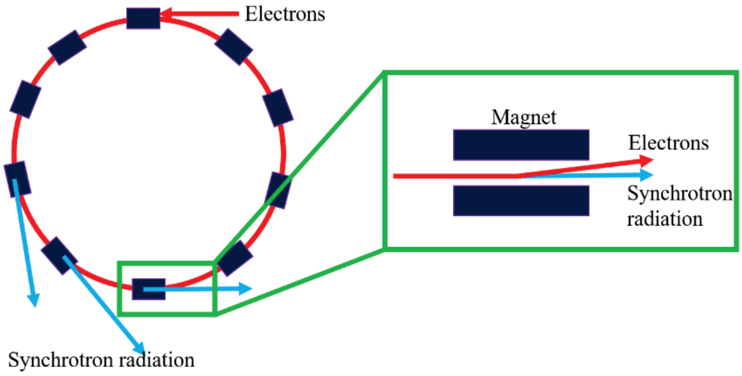

Fig. 2-1. Schematic imagine of a third-generation synchrotron radiation. Red line indicates the electrons accelerated to near the speed of light. Dark blue rectangle implies bending magnet. While the blue line means the synchrotron radiation light.

Synchrotron radiation light sources were widely used in physical, chemical, biology and other fields, such as archaeology. In this study, synchrotron radiation X-ray powder diffraction experiment was required to collect the precise crystal structure information and electron density distribution at SPring-8, Japan. SPring-8 is one of the largest and most advanced third-generation synchrotron radiation facility in the world, located in Harima Science Park City, Hyogo Prefecture, Japan.[110] As shown in Fig. 2-2, the SPring-8 facility consists of several systems, including electron gun, linear accelerator, storage ring, and beamlines for different scientific fields. First, the electron beam is generated by an electron gun and then accelerated by a linear accelerator to about 1 GeV. Further, the electron beam is accelerated to 8 GeV in the synchrotron to obtain high energy state electrons. Meanwhile, the electrons with energy of 8 GeV are introduced into the storage ring. Finally, the synchrotron radiation light generated by high energy electrons under an applied bending magnet, as detailed in Fig. 2-1, is introduced into different beamline stations for different scientific fields.

Fig. 2-2. Bird view of Spring-8 facility.

SPring-8 BL02B2 is a beamline station for polycrystalline powder X-ray diffraction using high energy synchrotron light in a wide range of 12 to 37 KeV. To achieve the energy continuous change, the optical system consisted of a curved mirror and a double Si crystal monochromator is installed in BL02B2. In this optical system shown in Fig. 2-3, in order to eliminate the high-order harmonics and collimate the X-rays, the mirrors are composed of silicon, nickel and platinum for different energies up to 15.5 keV, 15.5-28.2 keV and above 28.2 keV, respectively. To improve the parallelism of X-rays and the energy resolution, double Si crystal monochromator is also installed in this optical system. At the same time, the crystal plane (111) of Si crystal is used as a standard. Even the energy up to 37 keV, the energy resolution $\Delta E/E$ remains around 2×10^{-4}. According to Einstein equation, $\Delta E = h\nu$, where h is Planck constant. Thus, the relationship of wavelength and energy can be obtained as $\lambda = \frac{hc}{eV} = \frac{12.4}{E}$, where c is the speed of light, unit of E is keV, and unit of λ is Å. According to this relationship, the precise wavelength of synchrotron X-ray can be obtained by changing the energy state of synchrotron light.

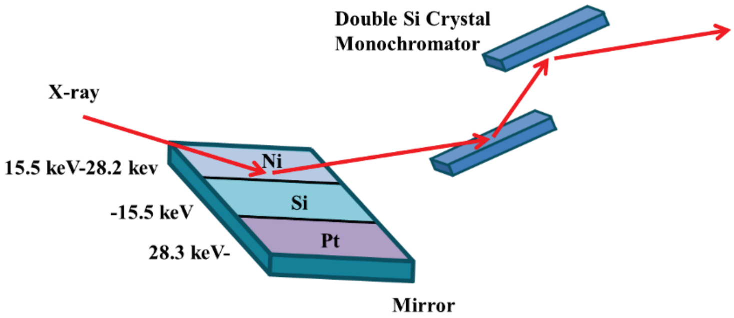

Fig. 2-3. Schematic view of the optical system in SPring-8 BL02B2.

In the beamline station of BL02B2, a large Debye-Scherrer camera with a two-circle diffractometer and imaging plate (IP) is installed. As shown in Fig. 2-4, two-dimensional (2D) IP detector and six one-dimensional (1D) MYTHEN detectors are developed in this measurement system to meet the needs of different applications. In 2D IP detector system, one hand, the preferred orientation, impurity, and crystallization of material can be clearly characterized. On the other hand, combined with the maximum-entropy-method and Rietveld method, the charge density distribution of measured material can be visualized. There are two kinds of modes can be used in the MYTHEN system, namely double-step and single-step modes. For the double-step mode, this system can accurately determine the crystal structure due to the large range of 2θ, which ensures that sufficient diffraction data can be collected. For the single-step mode, due to the range of 2θ is not enough, this system usually is used to collect the *in situ* diffraction data and identify the phase transition. More details about synchrotron radiation X-ray powder diffraction can be found in ref [110].

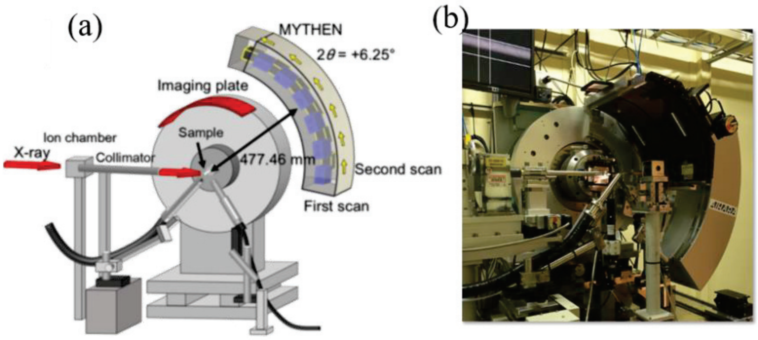

Fig. 2-4. (a) schematic imagine and (b) real photograph of the large Debye-Scherrer camera.[110]

In general, IP mode has higher efficiency for high-energy X-rays compared to MYTHEN mode. For MYTHEN mode, the quantum efficiency is less than 25 % when the energy of X-rays is larger than 30 keV. Thus, crystal structure studies requiring high energy X-rays, such as charge density analysis, preferentially apply the IP detector. On the other hand, the MYTHEN mode has better angular resolution than that of IP mode. Notably, these two measurement systems, IP detector and MYTHEN detector, can be used over a wide temperature range of 25K to 1473K.

2.3 Experimental conditions

2.3.1 AD films and starting powders of $PbTiO_3$ and $Bi_4Ti_3O_{12}$

AD films and starting powders of $PbTiO_3$

First, synchrotron radiation X-ray diffraction (SXRD) experiments were performed for $PbTiO_3$ starting powders, the self-supported films, and the AD films at the beamline BL02B2 at SPring-8. For $PbTiO_3$ starting powders, they were sealed into a quartz capillary with inner diameter of 0.1 mm. Then, the IP data (Debye-Scherrer patterns) were collected using X-rays with a wavelength of 0.780116(1) Å to evaluate the preferred orientation at room temperature for 5 mins. To further investigate this orientation behavior at high temperature condition, the temperature was elevated to 1000 K using high-temperature N_2 gas streams. To control the temperature deviation within 0.1 K at 1000 K, the data of Debye-Scherrer patterns were collected after waiting 5 mins when temperature was elevated to 1000 K. Also, after temperature cooling to room temperature again, waiting 5 mins to eliminate the temperature deviation and then collecting the IP data. These IP data also were collected 5 mins. The $PbTiO_3$ starting powders also were determined by the six 1D MYTHEN detectors to collect the diffraction data using the X-rays of 0.413850(1) Å (corresponding to the energy with 30 keV) to study the phase transition behavior and the crystal structure. Diffraction data were collected for 10 mins at room temperature, 1000 K, and room temperature after cooling, to analyze the crystal structures of tetragonal phase and cubic phase. Also, to control the temperature deviation within 0.1 K, these diffraction data at 1000 K and room temperature after cooling were collected after waiting 5 mins when temperature was heating to 1000 K and cooling to room temperature. To study the phase transition behavior, under high-temperature gas N_2 gas flows, the temperature of $PbTiO_3$ starting powders was elevated from room temperature to 1000 K with the heat rate of 20 K/min and then cooled to room temperature with the same cooling rate. The interval temperature ΔT of collecting diffraction data is 5 K during the heating and cooling process.

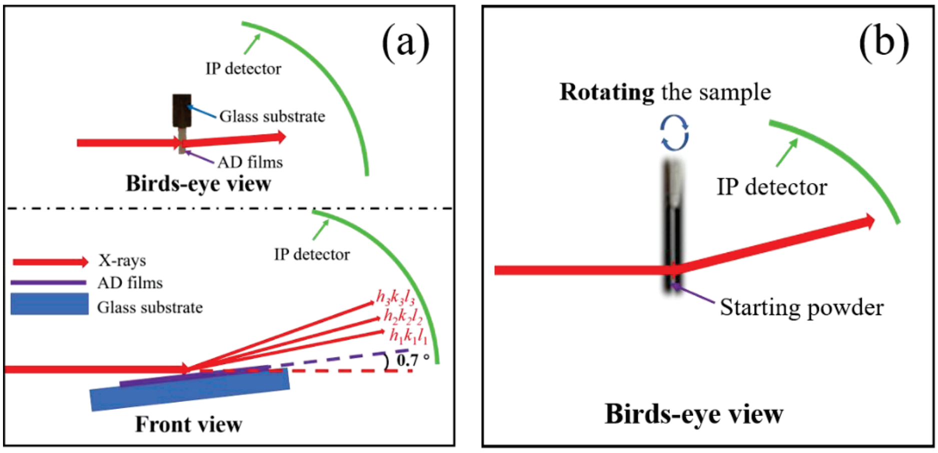

Fig. 2-5. Schematic image of measured conditions of $PbTiO_3$ (a) AD films and (b) starting powders and self-supported films.

Notably, as shown in Fig. 2-5 (a), to obtain a better quality of collecting data, $PbTiO_3$ AD films were set tilted 0.7° along the direction of parallel to the incident X-ray during collecting IP data. To investigate the behavior of preferred orientation, Debye-Scherrer patterns of $PbTiO_3$ AD films were recorded on IP detectors with the X-rays of 0.780116(1) Å at room temperature for 5 mins. Furtherly, to evaluate the temperature-dependent of preferred orientation, Debye-Scherrer patterns of $PbTiO_3$ AD films were recorded on flat IP detectors for 5mins at 500 K, 700 K, 750 K, 800 K, 850 K, 900 K, 950 K, and 1000 K, respectively. Then, during the cooling process, these Debye-Scherrer patterns also were recorded on flat IP detector for 5 mins at 950 K, 900 K, 850 K, 800 K, 750 K, 600 K, 500 K, and room temperature after cooling, respectively. Among this heating and cooling process, the phase transition behavior of $PbTiO_3$ AD films can be roughly determined. To confirm this phase transition behavior, the second heating process was performed and the IP data was collected for 5 mins at 500 K, 600 K, 700 K, 750 K, 800 K, 900 K, and 1000 K, respectively. Also, to keep the temperature deviation within 0.1 K, during the cooling and second heating process, these Debye-Scherrer patterns were also collected after waiting 5 mins when temperature was raised to the measured temperature.

To study the precise phase transition behavior and structural characteristics of $PbTiO_3$ AD films, we peel the AD films from the glass substrate and call the films without substrate as “self-supported films”. Then, the self-supported films cut into small pieces are sealed into a quartz capillary with 0.1 mm inner diameter. Using the X-rays of 0.413850(1) Å, the diffraction data of the $PbTiO_3$ self-supported films were collected for 10 mis at room temperature by the six 1D MYTHEN detectors to analyze the crystal structure. At high temperature 1000 K, the diffraction data of $PbTiO_3$ self-supported films were also collected for 10 mins. Then, to confirm the behavior of crystal structure, $PbTiO_3$ self-supported films were also measured for 10 mins at the room temperature after cooling, at 1000 K after second heating, and at room temperature after the second cooling, respectively. Under high-temperature N_2 gas flows, when increased or decreased temperature to the measured temperature, waiting 5 mins can ensure the temperature deviation within 0.1 K for these temperatures. Then, to further study the phase transition behavior of $PbTiO_3$ self-supported films, under high-temperature N_2 gas flows, temperature was increased from room temperature to 1000 K and then cool from 1000 K to room temperature with the heat or cool speed of 20 K/min. In particular, a second heating and cooling process was performed at the same heating and cooling rate of 20 K/min in order to accurately determine the phase transition behavior of the self-supported films. Here, the interval temperature ΔT of collecting diffraction data is also set to 5 K. In these experimental conditions, due to the heavy atom in the samples, Pb, the absorption effect of X-rays must should not be ignored. However, since the short wavelength of the X-ray and the small diameter of capillary, we can ignore this absorption effect.

AD films and starting powders of $Bi_4Ti_3O_{12}$

The measurement methods of AD films and starting powders of $Bi_4Ti_3O_{12}$ are roughly similar to those of $PbTiO_3$. Thus, the details of the experiments can be described here in a simplified manner. The starting powders of $Bi_4Ti_3O_{12}$ were sealed into the quartz capillary with an inner diameter of 0.1 mm. To explore the preferred orientation of $Bi_4Ti_3O_{12}$ starting powders, Debye-Scherrer patterns were recorded on IP detectors with the X-rays of 0.799203(1) Å at room temperature and 1100 K, respectively. Then, the diffraction data of $Bi_4Ti_3O_{12}$ starting powders were collected at room temperature, at 1100 K, and at room temperature after cooling, respectively, using MYTHEN detectors. These diffraction data are used to analyze the crystal structure. Phase transition behavior can be determined by heating from room temperature to 1100 K and then cooling to room temperature under the high-temperature N_2 gas flows. The heating and cooling rate is 20 K/min. The interval temperature ΔT for collecting diffraction data is also set to 5 K.

Next, to obtain a better quality of collecting data, $Bi_4Ti_3O_{12}$ AD films were set tilted 1° along the direction of parallel to the incident X-ray during collecting the SXRD data. Then, using the X-rays of 0.799203(1) Å, the IP data of $Bi_4Ti_3O_{12}$ AD films were recorded at room temperature, 1100 K, and room temperature after cooling, respectively. Next step is changing the wavelength of X-rays to 0.413034(1) Å to collect MYTHEN data. To analyze the crystal structure and phase transition behavior, $Bi_4Ti_3O_{12}$ self-supported films were cut into small pieces and then sealed into quartz capillary with an inner diameter of 0.1 mm. $Bi_4Ti_3O_{12}$ self-supported films were measured at room temperature, 1100 K, and room temperature after cooling, respectively. To confirm the precise phase transition behavior of $Bi_4Ti_3O_{12}$ self-supported films, under the high-temperature N_2 gas flows, the heating and cooling process were performed for two times from room temperature to 1100 K. The heating and cooling rate is 20 K/min. Also, the interval temperature ΔT for collecting diffraction data is 5 K. In these experimental conditions, the absorption effect can be ignored even with heavy atom Bi due to the short wavelength of X-rays and small diameter of capillary.

2.3.2 $Pb(Zr_{1-x}Ti_x)O_3$ powders

SXRD experiments were performed using a large Debye-Scherrer camera with a multi-MYTHEN-detector system installed at the powder diffraction beamline BL02B2 at SPring-8. The powder samples of PZ, PT, sintered bulk ceramic of PZT (PZT), and ball-milled PZ–PT samples (4h PZ–PT, 8h PZ–PT, 16h PZ–PT, and 32h PZ–PT) were sealed into quartz capillaries with an inner diameter of 0.1 mm. X-rays with a wavelength of 0.35 Å were used to analyze the crystal structure of the powder samples at RT and 1000 K in the ferroelectric and paraelectric phases, respectively. These experimental conditions enabled us to ignore the absorption and extinction effects while analyzing the SXRD data accurately using the Rietveld method. The sample temperatures were changed by a high-temperature N_2 gas flow system and controlled within 0.1 K. The phase transition in the PZT and 8h PZ–PT samples was evaluated by temperature sweep measurements at 20 K/min during heating and subsequent cooling of the samples in the temperature range between RT and 1000 K. For the 8h PZ–PT sample, the phase transition in the second heating/cooling cycle was measured to confirm the difference from that in the first heating/cooling cycle. The 2D intensity map as a function of the temperature was drawn based on the diffraction patterns collected every 5 K.

Chapter 3

Analysis method

The diffraction data obtained from SXRD experiments will be studied by follow analytical methods. First, Rietveld refinement analysis is one of most popular and accurate method for refining crystal structures.[115-117] Then, combined with maximum entropy method (MEM), the MEM/Rietveld method can be used to investigate the charge density distribution.[28,118] Specially, to analyze the structure of the powders after ball milling and thin films deposited by the AD method, Huang-diffuse scattering was introduced in this work. Finally, the analysis of Williamson-Hall method was used to determine the residual strain generated during the film deposited process and ball milling process.

3.1 Rietveld analysis

In 1967, Rietveld proposed an original method to analyze the neutron diffraction data.[119,120] To honor his contribution, this new method was named Rietveld refinement. Since then, Rietveld method has also been used to study X-ray diffraction data, which is a powerful tool for analyzing crystal structures. In Rietveld refinement method, based on a given structure model that is similar to the material of the unknown structure, the structure parameters can be carefully refined and obtain a good quality fitting result. Based on this method, many information can be obtained from the diffraction data, such as lattice parameters, atomic position, grain size, thermal vibration, and atomic occupancy, etc. For the material with a multi-phase structure, this method can also determine the ratio of each phase from the scattering factor.

In the Rietveld analysis, the fitting profile calculated from an approximate structure model should match the diffraction profile as closely as possible. Here, through the least-squares method, the error sum of the square is shown in follow:

$$S(x) = \sum_i w_i[y_i - f_i(x)]^2, \tag{3-1}$$

where y_i ($i = 1, 2, 3\ldots$) is the intensity of observed diffraction peak, w_i ($=1/y_i$) is the statistical weight, and $f_i(x)$ is the intensity of calculated diffraction peak. To estimate the fitting result of Rietveld analysis, there are some R factors as an index, such as R_{WP}, R_{I}, and R_{F}, which denote the weighted profile factor, the reliability factor for intensity comparison between observations and calculations, and the reliability factor for structural factor comparison between observations and calculations, respectively.[28] The details of these R factors show in follow:

$$R_{WP} = \left\{\frac{\sum_i w_i[y_i - f_i(x)]^2}{\sum_i w_i {y_i}^2}\right\}^{0.5}, \tag{3-2}$$

$$R_I = \frac{\sum_H |I'_{obs}(\boldsymbol{H}) - I_{cal}(\boldsymbol{H})|}{\sum_H I'_{obs}(H)}, \tag{3-3}$$

$$R_F = \frac{\sum_H \big||F'_{obs}(\boldsymbol{H})| - |F_{cal}(\boldsymbol{H})|\big|}{\sum_H |F'_{obs}(\boldsymbol{H})|}, \tag{3-4}$$

where $\boldsymbol{H}$ is the Miller index (h, k, l), $I'_{\mathrm{obs}}(\boldsymbol{H})$ and $I_{\mathrm{cal}}(\boldsymbol{H})$ is the intensity of observed and calculated, and $F'_{\mathrm{obs}}(\boldsymbol{H})$ and $F_{\mathrm{cal}}(\boldsymbol{H})$ is the structure factor of observed and calculated, respectively. In addition, the half width of peak profile, W, is also a necessary factor to evaluate the fitting result, which can be written as:

$$W^2 = u + v \times tan\theta + w \times tan^2\theta + p \times sec^2\theta \ , \tag{3-5}$$

where u, v, w, and p is the factor of peak function.

Crystal structure factor $F(\boldsymbol{H})$ can be written as:

$$F(\boldsymbol{H}) = \sum_j f_j T_j e^{2\pi i(hx_j + ky_j + lz_j)}, \tag{3-6}$$

where $T(h, k, l)$ is the temperature factor, f_{j} is atomic scattering factor, i is the imaginary number, and (x, y, z) is the atomic position. Here, the atomic scattering factor f_{j} can be written as follow:

$$f\left(\frac{sin\theta}{\lambda}\right) = \sum_{i=1}^{4} a_i \exp\left(-b_i \frac{sin^2\theta}{\lambda^2}\right) + c, \tag{3-7}$$

where a_{i}, b_{i}, and c are constant, which can be obtained from the International Tables for Crystallography C. Since f is equal to the atomic or ionic electrons number of atom when θ is 0, the value of f are different for different ionic or atomic states at low angle range. For instance, the atomic scattering factor of the $PbTiO_3$ material shown in Fig. 3-1 is different from that of ionic state at low angle about $\sin\theta / \lambda < 0.1$. Thus, due to the ionicity, this difference in atomic scattering factor at low angle can lead to a deviation of crystal structure factor at a fixed the temperature factor or a deviation in the temperature factor at a fixed the crystal structure factor. Therefore, to obtain a precise charge density distribution, it is also necessary to collect the high-angle diffraction data for analysis and then obtain the temperature factor. Then, fixing the temperature factor, the crystal structure factor can be obtained from the diffraction data for the whole range of 2θ, including also the low angle range.

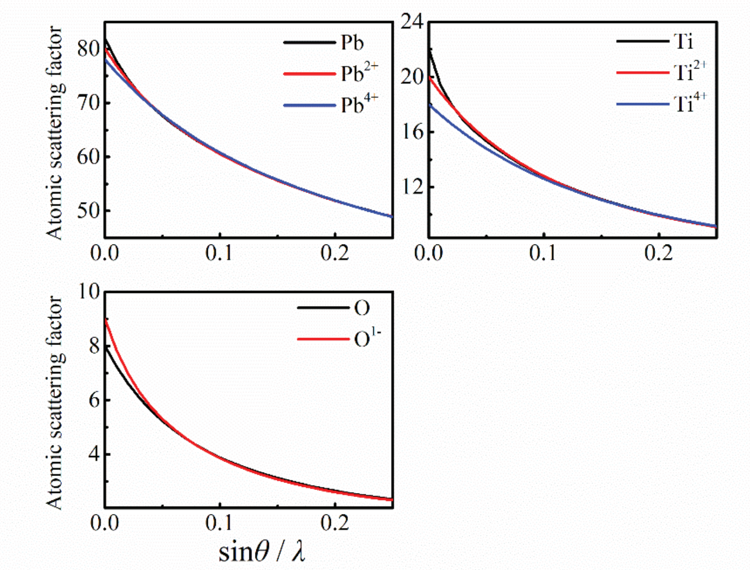

Fig. 3-1. Atomic scattering factor *f* as a function of sinθ / λ. In the high angle range, the atomic scattering factor of atom state is equal to that of ionic state.

3.2 Maximum entropy method (MEM) / Rietveld method

3.2.1 Maximum entropy method (MEM)

In 1948, Shannon et al. created information theory, which uses entropy to measure the uncertainty of information sources.[121,122] Because this entropy has a mathematical behavior similar to thermodynamics and statistical mechanics, this entropy is named information entropy or Shannon entropy. Since then, a new method for studying crystal structures based on information entropy, namely MEM, has been proposed. In the early 1980s, MEM was introduced to analyze the crystal structure of single crystals by X-ray diffraction.[123] Specially, the theory, algorithms, computer programs and experimental applications of the MEM for crystal structure determination were systematically studied, and the MEM was extended to crystal structure analysis by powder diffraction in the early 1990s. Up to now, MEM has been widely used not only for crystal structure but also for spectral analysis.[124-126]

In crystal structure analysis, the continuous electron density distribution function $\rho(\boldsymbol{r})$ can be used to substitute the isolate atom, where $\boldsymbol{r}$ is (x, y, z). Then, the structure factor $\mathrm{F}(\boldsymbol{H})$ can be written as follow:

$$F(\boldsymbol{H}) = V\int \rho(\boldsymbol{r})e^{-2\pi i(hx+ky+lz)}dxdydz. \tag{3-8}$$

Next, the entropy can be defined and shown in follow:

$$S = -\sum_{r}\rho'(\boldsymbol{r})ln\frac{\rho'(r)}{\rho'_0(r)}, \tag{3-9}$$

$$\rho'(\boldsymbol{r}) = \rho(\boldsymbol{r}) / \int \rho(\boldsymbol{r})\, d\boldsymbol{r}, \tag{3-10}$$

$$\rho_0'(\boldsymbol{r}) = \rho_0(\boldsymbol{r}) / \int \rho_0(\boldsymbol{r})\, d\boldsymbol{r}, \tag{3-11}$$

where $\rho_0(\mathbf{r})$ is the electron density in a reference state. Here, the binding function C was introduced,

$$C = \frac{1}{N} \sum \frac{|F_{cal}(\boldsymbol{H}) - F_{obs}(\boldsymbol{H})|^2}{\sigma_{\boldsymbol{H}}^2}, \tag{3-12}$$

where $F_{cal}(\boldsymbol{H})$ and $F_{obs}(\boldsymbol{H})$ is the structure factor of calculated and observed, respectively, and $\sigma_{\boldsymbol{H}}$ is the deviation of $F_{obs}(\boldsymbol{H})$. C is expected to be 1 from the error theory. Thus, the entropy $Q(\lambda)$ that has been bound can be rewritten as follow:

$$Q(\lambda) = -\sum_{\boldsymbol{r}} \rho'(\boldsymbol{r}) ln \frac{\rho'(\boldsymbol{r})}{\rho_0'(\boldsymbol{r})} - \frac{\lambda}{2}(C-1), \tag{3-13}$$

where λ is the Lagrangian multiplier. The maximum value of $Q(\lambda)$ can be obtained when the first-order partial derivative $\partial Q(\lambda)/\partial \rho(\boldsymbol{r}) = 0$. Thus, in this condition,

$$\rho(r) = \exp\,[ln\rho_0(\boldsymbol{r}) + \lambda F_0 \sum \frac{F_{cal}(\boldsymbol{H}) - F_{obs}(\boldsymbol{H})}{\sigma_{\boldsymbol{H}}^2} \exp\,(-2\pi i\boldsymbol{H})], \tag{3-14}$$

where F_{cal} $(\boldsymbol{H})$ come from the Fourier transform of $\rho_0(\boldsymbol{r})$. The details of F_{cal} $(\boldsymbol{H})$ can be written as follow:

$$F_{cal}(\boldsymbol{H}) = V \int \rho_0(\boldsymbol{r}) \exp(-2\pi i\boldsymbol{H})\, d\boldsymbol{r}. \tag{3-15}$$

In the actual calculation, firstly, $\rho_0(\boldsymbol{r})$ is given a uniform electron density and then calculate the $\rho(\boldsymbol{r})$. This process will be iterated until C is not greater than 1, and finally the electron density distribution $\rho(\boldsymbol{r})$ is obtained. Since the operation of iteration, the influence of initial value $\rho_0(\boldsymbol{r})$ can be ignored.

3.2.2 Weighting of MEM

MEM is a powerful tool to study the electron density distribution and nature of chemical bond. The standardized residual $\triangle F$ is defined as follow:

$$\Delta F = \frac{|F_{obs}| - |F_{MEM}|}{\sigma_{obs}}, \tag{3-16}$$

where F_{obs} and F_{MEM} is the measured structural factor and structural factor estimated by MEM. To obtain ideal MEM analysis results, the distribution of $\triangle F$ should match the Gaussian distribution. Thus, R. Y. De Vries et al. proposed $|\boldsymbol{H}|^{-n}$ to estimate the result of MEM analysis, where $\boldsymbol{H}$ and n is the reciprocal lattice vector and related weight, respectively.[127] By reasonably changing the value of n, high quality electron density distribution maps can be obtained.

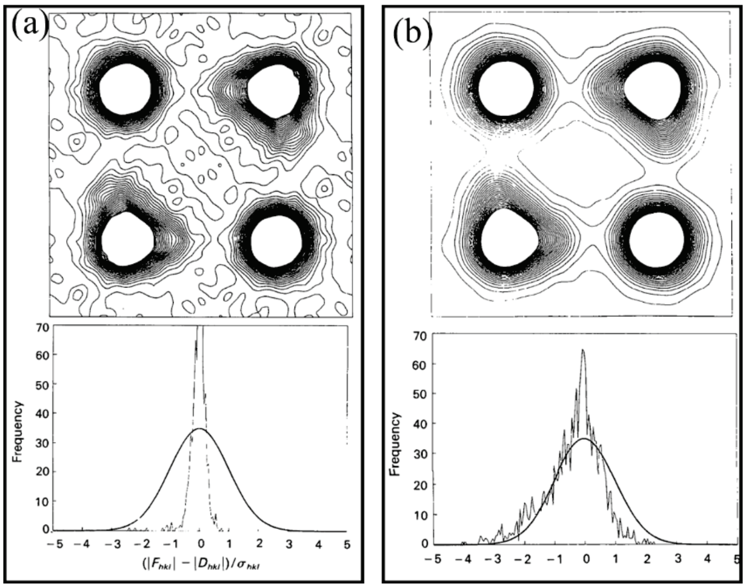

Fig. 3-2. Electron density distribution came from MEM (a) without change weight and (b) change weight.[127]

The improvement in the quality of the electron density distribution can be clearly observed in Fig. 3-2. Thus, a smooth surface of electron density distribution can be obtained by adopting the value of weight.

3.2.3 MEM / Rietveld method

The electron density distribution can be visualized by combining MEM and Rietveld refinement analysis, and this combined method is named MEM/Rietveld method.[124] From synchrotron radiation X-ray diffraction data to visualized electron density distribution, the complicated process can be described as four steps. Diffraction data was extracted from 2D IP data along 2θ direction. Thus, for the 1D diffraction data, there are many Bragg peaks overlapping each other. To obtain the accurate electron density distribution from the 1D diffraction pattern,

(1) separating the multiple overlap peaks and multiplying each the product of the peak,
(2) obtaining the crystal structure factor by applying various corrections,
(3) assuming a crystal structure model and based on this to obtain the structure factors,
(4) carrying out the MEM analysis based on the obtained structure factors.

The steps of (1)-(3) are analyzed by Rietveld refinement method. Then, based on the crystal structural factor, the electron density distribution can be analyzed by MEM. Finally, when the obtained electron density distribution is consistent with the crystal structure model, the obtained electron density is the final electron density. Otherwise, the Rietveld model should be corrected according to the electron density and then the steps of (1)-(4) should be performed again. The flow chart of the MEM/Rietveld method is displayed in Fig. 3-3.

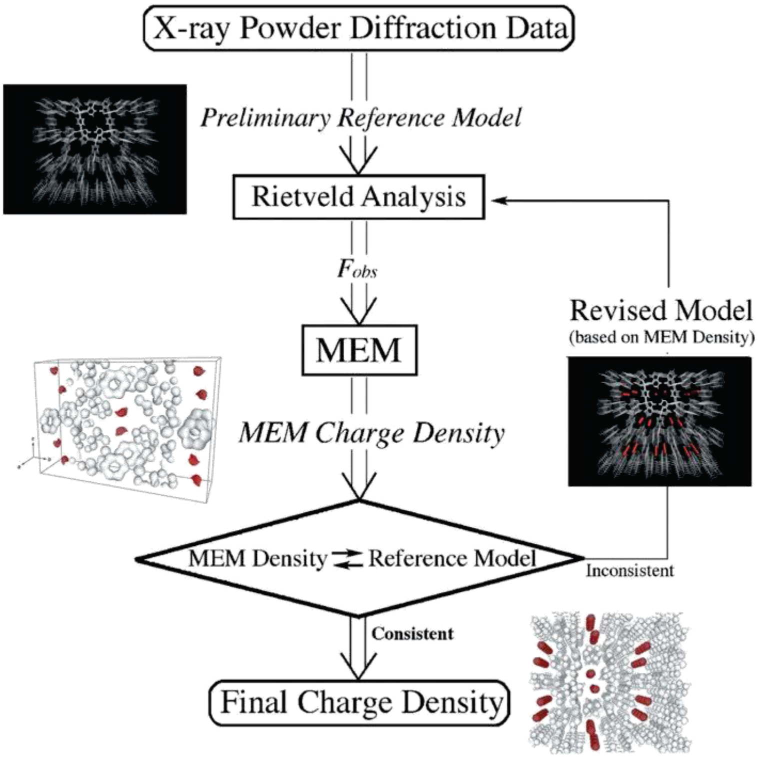

Fig. 3-3. Flow chart of the MEM/Rietveld method.[124]

3.3 Huang diffuse scattering

Due to various physical mechanisms, diffuse scattering of X-rays in solids can be classified into four types: 1, thermal diffuse scattering derived from lattice atomic vibrations; 2, Compton diffuse scattering due to electron absorption in atoms; 3, superlattice diffuse scattering caused by the degree of structure order; and 4, Huang diffuse scattering caused by lattice atomic shifts or charge shifts caused by various types of lattice defects.

The effect of defects on X-ray reflection was first reported theoretically by Kun Huang in 1947.[128] Huang pointed out that small deviations from the ideal lattice sites will lead to the diffuse scattering near the Bragg peak. Meanwhile, Huang predicted that the diffuse intensity is inversely proportional to the square of the distance in reciprocal space. This diffuse scattering derived from the lattice defects is different from the thermal diffuse scattering and is named as Huang diffuse scattering. Because the intensity of Huang diffuse scattering is small and this effect is mixed with thermal diffusion, it is not easy to distinguish Huang diffuse scattering from the thermal diffuse scattering at ordinary temperatures. It was not until 1967 that Peisl et al. experimentally discovered this effect from LiF crystals.[129]

Therefore, experiments with X-rays can obtain the information on displacements caused by defects or small defect agglomerates from Huang diffuse scattering.

3.4 Williamson-Hall method

It is well known that a small grain size can lead to a broadening of the X-ray peak profile shape. Therefore, the grain size can be inferred from the X-ray peak width. Generally, X-ray diffraction can accurately determine the average grain size of nanometer to micrometer sized crystals. In 1918, Scherrer first proposed the well-known formula, the Scherrer equation, as shown in follow:

$$D = \frac{K\lambda}{\beta cos\theta}, \tag{3-17}$$

where D is the average crystal size, K is the constant related to the crystallite shape, generally set to about 0.9, λ is the wavelength in Å, β is the full width at half maximum of Bragg peak, and the unit of θ is radian.[130]

In addition to the contribution of grain size, the intrinsic strain also induces a broadening of the Bragg diffraction peak profile. Thus, in addition to the instrumental effect, the physical mechanism of peak broadening includes a two-part contribution: grain size and strain. The strain due to crystal imperfections, such as point defects, grain boundary junctions, residual stresses can be calculated according to the modified Bragg equation.[130,131]

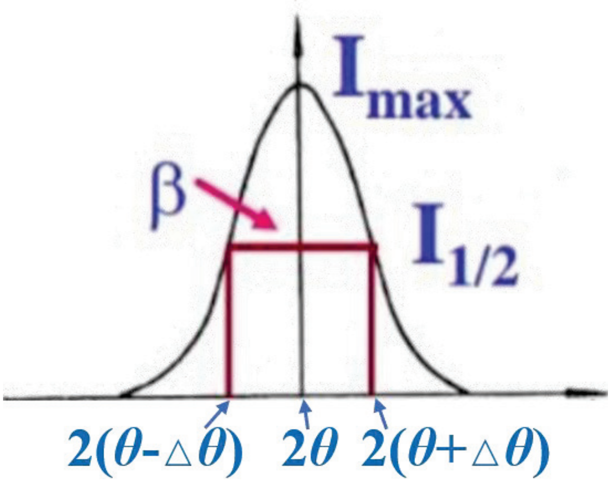

Figure 3-4. Schematic image of the deviation of 2θ derived from strain.

Assuming that the deviation of the peak position 2θ derived from the strain is $\triangle\theta$, the Bragg equation can be rewritten as:

$$2(d + \Delta d)\sin(\theta + \triangle\theta) = \lambda. \tag{3-18}$$

Ignoring the high-order items, the mean strain can be obtained:

$$\varepsilon = \frac{\Delta d}{d} = -\triangle\theta \cdot cot\theta. \tag{3-19}$$

Due to the full width at half maximum β is four times higher than that of $\triangle\theta$, the relationship between strain and strain-induced peak width can be expressed as:

$$\beta_{strain} = 4\varepsilon \cdot tan\theta. \tag{3-20}$$

Therefore, according to the equations of (3-17) and (3-20), the total peak width derived from the grain size and strain can be written as follow:

$$\beta_{total} = \beta_{size} + \beta_{strain} = \frac{k\lambda}{D\cdot cos\theta} + 4\varepsilon \cdot tan\theta. \tag{3-21}$$

The Williamson-Hall equation (W-H equation) can be obtained by rewriting the equation of (3-21) as shown below:

$$\beta_{(hkl)}cos\theta = \frac{K\lambda}{D} + 4\varepsilon \cdot sin\theta\ . \tag{3-22}$$

Thus, based on the W-H equation, a graph with 4sinθ along the *x*-axis and $\beta_{(hkl)}$cosθ along the y-axis can be drawn to analyze the grain size and strain. For instance, as reported by D. Nath et al, the particles size and strain analysis of CdSe nanoparticles are plotted in Fig. 3-5.[130]

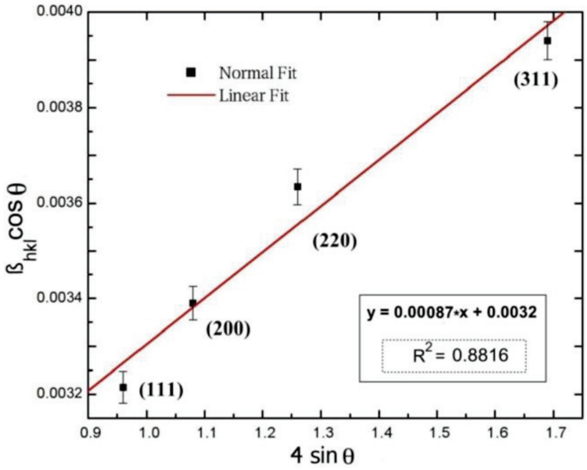

Fig. 3-5. W-H plot for CdSe nanoparticle.[130]

Chapter 4

Mechanism of film growth in $PbTiO_3$ and $Bi_4Ti_3O_{12}$ AD films

4.1 Mechanism of film growth in AD films

$PbTiO_3$ (PT) ferroelectric thin films have been widely investigated by various methods such as metalorganic chemical vapor deposition, sol-gel method, RF magnetron sputtering, pulsed laser deposition, hydrothermal method, and related means.[68,69,82,132-134] However, the mechanism of PT film growth remains obscure. Recently, J. Akedo et al. proposed a new method (AD method) deposited at room temperature that can avoid negative thermal expansion during the phase transition from cubic to tetragonal phase with cooling temperature.[73] Interestingly, PT thin films deposited by most methods, including the AD method, exhibit a *c*-axis preferred orientation.[46,67,82,83,133,135,136] Therefore, there is an intrinsic correlation between preferred orientation of PT thin films and film growth. In this work, we use PT AD films as a model to comprehensively study the mechanism of the film growth in PT ferroelectric thin films.

4.1.1 Preferred orientation in AD films

Debye-Scherrer patterns of the PT starting powders and the as-deposited AD films recorded on IP detector at room temperature (RT) are shown in Fig. 4-1. As shown in Fig. 4-1(a), the PT starting powders measured by rotating the capillary exhibit a homogenous diffraction intensity distribution, indicating that there is no preferred orientation in the PT starting powders. Meanwhile, the as-deposited AD film in Fig. 4-1(b) was tilted by 0.7° along the incident X-ray direction for collecting high-quality diffraction data, showing polycrystalline properties. Evidently, the intensity distribution of (00*l*), such as (001) and (002) marked in Fig. 4-1(b) by red, is not homogenous, revealing the preferred orientation along the *c*-axis in the AD film. Since the angle between the incident X-rays and the AD film is small, the (00*l*) in the Debye-Scherrer ring denotes the approximate normal direction to the film surface. Figure 4-1 (c) shows the diffraction profiles of the starting powders and the AD film along the direction of 2θ, colored by black and red, respectively. Since the intensity of the starting powders is too strong than that of the AD film, we divided the intensity of powder by 15 to obtain a good visual contrast in the same image shown in Fig. 4-1(c). Because lattice parameters *a* and *b* are the same at tetragonal phase, the ratio of the intensity of (*h*00) and (00*h*) should be 2:1 for randomly orientation PT material, such as the starting powders. However, the intensity of (00l) and (002) are stronger than that of (100) and (200) in the AD film, which means the *c*-axis preferred orientation. Meanwhile, the intensity of (111) peak is stronger than that of (001) and (002) in the starting powder, while the relationship is opposite in the AD film, that is the intensity of (001) and (002) are stronger than that of (111) peak. This also indicates the AD film exhibits *c*-axis orientation.

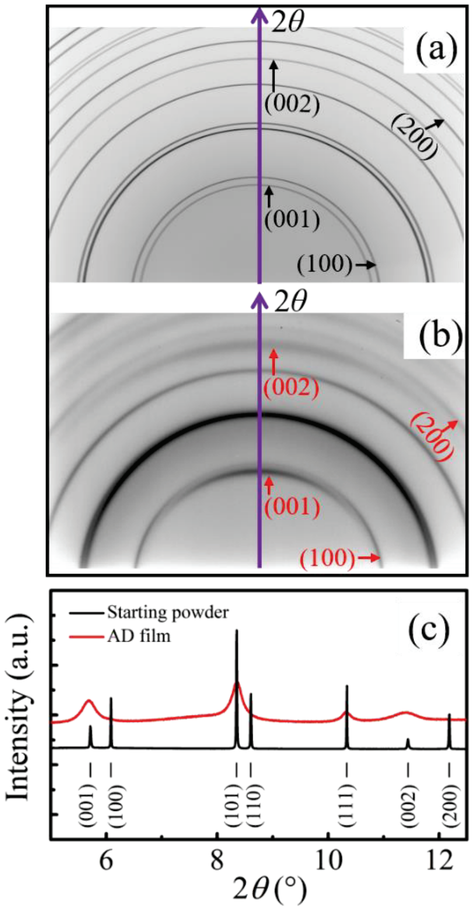

Fig. 4-1. Debye-Scherrer patterns of (a) PT starting powders and (b) PT as-deposited film at RT. (c) diffraction line profiles indicated by arrows in (a) and (b). AD film and starting powders indicated by the red and black lines, respectively.

To estimate the degree of the preferred orientation in the AD film, there are two evaluation methods, namely factor f and factor A.[70] On the one hand, the factor f is defined as $f = \frac{3}{2}\left(\frac{I_{(001)}}{I_{(001)}+I_{(100)}} - \frac{1}{3}\right) \times 100\%$, where the $I_{(001)}$ and $I_{(100)}$ are the intensities of (001) and (100) diffraction peaks calculated from the Lorentz function. For the ideal random direction, the value of f is 0, while for the ideal *c*-axis direction, the value of f is 100%. The fitting results are detailed in Table 4-1. The ratio of (001) : {(100) + (010)} diffraction peak intensity of PT starting powders is 36% : 64%, while the ratio of PT AD films is 99% : 1%. For the AD film at RT as shown in Fig. 4-

2, the value of *f* is 98.5%, indicating that it is close to the ideal (001) preferred orientation. On the other hand, the factor *A* describes the diffraction intensity distribution of the (001) Debye-Scherrer ring in 2D and is written as $A = (180 - w)/180$, where *w* is the full width at half maximum (FWHM) of the (001) diffraction peak. Use the program IPAnalyzer to obtain the (001) profile shown in Fig. 4-3(b) from the (001) Debye-Scherrer ring shown in Fig. 4-3(a). The value of *w* of the (001) peak calculated from the Pseudo-Voigt function is 55.6°, corresponding to the degree of 69 % for the preferred orientation *A*.

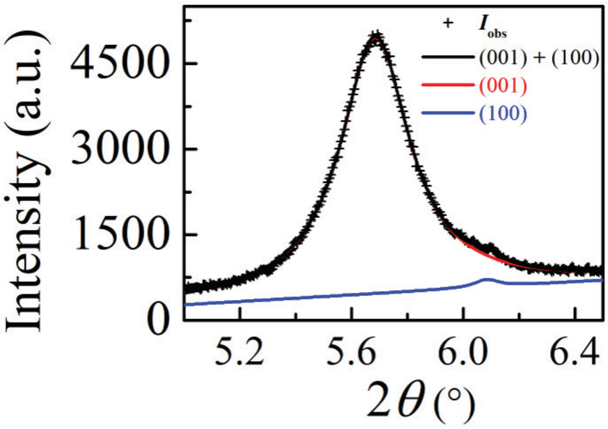

Fig. 4-2. Intensity distribution of (001) and (100) diffraction peaks of PT as-deposited film at RT. Black cross-shape denotes the observed intensity (I_{obs}). Black, red and blue solid lines indicate the fitting results of the combined diffraction peak of the (001) and (100), the (001) diffraction peak, and the (100) diffraction peak using Lorentz function, respectively.

Table 4-1. Ratio of (00*h*) and (*h*00) diffraction peak of PT starting powder and PT as-deposited AD film at RT. Ideal random orientation scenario for tetragonal phase also lists in this table to be compared.

Ratio of intensity	(001)	(100) + (010)	*f*
Random orientation	33%	67%	0
Starting powder	36%	64%	4.3%
AD film	99%	1%	98.5%

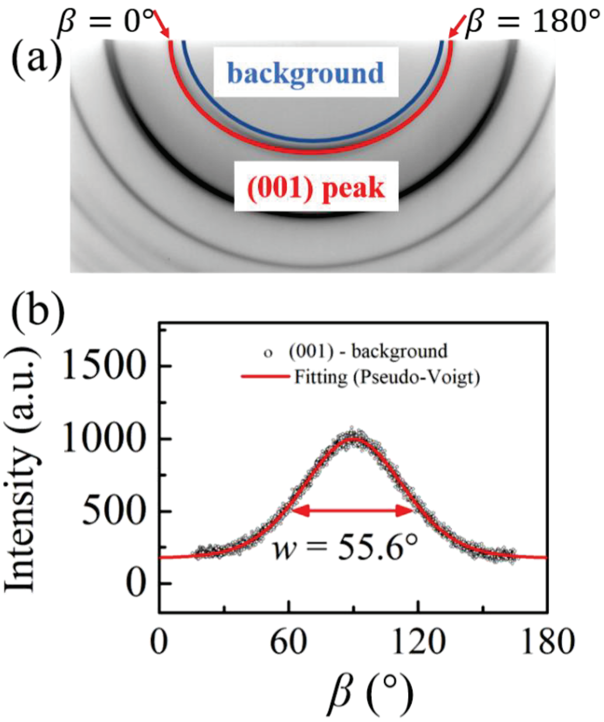

Fig. 4-3. Intensity distribution of the (001) Debye-Scherrer ring of PT as-deposited AD film at RT. (a) Debye-Scherrer patterns of PT AD film. (b) fitting result of the (001) Debye-Scherrer ring diffraction intensity distribution using Pseudo-Voigt function. Red and blue lines shown in Figure 4-3(a) is the (001) Debye-Scherrer ring and the related background, respectively.

4.1.2 Origin of film growth

To investigate the mechanism of *c*-axis orientation in the AD film, we further consider the preferred orientation of the starting powder and the AD film at 1000 K and RT after heating. Enlarged images of Debye-Scherrer rings of the PT starting powders and AD film are displayed in Fig. 4-4. As shown in Fig. 4-4 (a) and (b), it can be clearly seen that the Debye-Scherrer rings of the starting powders are uniform not only at RT but also at 1000 K, demonstrating that the starting powders are randomly oriented. Fig. 4-4 (c), (d), (e), (f), and (g) show the Debye-Scherrer rings of the AD film at as-deposited RT (RT0), 1000 K in the first heating/cooling cycle (1000 K1), RT after the first heating/cooling cycle (RT1), 1000 K in the second heating/cooling cycle (1000 K2), and RT after the second heating/cooling cycle (RT2), respectively. Intensity distribution of the AD film does not always remain inhomogeneous at these several temperatures. As mentioned above, it's inhomogeneous for the (00*h*) peak intensity distribution at RT0 for the AD film. However, the Debye-Scherrer rings of the AD film are uniform at 1000 K1, RT1, 1000 K2, and RT2, respectively. This result suggests that the *c*-axis oriented of the AD film appear only at RT0 but disappeared at

1000 K1, RT1, 1000 K2, and RT2.

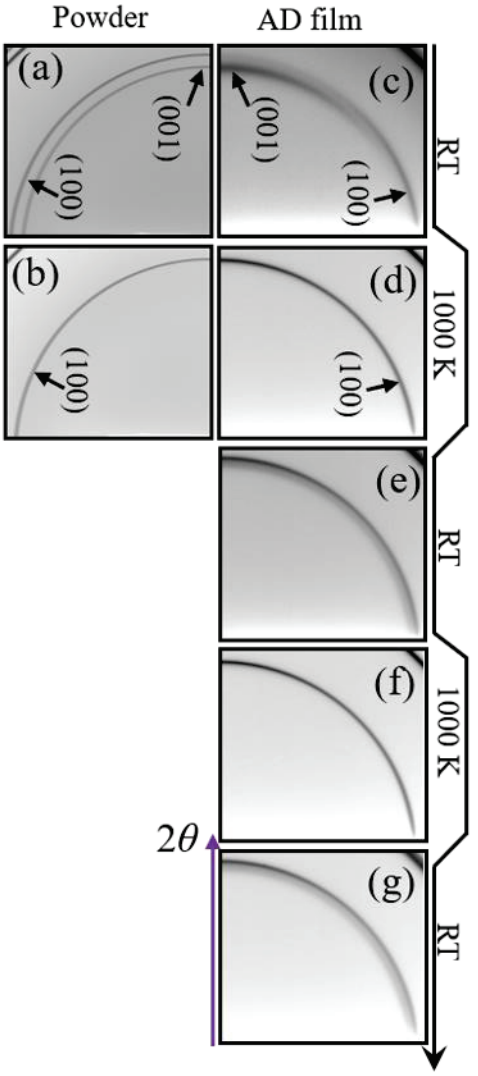

Fig. 4-4. Enlarged images of Debye-Scherrer rings of PT starting powders at (a) RT and (b) 1000 K; and of PT AD film at (c) RT, (d) 1000 K, (e) RT after 1st heating/cooling cycle, (f)1000 K in the 2nd cycle, and (g) RT after 2nd heating/cooling cycle.

Next task is to illustrate the mechanism by which the preferred orientation of the AD film appears at RT0 but vanishes at 1000 K1, RT1, 1000 K2, and RT2. Since PT is a tetragonal phase showing ferroelectric property at RT and a cubic phase showing paraelectric property at 1000 K, it is important to analyze the nature of the chemical bond of the tetragonal and cubic phases. As shown in the previous work of our group,[28] PT forms a 2D layered structure composed of covalent bonds at 300 K (the tetragonal phase), i.e., it is consists of the Ti-O_5 pyramid strongly bonded to Pb-O covalent bond; however, at 800 K (cubic phase), the layered structure of covalent bonding is destroyed because the six Ti-O bonds are the same and the Pb-O bond become ionic bond. Based on this work, we can acquire a clue that the 2D covalent bond structure plays an important role in understanding the preferred orientation behavior of AD film at RT0, 1000 K1, RT1, 1000 K2, and RT2. Figure 4-5(a) and (b) show Rietveld fitting results of the PT starting powders at RT and 1000 K, respectively. Then, as shown in Fig. 4-6, the charge density distribution of the PT starting powders at RT and 1000 K was obtained using MEM/Rietveld method. In the tetragonal phase (RT), the 2D layered structure consists of Pb-O2 covalent bond and Ti-O$_5$ pyramid and is parallel to the *ab* plane, as shown in Fig. 4-6 (a). While in the cubic phase (1000 K), as shown in Fig. 4-6 (b), the layered structure vanishes due to the covalent Pb-O bond becoming ionic and the Ti-O5 pyramid becoming Ti-O6 octahedron. Thus, we consider that the preferred orientation of the AD film is attributed to the layered characteristics. At RT, the layered covalent bond structure parallel to *ab* plane promotes the probability of particle recombination at a certain layer (the *ab* layer). While the weak bonds between PbTiO$_3$ layers along the *c*-axis direction can easily give rise to layer-to-layer cleavage or deformation. Thus, in this condition, the PT film deposited by the AD process exhibits a *c*-axis oriented. Since the layered covalent bond structure is vanished in the cubic phase, the *c*-axis oriented of the AD film will disappear when the temperature is higher than the Curie temperature. Since the layered structure has disappeared, the preferred orientation does not reappear during the cooling process.

There are other explanations for the preferred orientation of PT as-deposited AD film. For instance, to investigate the origin of the preferred orientation of Bi$_4$Ti$_3$O$_{12}$ (BiT) film, Suzuki et al. considered that the plate-like shape of the starting powders affects the deposited process.[70] Thus, in order to avoid the influence of plate-like shape, a non-plate-like shaped PT starting powders were selected out as shown in Fig. 4-7 (a). In this study, although the starting powders are in a non-plate-like shape, the as-deposited AD films also exhibit the preferred orientation. On the other hand, as shown in Fig. 4-7 (b), the crystal structure of PT starting powders is also a layered structure stacked along the direction of *c*-axis. Therefore, we consider that the PT ferroelectric films exhibit preferred orientation due to the characteristic of the layered crystal structure.

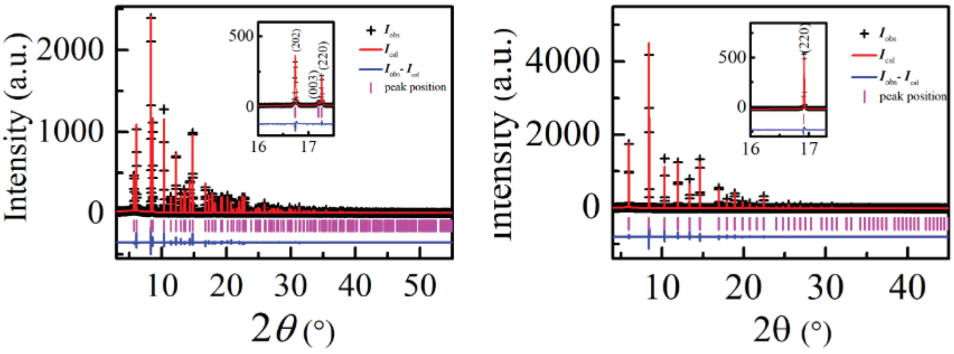

Fig. 4-5. Rietveld refinement of profile fitting results of PT starting powders at (a) RT and (b) 1000

K. Black cross-shape and red solid line indicate the observed and calculated diffraction intensity, respectively. Blue solid line denotes the difference between the observed and the calculated intensity. Magenta solid line is the Bragg peak position.

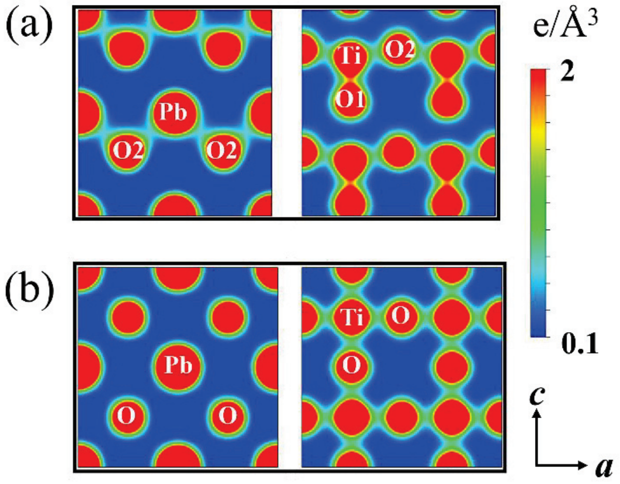

Fig. 4-6. 2D charge density distribution of PT starting powders at (a) RT and (b) 1000 K. Left and right columns show the Pb-O plane and Ti-O plane, respectively. The contour lines are drawn from 0 e Å^{-3} to 2 Å^{-3} with 0.2 e Å^{-3} intervals.

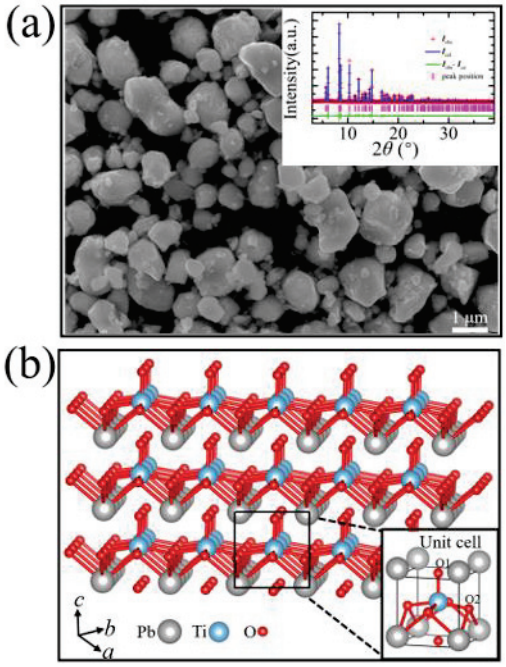

Figure 4-7. (a)SEM image and (b) crystal structure of PT starting powders at RT.

The preferred orientation in the PT AD film during heating and cooling may also have other explanations, such as (1) the spontaneous polarization P_S of the PT whose polarization direction is along the *c* axis, and (2) the ferroelectricity of the PT, which is in the ferroelectric phase at RT and in the paraelectric phase at 1000 K. To further confirm the origin of the *c*-axis oriented, another typical perovskite material, BiT, was chosen and then deposited by AD method.

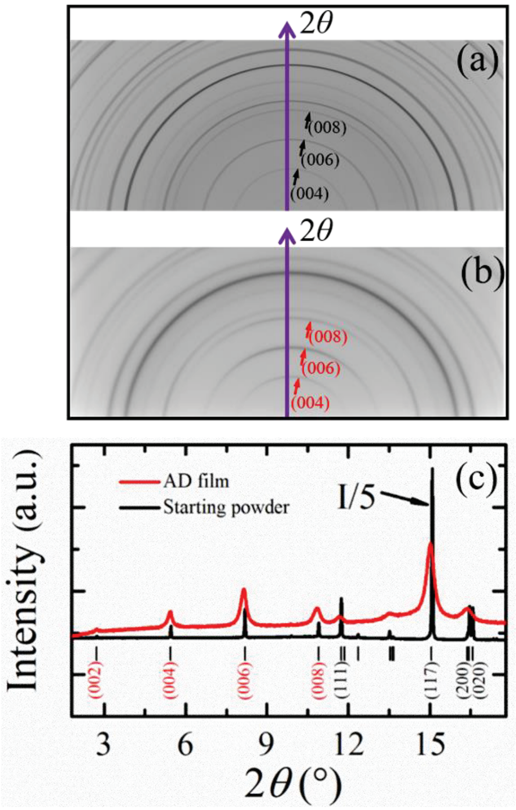

Fig. 4-8. Debye-Scherrer patterns of (a) BiT starting powder and (b) BiT as-deposited film at RT. (c) SXRD profiles indicated by arrows in (a) and (b). AD film and starting powders indicated by red and black lines, respectively. The peak of AD film with relatively stronger intensity, (004), (006), and (008), colored by red.

As shown in Fig. 4-8 (a) and (b), Debye-Scherrer patterns of the BiT starting powders and the as-deposited AD film were recorded on IP detector at RT, respectively. As similar to the PT starting powders, the intensity distribution of Debye-Scherrer rings of the BiT starting powders exhibits homogenous characteristic, implying that the BiT starting powders are randomly oriented. Meanwhile, similar to PT as-deposited AD film, the intensity distribution of (00*l*) Debye-Scherrer rings of the BiT as-deposited AD film, such as (004), (006), and (008), is not uniform at RT, indicating that the BiT AD film has the preferred orientation along the *c*-axis. Since the BiT AD film is measured by tilting the film sample 1° along the incident X-ray direction, the diffraction peaks indicated by red arrows in Fig. 4-8 (b), such as the (004) diffraction peak, are approximately parallel to the film surface. This observation in the BiT as-deposited AD film is also similar to that in the PT as-deposited AD film. SXRD profiles of the BiT starting powders and the as-deposited AD film along the 2θ direction in Fig. 4-8 (a) and (b) are drawn in black and red solid lines in Fig. 4-8 (c), respectively. To obtain a better visualized comparison, the intensity of BiT starting powders was divided by 5. As shown in Fig. 4-8 (c), the intensity of the (111) peak of the starting powders is stronger than that of (004), (006), and (008), while is opposite in the AD film, i.e., the intensity of (004), (006), and (008) peaks of the AD film are stronger than that of (111) peak. This observation also suggests that the (00*l*) diffraction peaks are relatively stronger in the BiT AD film, indicating that BiT as-deposited AD film exhibits the preferred orientation along the direction of *c*-axis.

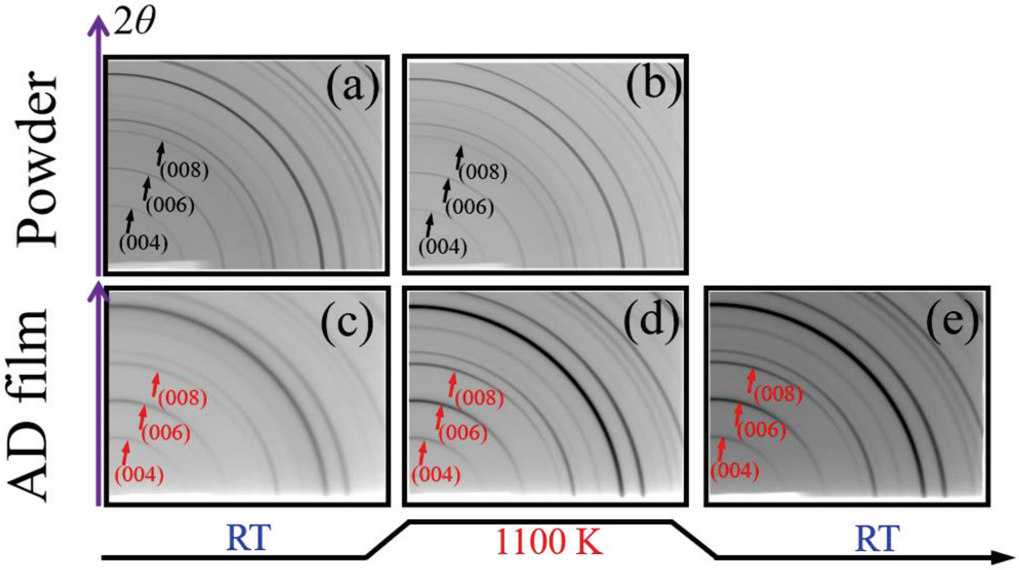

Fig. 4-9. Enlarged images of Debye-Scherrer rings of BiT starting powders at (a) RT and (b) 1100 K; and of BiT AD film at (c) RT, (d) 1100 K, (e) RT after heating/cooling cycle.

Then, the enlarged images of the Debye-Scherrer rings of the BiT starting powders and the AD film at RT and 1100 K are displayed in Fig. 4-9. The labels RT0 and RT1 represent the data measured at RT in the as-deposited state and RT after heating, respectively. As shown in Fig. 4-9 (a) and (b), respectively, it is clearly demonstrated that the intensity distribution of Debye-Scherrer patterns of BiT starting powders is uniform not only at RT but also at 1100 K, proving that the BiT starting powders are randomly oriented. This observation in the BiT starting powders is the same as that in the PT starting powders. Meanwhile, Fig. 4-9 (c), (d), and (e) show the Debye-Scherrer patterns of the BiT AD film at RT0, 1100 K, and RT1, respectively. As shown in Fig. 4-9 (c), (d) and (e), the intensity distribution of the Debye-Scherrer rings for the (00*l*) peaks in the AD film is not uniform indicated by the red arrows. These Debye-Scherrer rings maintain the same degree inhomogeneous at RT0, 1100 K, and RT1. This interesting observation suggests that the *c*-axis oriented of the BiT AD film occurs not only at RT0, but also at 1100 K and RT1, which is different from the PT AD film.

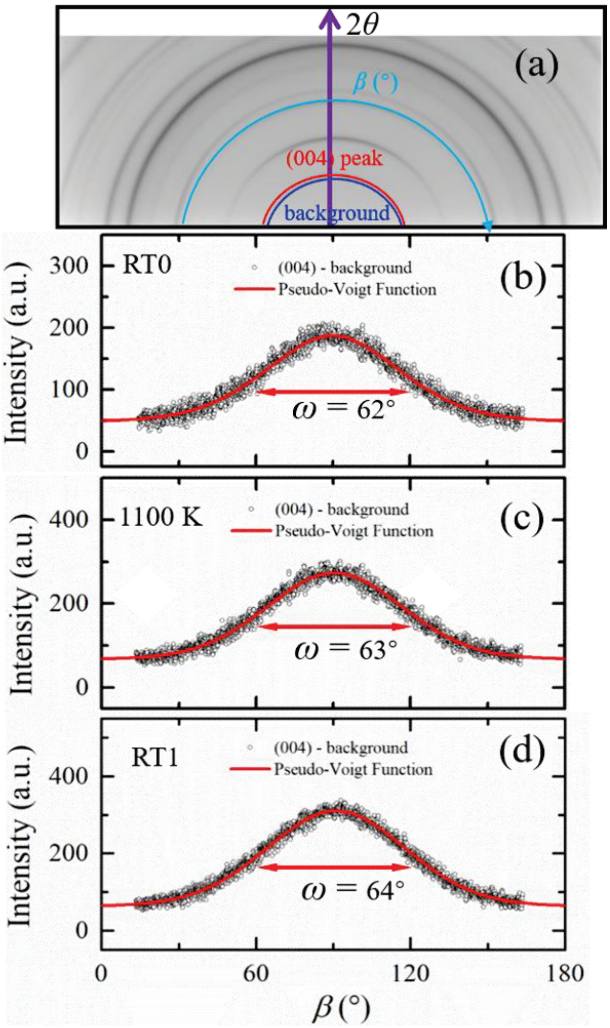

Fig. 4-10. Intensity distribution of (004) Debye-Scherrer ring of BiT AD film. (a) Debye-Scherrer patterns of BiT as-deposited AD film. Fitting results of (004) Debye-Scherrer ring intensity distribution using Pseudo-Voigt function at (b) RT in the as-deposited state (RT0), (c) 1100 K, and (d) RT after heating /cooling process (RT1). Red and blue lines shown in Fig. 4-10 (a) is the (004) Debye-Scherrer ring and the related background, respectively.

To evaluate the degree of preferred orientation of the BiT AD film at RT0, 1100 K, and RT1, as shown in Fig. 4-10, factor *A* was carried out using the program IPAnalyzer. As mentioned above, the degree of preferred orientation *A* = (180 - *w*)/180. For the Debye-Scherrer ring of the (004) peak, the values of *w* are 62°, 63° and 64° at RT0, 1100 K and RT1 respectively. As shown in Fig. 4-10 (b), (c) and (d), the values of *w* are approximately the same at these temperatures. Thus, the values of the degree of preferred orientation *A* are 65%, 65%, and 64% at RT0, 1100 K, and RT1, respectively. This evidence suggests that the preferred orientation of BiT AD film remains constant and exhibits temperature-independent properties despite different temperature conditions. To confirm this characteristic, the degree of preferred orientation of Debye-Scherrer ring of the (008) peak is shown in Fig. 4-11. As shown in Fig. 4-11 (a), (b), and (c), the values of *w* are 66°, 66°, and 67° at RT0, 1100 K and RT1, respectively. Therefore, the values of the degree of preferred orientation *A* are 63%, 63%, and 63% at RT0, 1100 K, and RT1, respectively. This result observed in the Debye-Scherrer ring of the (008) peak verifies that the results in the Debye-Scherrer ring of the (004) peak are correct at these temperatures.

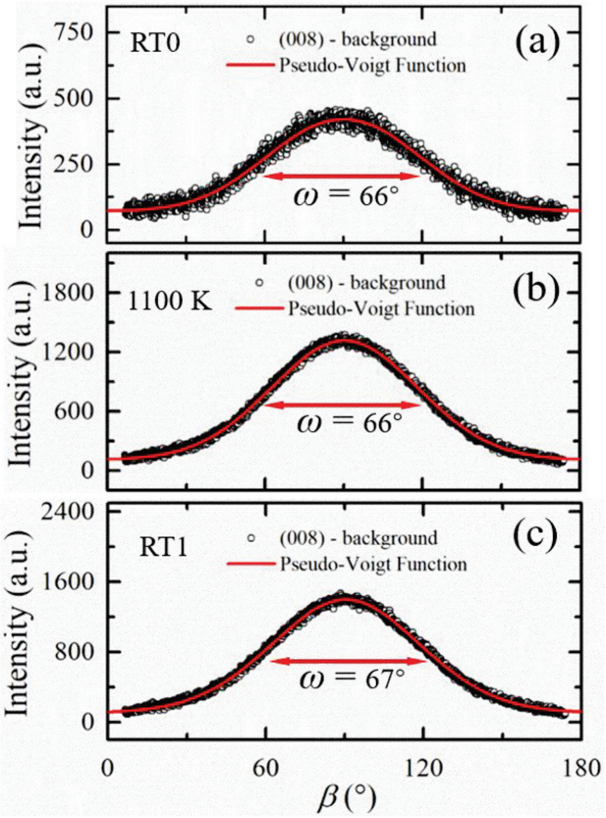

Fig. 4-11. Intensity distribution of (008) Debye-Scherrer ring of BiT AD film. Fitting results of (008) Debye-Scherrer ring intensity distribution using Pseudo-Voigt function at (a) RT0, (b) 1100 K, and (c) RT1.

To elucidate the origin of the preferred orientation in BiT AD film, crystal structure and charge density distribution should be considered. To obtain high quality SXRD data, these data were collected by IP detector using the X-rays of 0.35482 Å. Thus, under these conditions, the crystal structures of BiT starting powders were refined by the Rietveld method at RT and 1100 K, as shown in Fig. 4-12 (a) and (b), respectively. Crystal structure parameters at RT and 1100 K are detailed in Table 4-2 and Table 4-3.

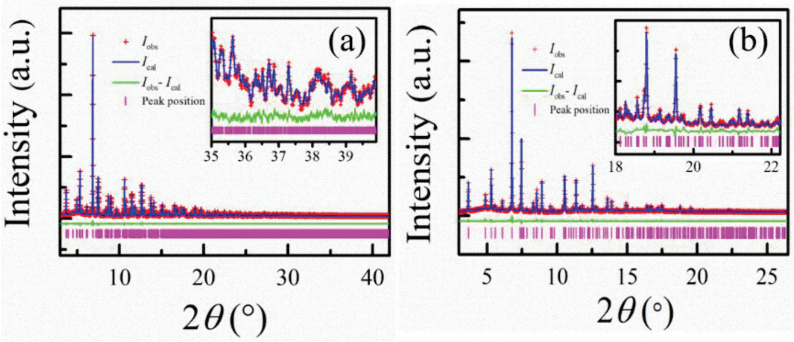

Fig. 4-12. Rietveld refinement of profile fitting results of BiT starting powders at (a) RT and (b) 1100 K. Red daggers and blue solid line indicate the observed and calculated diffraction intensity, respectively. Green solid line denotes the difference between the observed and the calculated intensity. Magenta solid line is the Bragg peak position.

Table 4-2. Structural parameters of $Bi_4Ti_3O_{12}$ starting powders at RT. Space group: *B*2*cb*, *a* = 5.4423 (1) Å, *b* = 5.4036 (1) Å, *c* = 32.7896 (6) Å. R_{wp} : 1.84%, R_I : 2.05%, R_F : 2.18%, where R_{wp}, R_I, and R_F are reliability factors (*R*-factor) based on the weighted profiles, Bragg intensities, and structure factors, respectively.

Atom	*x*	*y*	*z*	U_{11} (Å^2)	U_{22} (Å^2)	U_{33} (Å^2)
Bi(1)	0.00000	0.9974(2)	0.06676(1)	0.0080(3)	0.0101(5)	0.0076(7)
Bi(2)	0.9997(7)	0.0190(1)	0.21129(1)	0.0102(3)	0.0087(5)	0.0118(9)
Ti(1)	0.040(1)	0.00000	0.50000	0.002(2)	0.002(3)	0.01(1)
Ti(2)	0.0476(8)	0.996(1)	0.37173(7)	0.007(1)	0.012(2)	0.008(5)
O(1)	0.320(2)	0.252(2)	0.0079(4)	0.01(2)	0.01(4)	0.005(3)
O(2)	0.249(6)	0.267(6)	0.2467(5)	0.01(4)	0.004(4)	0.01(9)
O(3)	0.086(1)	1.054(2)	0.4381(3)	0.02(1)	0.001(6)	0.07(3)
O(4)	1.041(3)	0.946(3)	0.3175(2)	0.004(7)	0.003(9)	0.02(4)
O(5)	0.295(3)	0.230(2)	0.11147(3)	0.005(9)	0.006(1)	0.006(9)
O(6)	0.151(2)	0.212(2)	0.8746(3)	0.002(8)	0.01(4)	0.08(8)

Table 4-3. Structural parameters of $Bi_4Ti_3O_{12}$ starting powders at 1100 K. Space group: *I*4/*mmm*, *a* = 3.8568 (1) Å, *c* = 33.240 (1) Å. R_{wp} : 2.02%, R_I : 2.96%, R_F : 3.83%.

Atom	*x*	*y*	*z*	U_{11} (Å^2)	U_{22} (Å^2)	U_{33} (Å^2)

Bi(1)	0.50000	0.50000	0.06720(4)	0.057(1)	= U_{11}	0.062(1)
Bi(2)	0.50000	0.50000	0.21131(3)	0.051(1)	= U_{11}	0.031(1)
Ti(1)	0.50000	0.50000	0.50000	0.008(4)	= U_{11}	0.014(6)
Ti(2)	0.50000	0.50000	0.3711(1)	0.017(3)	= U_{11}	0.025(6)
O(1)	0.50000	0.00000	0.00000	0.04(2)	0.008(4)	0.17(3)
O(2)	0.50000	0.00000	0.25000	0.01(1)	= U_{11}	0.12(2)
O(3)	0.50000	0.50000	0.4401(2)	0.10(1)	= U_{11}	0.003(7)
O(4)	0.50000	0.50000	0.3163(3)	0.07(1)	= U_{11}	0.03(2)
O(5)	0.50000	0.00000	0.1179(2)	0.022(6)	0.01(4)	0.06(1)

As shown in Fig. 4-13, the crystal structure of BiT starting powders at 1100 K exhibits a layered structure consisting of Ti(1)-O$_6$ layer, Ti(2)-O$_5$ layer, Bi(2)-O$_4$ layer, Ti(2)-O$_5$ layer alternatively stacked along *c*-axis. To further elucidate the origin of the layered structure, the electron charge density distribution is studied. As shown in Fig. 4-14 (a) and (b), respectively, the 2D maps of the charge density distribution of BiT starting powders in the (100) and (200) planes provide direct evidence of the layered structure at 1100 K. Electron orbital hybridization between the Bi(2) and O(2) atoms leads to Bi(2)-O(2) covalent bonds. Further, the covalent bond of Bi(2)-O(2) forms a 2D network Bi(2)-O$_4$ layer. For the same reason, the Ti(2)-O$_5$ layer consists of Ti(2)-O(5) covalent bonds and Ti(2)-O(4) covalent bonds, while the Ti(1)-O$_6$ layer consists of Ti(1)-O(1) covalent bonds and Ti(1)-O(3) covalent bonds. Therefore, at 1100 K, Ti(1)-O$_6$, Ti(2)-O$_5$, Bi(2)-O$_4$ and Ti(2)-O$_5$ layers alternately stacked along the *c*-axis, forming the layered crystal structure shown in Fig. 4-13. In this scenario, Ti(1) is present with 6-fold oxygen coordination while Ti(2) is 5-fold oxygen coordination. Difference in the oxygen coordination is due to the different chemical environment around Ti(1) and Ti(2). Ti(1) is surrounded by 8 Bi(1) ionic state ions, while Ti(2) is surrounded by 4 Bi(1) ionic state ions and 4 Bi(2) covalent state ions. For Ti(2) atom, the 4 Bi(2) covalent state ions located in Bi(2)-O$_4$ layer lead to the atom of Ti(2) shift to the direction of Bi(2)-O$_4$ layer. As a result, the bond of Ti(2)-O(3) becomes longer, leading to the disappearance of the hybridization. Finally, around Ti(2) is a 5-fold ligand of oxygen.

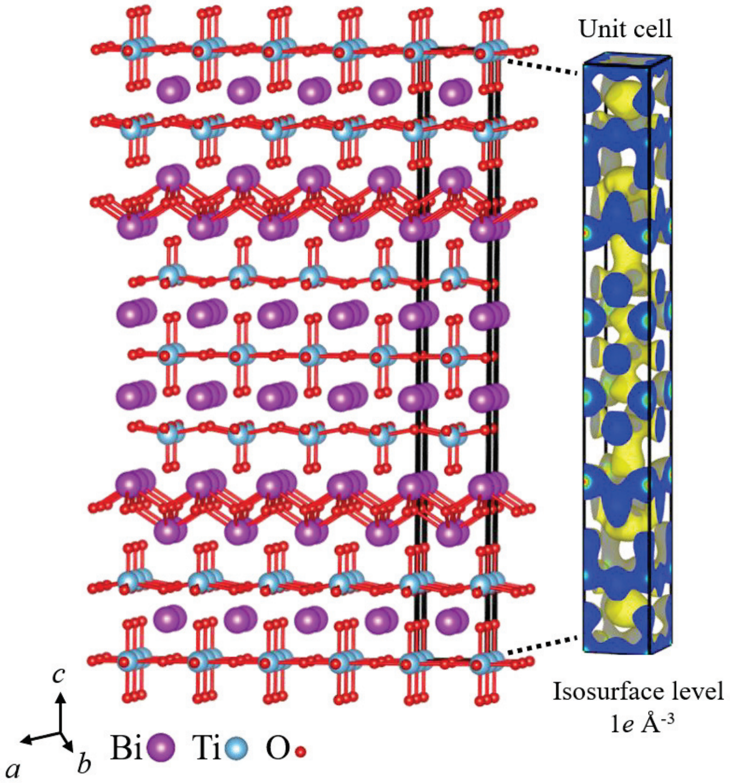

Fig. 4-13. Crystal structure of BiT starting powder and related 3D charge density distribution in unit cell at 1100 K. The isosurface level of the unit cell is 1 *e* Å^{-3}.

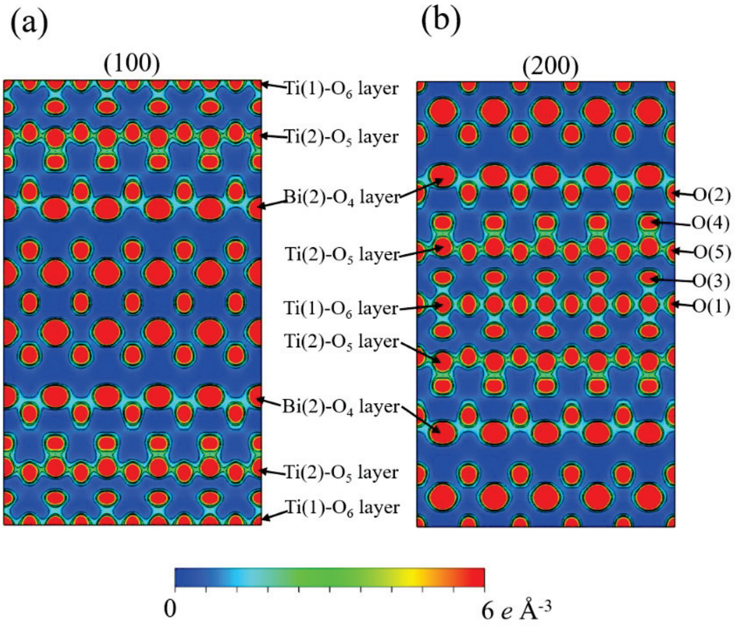

Fig. 4-14. 2D electron charge density of BiT starting powders at 1100 K on (a) (100) plane and (b) (200) plane. The contour lines are drawn from 0 *e* Å^{-3} to 6 *e* Å^{-3} with 0.5 *e* Å^{-3} intervals.

To confirm that the layered structural characteristic still exist at RT, the crystal structure and electron charge density distribution of BiT starting powders at RT are also determined by the MEM/Rietveld method. As shown in Fig. 4-15, the crystal structural characteristics of BiT starting powders also exhibit a layered structure consisting of Ti(1)-O$_6$ layer, Ti(2)-O$_4$ layer, Bi(2)-O$_2$ layer, Ti(2)-O$_4$ layer alternatively stacked along *c*-axis at RT. Next, to confirm the origin of the layered crystal structure of the BiT starting powders at RT, the 2D maps of electron charge density distribution in the (220) and (110) planes are plotted in Fig. 4-16 (a) and (b), respectively. As shown in Fig. 4-16, the covalent bonds of Ti(1)-O(1) and Ti(1)-O(3) form a network structure of Ti(1)-O$_6$ layer, while the covalent bonds of Ti(2)-O(4), Ti(2)-O(5) and Ti(2)-O(6) generate a 2D structure of Ti(2)-O$_4$ layer. From 1100 K cooling to RT, the octahedron TiO$_6$ is tilting, which can be described as $a^-a^-c^0$ in Glazer notation. Thus, at 1100 K, 4 Ti(2)-O(5) covalent bonds of the same bond length (1.96 Å) split into two types of bonds at RT, namely two Ti(2)-O(5) bonds and two Ti(2)-O(6) bonds. At RT, the bond lengths of the two Ti(2)-O(5) bonds are 1.93 Å and 2.04 Å, and the bond lengths of the two Ti(2)-O(6) bonds are 1.66 Å and 2.48 Å, respectively. As a result, the long bond length of Ti(2)-O(6) bond, 2.48 Å, leads to its ionic state. Thus, around the Ti(2) atom is a 4-fold oxygen coordination, forming a Ti(2)-O$_4$ layer at RT. Although octahedron Ti(2)O$_6$ is composed of six Ti(2)-O bonds, one Ti(2)-O(3) bond, one Ti(2)-O(4) bond, two Ti(2)-O(5) bonds, and two Ti(2)-O(6) bonds. From the viewpoint of electron charge density distribution, the minimum charge density of Ti(2)-O(3) bond and Ti(2)-O(6) bond (the long one) is 0.46 e Å^{-3} and 0.38 e Å^{-3}, respectively, indicating their major electron states are ionic state. While the minimum charge densities of Ti(2)-O(4) bond, two Ti(2)-O(5) bonds (1.93 Å and 2.04 Å) and Ti(2)-O(6) bond (the short one) are 1.44 e Å^{-3}, 1.04 e Å^{-3}, 0.80 e Å^{-3} and 1.75 e Å^{-3}, respectively, indicating that their major electron states are covalent. Thus, the covalent bonds of one Ti(2)-O(4) bond, two Ti(2)-O(5) bonds (1.93 Å and 2.04 Å) and one Ti(2)-O(6) bond (the short one) form a Ti(2)-O$_4$ layer at RT. At the same time, the covalent bond of Bi(2)-O(2) forms a 2D network structure Bi(2)-O$_2$ layer. At 1100 K, the network structure of Bi(2)-O$_4$ layer is composed of 4 Bi(2)-O(2) covalent bonds. However, due to the Glazer tilt, 4 Bi(2)-O(2) covalent bonds (2.317 Å) split into two short Bi(2)-O(2) bonds and two long Bi(2)-O(2) bonds at RT. The elongated bond length of the two long Bi(2)-O(2) bonds comes from the decreased hybridization between the Bi(2) and O(2) atoms. Thus, there are two Bi(2)-O(2) covalent bonds at RT and a Bi(2)-O$_2$ layer is formed. As a result, Ti(1)-O$_6$, Ti(2)-O$_4$, Bi(2)-O$_2$ and Ti(2)-O$_4$ layers are alternately stacked along the *c*-axis at RT, forming the layered crystal structure shown in Fig. 4-15.

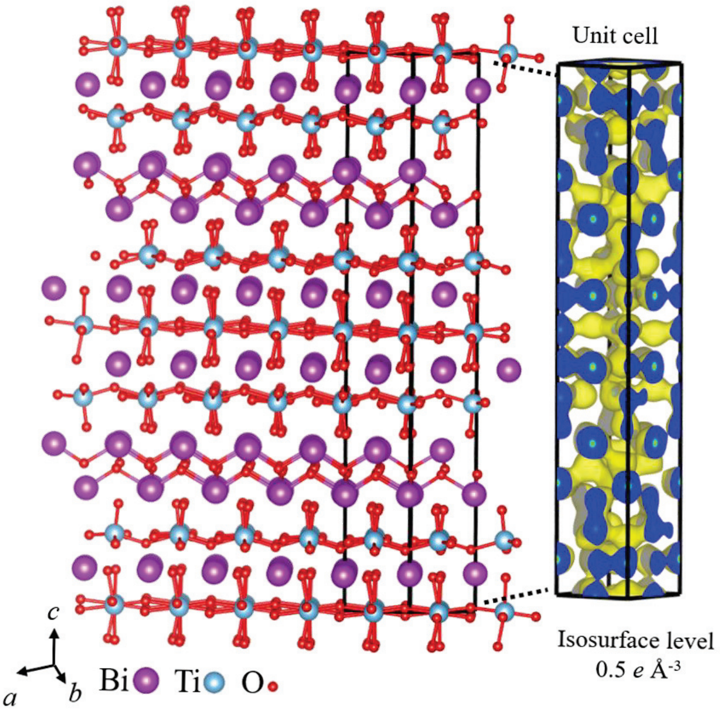

Fig. 4-15. Crystal structure of BiT starting powders and related 3D charge density distribution in unit cell at RT. The isosurface level of the unit cell is 1 e Å^{-3}.

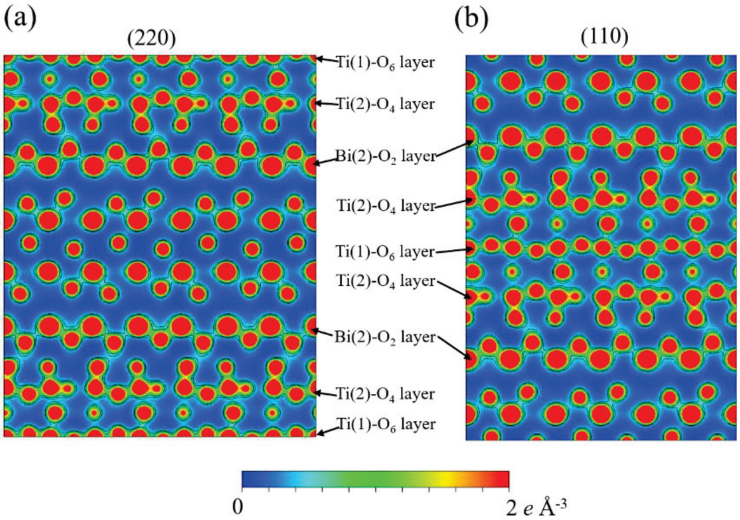

Fig. 4-16. 2D electron charge density of BiT starting powders at RT on (a) (100) plane and (b) (200) plane. The contour lines are drawn from 0 e Å^{-3} to 6 Å^{-3} with 0.5e Å^{-3} intervals.

As shown in Fig. 4-16, Ti(2)-O$_4$ layer seems is not continuous along [110] direction at RT. As mentioned above, the [110] direction of BiT at RT is equal to the [100] direction at 1100 K. Cooling from 1100 K to RT, octahedral TiO_6 tilts, causing the Ti(2)-O(5) bond to deviate from the ideal orientation [110] direction. To investigate the precise structure of Ti(2)-O_4 layer, the 2D maps of charge density distribution of Ti(2)-O_4 layer and Ti(1)-O_6 layer are shown in Fig. 4-17 (a) and (b), respectively. The isosurface level of the 2D map is 0.6 e $Å^{-3}$. The direction of $\boldsymbol{a}_o$ is [110] direction at RT. As shown in Fig. 4-17 (b), it is natural to consider that the Ti(1)-O_6 layer is composed of a 2D network structure. Meanwhile, as shown in Fig. 4-17 (a), although not continuous along [110] direction, the 2D map of the charge density distribution of the Ti(2)-O_4 layer provides evidence that the Ti(2)-O_4 layer is composed of 1D chain. Thus, the structure of Ti(2)- O_4 is a layered structure. Therefore, from the point of view of charge density distribution, BiT starting powders are also composed of a layered structure at RT.

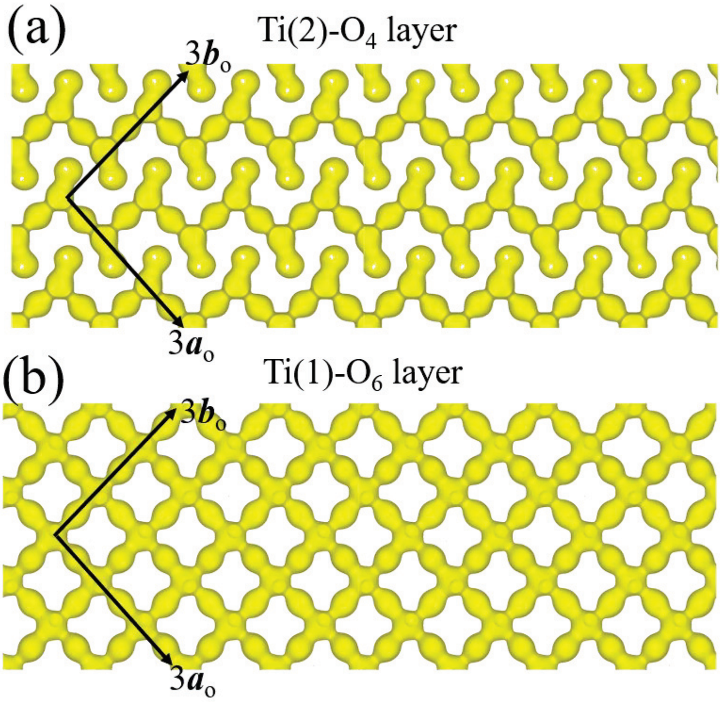

Fig. 4-17. 2D electron charge density of BiT starting powders at RT on (a) Ti(2)-O_4 layer and (b) Ti(1)-O_6 layer. The isosurface level of the 2D electron charge density distribution is 0.6 e $Å^{-3}$.

To confirm that the charge density distribution analysis of the BiT starting powders at 1100 K and RT is correct, the bond valence sum (BVS)[137,138] was calculated. The details show in Table 4-4. The bond valence parameters B and r_0 of Bi ions are 0.48 and 1.99, and those of Ti ions are 0.37 and 1.815, respectively. In this calculation, the valences of Bi(1), Bi(2), Ti(1) and Ti(2) ions at 1100 K are 2.57, 2.66, 4.17 and 3.90, respectively. While the valences of Bi(1), Bi(2), Ti(1) and Ti(2) ions at RT are 3.14, 3.01, 3.97 and 4.38, respectively. These calculations do not deviate much from the formal valences of 3+ and 4+ for Bi and Ti, proving that the charge density distribution analysis of BiT starting powders is successful at 1100 K and at RT.

Table 4-4. Bond valence sums are calculated from the selected bond lengths of BiT at RT and 1100 K. The unit of bond length is Å. The abbreviation of valence is **V** listed in this table.

	RT	1100 K
Bi(1)-O(1)	2.95392	2.95104 × 4
Bi(1)-O(1)	2.55996	
Bi(1)-O(1)	2.93589	
Bi(1)-O(1)	3.28488	
Bi(1)-O(3)	3.06671	2.73753×4
Bi(1)-O(3)	3.22337	
Bi(1)-O(3)	2.43431	
Bi(1)-O(3)	2.26147	
Bi(1)-O(5)	2.35378	2.56875×4
Bi(1)-O(5)	2.51061	
Bi(1)-O(6)	2.37746	
Bi(1)-O(6)	3.10842	
V	**3.14**	**2.57**
Bi(2)-O(2)	2.35655	2.31666×4
Bi(2)-O(2)	2.50676	
Bi(2)-O(2)	2.11098	
Bi(2)-O(2)	2.23763	
Bi(2)-O(4)	2.50651	2.87027×4
Bi(2)-O(4)	2.67246	
Bi(2)-O(4)	3.10734	
Bi(2)-O(4)	3.24678	
Bi(2)-O(6)	3.19487	
V	**3.01**	**2.66**
Ti(1)-O(1)	2.02003×2	1.92843×4
Ti(1)-O(1)	1.85399×2	
Ti(1)-O(3)	2.06307×2	1.99644×2
V	**3.97**	**4.17**
Ti(2)-O(3)	2.22011	2.30957
Ti(2)-O(4)	1.78974	1.82559

Ti(2)-O(5)	1.92954	1.96461×4
Ti(2)-O(5)	2.04306	
Ti(2)-O(6)	1.65674	
Ti(2)-O(6)	2.47583	
V	**4.38**	**3.90**

It is known that the P_S of BiT is along the *a*-axis, while the P_S of PT is along the *c*-axis. However, the AD films of both BiT and PT are *c*-axis oriented, which means that the P_S is not the origin of the preferred orientation. Meanwhile, at high temperature, both BiT and PT are the paraelectric phases (1000 K for PT and 1100 K for BiT). However, the preferred orientation of the BiT AD film remains at 1100 K, while the preferred orientation of the PT AD film vanishes at 1000 K. These results provide a directly evidence that the P_S and ferroelectricity are not the original reason of the preferred orientation. The charge density distributions of the BiT starting powders at RT and 1100 K indicate that the BiT is a layered structure consisting of Bi-O and Ti-O layers stacked along the *c*-axis not only at RT but also at 1100 K. Thus, the layered structure of BiT is the origin of the preferential orientation along the *c*-axis that occurs in BiT AD films at RT0, 1100 K and RT1.

Based on this result, we can consider that the crystal structure with layered characteristics plays a crucial role in the film growth of BiT AD film. That is, during the deposited process, the particles of BiT powders preferentially recombine along a certain layer (*ab* plane), while the interlayer connection between Bi-O and Ti-O layers is weak and easily cleaved and deformed. Therefore, the BiT AD film exhibits a preferred orientation along *c*-axis. Finally, it is clear that the film growth mechanism of PT and BiT is a layered structure at the deposited temperature.

4.2 Phase transition behavior in $PbTiO_3$ and $Bi_4Ti_3O_{12}$ AD films

4.2.1 Upshift of phase transition temperature

Thermal stability plays an important role for ferroelectric thin films in industries, especially in high-temperature applications. Herein, firstly, Debye-Scherrer patterns of PT AD film were recorded on a flat IP detector at several different temperatures to examine the phase transition behavior during heating and cooling process. To clearly show the phase transition from tetragonal to cubic phases, the 2D Debye-Scherrer pattern was transformed into 1D profiles of XRD patterns. As illustrated in Fig. 4-18 (a), it is interesting to note that the peak shapes corresponding to the (111), (002), and (200) peaks of the AD film gradually become sharper and the peak intensities become stronger as the temperature increases. This observation is also consistent with the phenomenon in Fig. 4-4. For the AD film in Fig. 4-4, the peak width of the Debye-Scherrer ring becomes sharper at RT1 and RT2 and the peak intensity increases compared to RT0.

We note, phase transition temperature T_C of the PT AD film is about 900 K during the first heating process, which is much higher than that of the bulk (763 K),[48] about 750 K for the first cooling process, and about 750 K for the second heating process. Tetragonal-ferroelectric transition temperature of the AD film shifts to a higher temperature and exhibits a better thermal stability property for tetragonal phase, indicating that the film deposited by AD method can be applied to high temperature fields. T_C of the cooling and the second heating processes is approximately the same as that of bulk. Due to the large heating area (10×2 mm^2) and exposure to air, practical temperature of the AD film is lower than that of the heating gas, which is the measured temperature, during the heating and cooling process. This means that T_C of the AD film is slightly below 900 K during the first heating process.

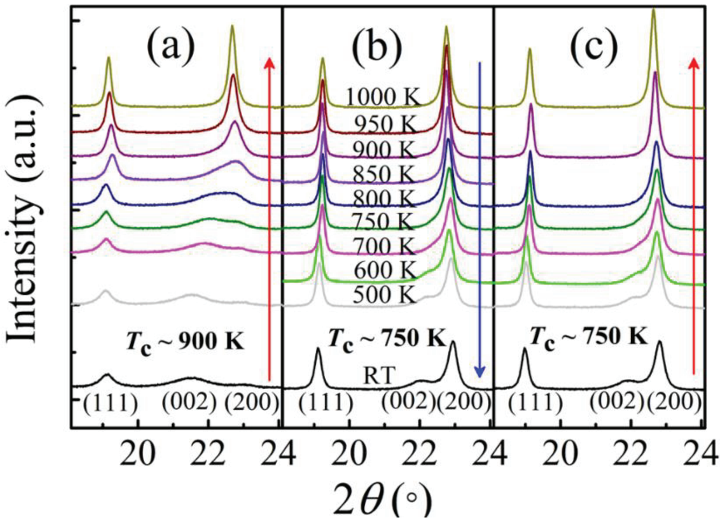

Fig. 4-18. Diffraction profiles of SXRD patterns of $PbTiO_3$ AD film recorded on flat IP detector. (a) shows the first heating process, (b) the first cooling process, and (c) the second heating process.

As plotted in Fig. 4-18 (a), (b) and (c), the degree of preferred orientation f can be roughly extracted from the intensity ratio of the (002) and (200) diffraction peaks. During the first heating process, the degree of preferred orientation f decreases as the temperature increases. As analyzed above, the preferred orientation disappears at cubic phase, hence, the preferred orientation cannot be observed during the cooling process and the second heating process, as shown in Fig. 4-18 (b) and (c). In order to estimate the correlation between preferred orientation and temperature, the degree of preferred orientation f of the AD film at several temperatures was calculated by using

Lorentz function during the first heating process. As shown in Fig. 4-19, the degree of preferred orientation does not change significantly from RT to 700 K. Then, as temperature increases further, the degree of preferred orientation decreases rapidly from 800 K. As can be observed in this figure, the tetragonal-cubic phase transition temperature can also be roughly determined to be around 900 K. In addition, since these data were recorded on a flat IP detector, unlike the IP detector, the preferred orientation calculated at RT is slightly different from that in Fig. 4-2.

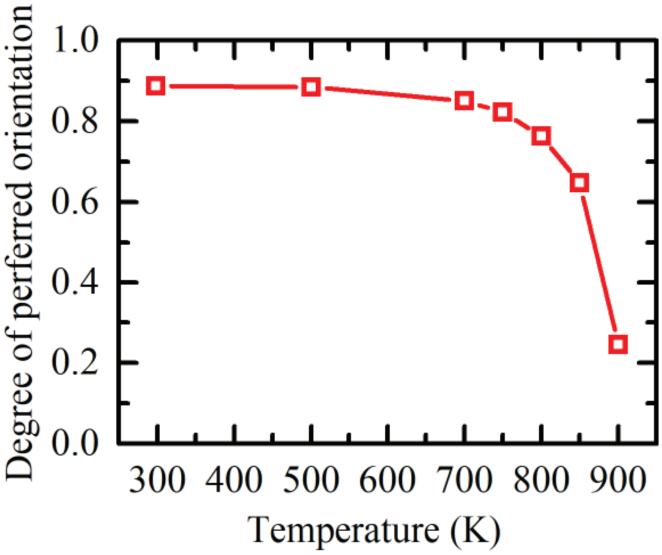

Fig. 4-19. Calculated degree of preferred orientation as a function of temperature at several temperatures during the first heating process. These several temperatures are RT, 500 K, 700 K, 750 K, 800 K, 850 K and 900 K, respectively.

Therefore, we next carried out temperature dependence SXRD experiments to precisely study the phase transition behavior of the self-supported films using an MYTHEN detector system. As a contrast experiment, phase transition behavior of PT starting powders was also determined. PT starting powders and the self-supported films, sealed in 0.1 mm diameter capillary, respectively, were heating from 300 K to 1000 K and then cooling to 300 K. In particular, the heating and cooling processes were performed two cycles in order to accurately determine the phase transition behavior of the self-supported films. As shown in Fig. 4-20 (a) and (b), T_C of the heating and cooling processes of the starting powders are 763 K and 758 K, respectively, which are in good agreement with other reports.[48] We note, as shown in Fig. 4-20 (c), the T_C of the self-supported films is 860 K during the first heating process, which is close to 100 K higher than that of the starting powders. In order to determine the value of T_c from the tetragonal phase to the cubic phase in the first heating process, the temperature dependence of the *d* values of the (111) peak of the starting powders and the self-supported films are shown in Fig. 4-21. These are derived from the (111) pattern of the starting powders and the self-supported films shown in Fig. 4-20. As shown in Fig. 4-21, the changes in the *d*-value indicate that the T_C of the starting powders and the self-supported films are 763 K and 860 K, respectively. Therefore, the T_C of the self-supporting films is 860 K during the first heating, which is also consistent with our analysis above regarding the T_C of the AD film. As for the cooling process and the second heating and cooling cycle, the T_c of the self-supported films is the same as that of the starting powders, as shown in Fig. 4-20 (d), (e), and (f), respectively.

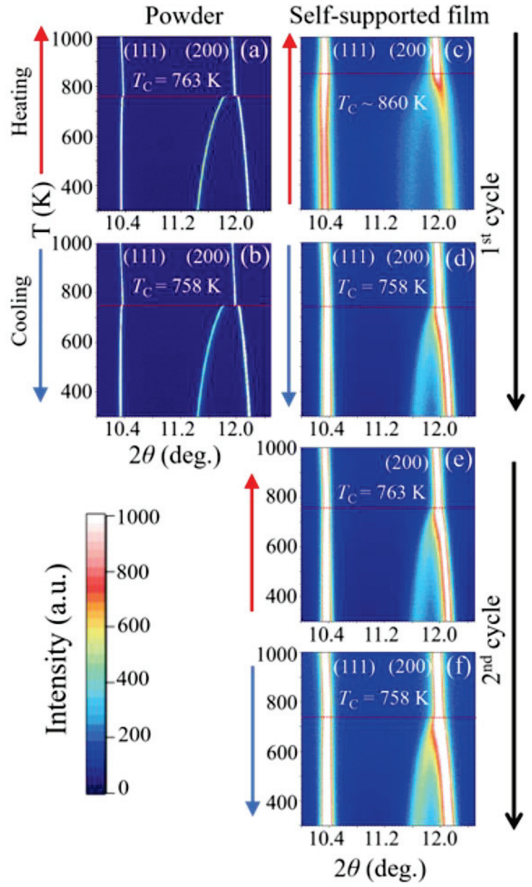

Fig. 4-20. Temperature dependence SXRD patterns of $PbTiO_3$. (a) the heating and (b) cooling processes for the starting powders. (c) the first heating and (d) first cooling processes for the self-supported films. (e) the second heating and (f) second cooling processes for the self-supported films.

Meanwhile, the peak width and the peak intensity of the self-supported films is broadened and weakened during the first heating process compared to the subsequent heating and cooling process. As shown in Fig. 4-18, we also note that the peak profiles of the AD film with broadened peak width and weakened peak intensity appear only during the first heating process and are not observed during the cooling and the second heating processes, similar to the self-supported films.

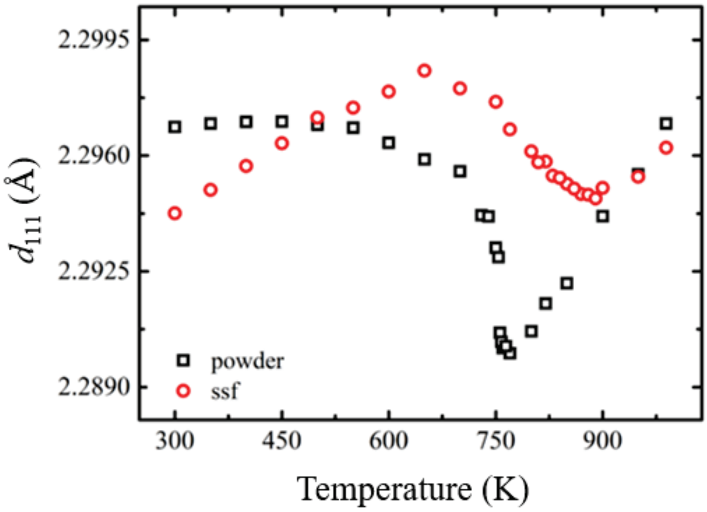

Fig. 4-21. Changes in the *d*-value of the (111) peak of the staring powders and the self-supported films as a function of temperature during the first heating process. Black rectangle and red circle indicate the starting powders and the self-supported films, respectively.

The T_C of BiT self-supporting films was also investigated. To precisely study the phase transition behavior, the temperature dependence SXRD experiments of BiT self-supported films were performed by heating from RT to 1100 K and then cooling to RT. As a contrast, the T_C of BiT starting powders is also measured. The heating and cooling processes of BiT self-supporting films were carried out twice in order to obtain the exact phase transition temperature. As plotted in Fig. 4-22 (a) and (b), the T_C of BiT starting powders are 972 K and 961 K during the heating and cooling processes, respectively, which are consistent with other published papers.[35] We also note, interestingly, the T_C of BiT self-supported films is about 1020 K during the first heating process shown in Fig. 4-22 (c), which is close to 50 K higher than that of the starting powders. Therefore, we concluded that the upward shift of T_C of the self-supported films deposited by AD method maybe is a common phenomenon. In addition, as shown in Fig. 4-22(d), (e) and (f), the T_C of BiT self-supporting films during the first cooling process and the second heating and cooling processes are 961 K, 972 K and 961 K, respectively, which are the same as that of the starting powders.

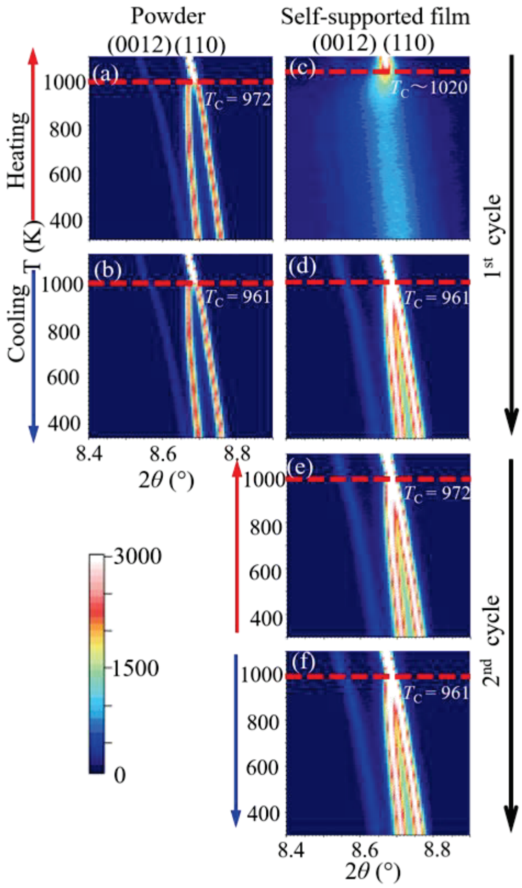

Fig. 4-22. Temperature dependence SXRD patterns of $Bi_4Ti_3O_{12}$. (a) the heating and (b) cooling processes for the starting powders. (c) the first heating and (d) first cooling processes for the self-supported films. (e) the second heating and (f) second cooling processes for the self-supported films.

4.2.2 Origin of enhanced phase transition temperature

As analyzed above, the phase transition behaviors of PT self-supporting films and BiT self-supporting films exhibit the same features, i.e., the T_C increases during the first heating process and returns to the same value of the starting powders during the subsequent cooling and heating processes. Thus, this observation suggests that the mechanism of the T_C upshift of PT self-supported films and BiT self-supported films are the same. In order to extract a clue to the phase transition behavior, it is natural to consider the changes of the peak width and peak intensity of PT self-supported films and BiT self-supported films during the first heating process. During the first heating process, both self-supported films exhibit a weakened peak intensity and a broadened peak width.

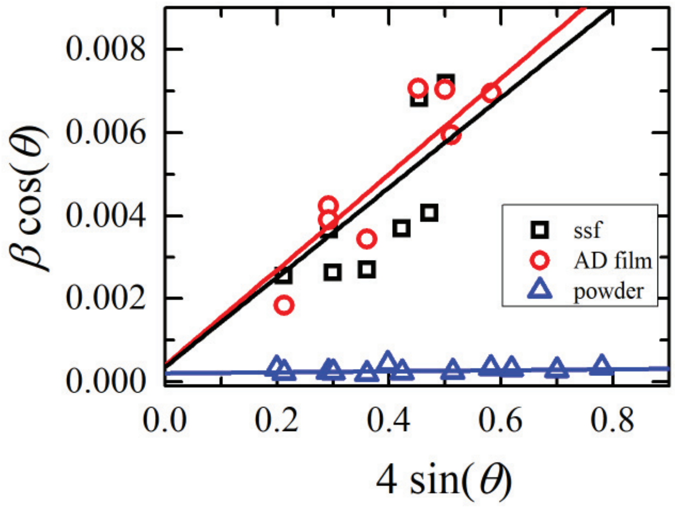

Fig. 4-23. Linear correlation between βcos(θ) and 4sin(θ) for PT samples at RT calculated from the Williamson-Hall equation. Black rectangle, red circle and blue triangle indicate the self-supported films, the AD film and the starting powders, respectively. For PT AD film and PT self-supported films, the RT is RT in the as-deposited state (RT0).

There are several reasons should be considered to explain the weakening of the peak intensity and the broadening of the peak width, such as the reduction of grain size, the residual or intrinsic stress (or strain) and the diffuse scattering. First, the relationship between the weakening of peak intensity (and the broadening of peak width) and the residual stress of PT AD film and PT self-supported films was investigated by the Williamson-Hall method. Based on the Williamson-Hall method shown in Fig. 4-23, we calculate that the stress in the AD films is the same as in the self-supported films and about 40 times higher than that of the starting powders, which indicates that there are enormous stresses in these films. In many published papers, they also reported the presence of high residual stresses in AD films, such as 800 MPa for $BaTiO_3$ AD films as reported by Neamul H. Khansur.[79] The weakening of the peak intensity and the broadening of the peak width in the PT AD film and the self-supported films come from the residual stress, which are mainly from the intrinsic stress generated by the atomic impact during the deposition process. In addition, according the Williamson-Hall equation, the grain size can be calculated. The grain sizes of PT AD film, PT self-supported films and PT starting powders are 100, 100 and 1500 nm, respectively. The high stresses will lead to the upshift of T_C in PT films, such as Zhang et al. obtained PT film with giant high T_C (725 °C) using interphase strain method.[140] For the self-supported films, the rapid shrinkage of the *c*-axis during the first heating process is suppressed by the stress, as shown in Fig. 4-24 (b), leading to T_c shift to the high-temperature side.

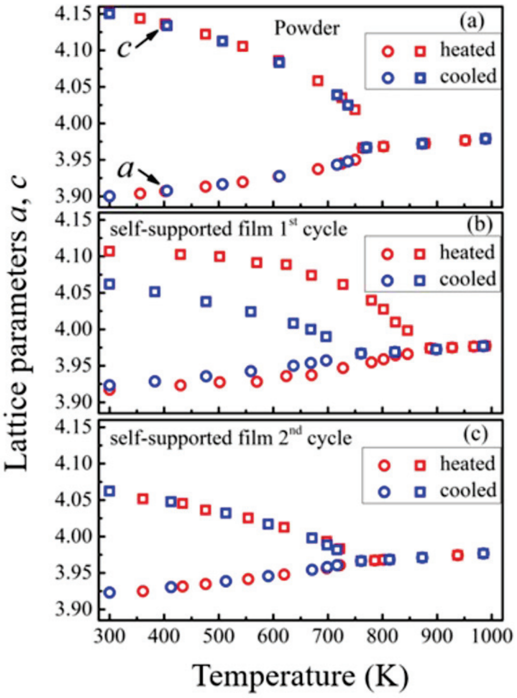

Fig. 4-24. Lattice parameters *a* and *c* as a function of temperature for $PbTiO_3$; (a) starting powders, self-supported films during (b) the first heating/cooling process, and (c) the second heating/cooling process. Red exhibits the heating process while blue indicates the cooling process; the circle represents lattice parameter *a* while the rectangle represents lattice parameter *c*.

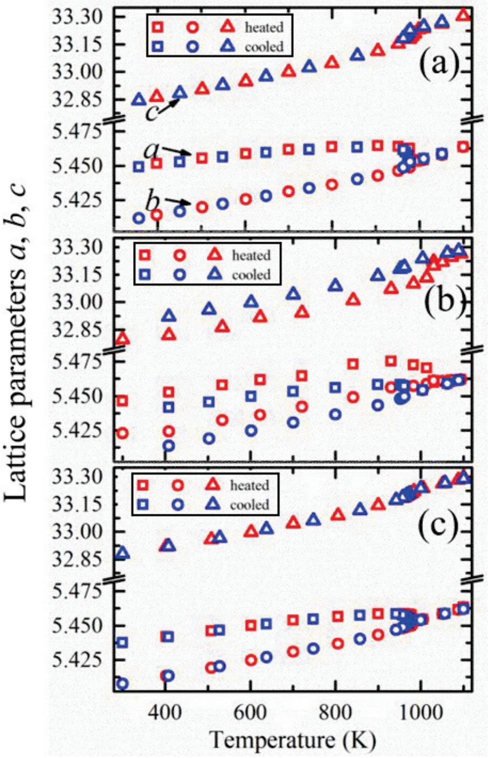

Fig. 4-25. Lattice parameters *a*, *b* and *c* as a function of temperature for $Bi_4Ti_3O_{12}$; (a) starting powders, self-supported films during (b) the first heating/cooling process, and (c) the second

heating/cooling process. Red exhibits the heating process while blue indicates the cooling process; the rectangle, circle and triangle represent lattice parameter *a*, *b* and *c,* respectively.

These observations provide a string to further understand the phase transition behavior of the self-supported films. Therefore, the residual stresses in the films from atomic impact during the deposition process is one reason why the T_C of the self-supported films is upward shift. The residual stress gradually released during the first heating process, hence, the phase transition behavior of the self-supported films replied to the same of the powders during the subsequent first cooling process and the second heating and cooling processes.

As shown in Fig. 4-20 (a) and (c), the peak position of the (002) peak of the self-supported films with a tetragonal phase is shifted to the right side compared to that of PT starting powders, indicating a contraction of the lattice parameter *c* in the self-supported films. Compared with Fig. 4-20 (c), we also note that the (002) peak of the self-supported films shifts to the right side during the second heating process shown in Fig. 4-20 (e), which indicates that the lattice parameter *c* of the self-supported films shrinks during the second heating process. The lattice parameters *a* and *c* of PT starting powders and PT self-supporting films as a function of temperature are shown in Fig. 4-24. As shown in Fig. 4-24 (a), the heating process and the cooling process of PT starting powders are reversible processes. However, as shown in Figure 4-24 (b), the lattice parameter *c* shrinks slightly from RT to about 600 K and then shrinks rapidly with further increase in temperature until the phase transition occurs at 860 K during the heating process. In addition, the lattice parameter *a* is linearly dependent on temperature during the heating process. The lattice parameter *a* increases slightly during the cooling process compared to the heating process, while the lattice parameter *c* shrinks significantly during the cooling process. As displayed in Fig. 4-25, the changes of the lattice parameters of BiT self-supported films are similar to those of the PT self-supported films. The heating and cooling processes of BiT starting powders are reversible processes. While the lattice parameters *a* and *b* of BiT self-supported films are contracted. Hence, we do not show details of the analysis of BiT self-supported films.

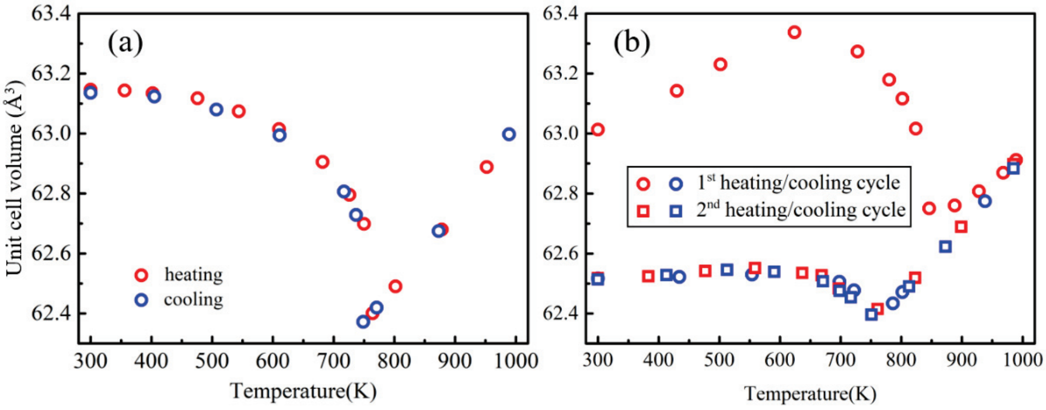

Fig. 4-26. Temperature dependence of the unit cell volume for (a) PT starting powders and (b) PT self-supported films.

Based on the lattice parameters, the temperature dependence of the unit cell volume for the PT starting powders and PT self-supported films is plotted in Fig. 4-26. As shown in Fig. 4-26 (a), the volume of PT starting powders exhibits a negative thermal expansion in tetragonal phase. In contrast, as shown in Fig. 4-26 (b), the volume of PT self-supported films in the tetragonal phase has about zero thermal expansion during the cooling process and the second heating and cooling processes. However, the temperature dependence features of the unit cell volume of BiT samples are different from those of PT samples. As shown in Fig. 4-27, not only in BiT starting powders but also in BiT self-supported films, the unit cell volume exhibits a linear relationship of the temperature in the range of RT to 1100 K. In addition, there is no obvious difference in the volume of the BiT starting powders and in the BiT self-supported films.

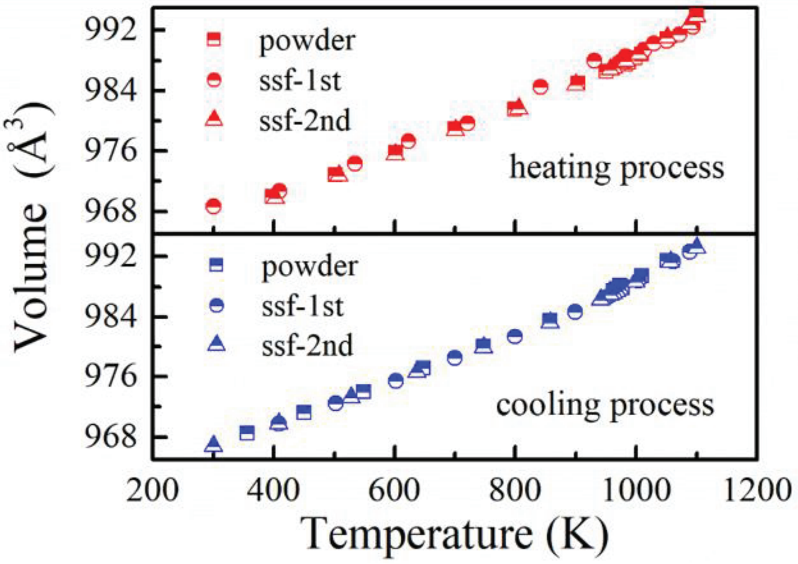

Fig. 4-27. Temperature dependence of the unit cell volume for the BiT starting powders and BiT self-supported films. The notation of "ssf-1st" and "ssf-2nd" means that is the first heating / cooling process for the self-supported films and the second heating / cooling process for the self-supported films.

For perovskite ferroelectric materials, T_c is also strongly coupled with tetragonality (c/a), such as high T_c usually means large c/a.[48] However, as plotted in Fig. 4-24, the c/a value of PT self-supported films (1.049 at RT0) is smaller than that of the powders (1.065), especially at RT1 and RT2 (1.035). In this scenario, the T_c of PT self-supported films, especially for the second process, should be lower than that of the powders, which can't be explained in this experiment. Meanwhile, we note, the average grain size of the self-supported films is about 100 nm, which is a significantly smaller than that of the powders (1.5 μm), will decrease the tetragonality (small c/a), which is also consistent with other published papers.[141] This means, for PT self-supported films, T_c is not so sensitive to the c/a variation derived from the grain size effect from 1.5 μm to 100 nm. This will help us to investigate the origin of high T_c in PT self-supported films. It is an important clue to focus on the value of the P_s calculated by the ionic model at RT0, RT1, and RT2 in the PT self-supported films. Although the grain size of the self-supported films at RT0 (100 nm) is smaller than that of RT1 (150 nm) and RT2 (150 nm), the value of c/a at RT0 (1.049) is larger than that of at RT1 (1.035) and RT2 (1.035). The large c/a at RT0 comes from the larger P_s (54 μC/cm^2) at RT0 compared to 43 μC/cm^2 at RT1 and RT2. As shown by the Landau theory relationship $T_C = \alpha P_S^2$,[49] the larger P_S at RT0 is one important factor to elucidate the higher T_c in the first heating process. In addition, crystal distortion produced by residual stresses leads to large P_S during the first heating and is coupled with an increase in unit cell volume. While during the subsequent cooling and heating processes, the stresses are released, the crystal distortion returns to the normal level, and the P_s decrease significantly, resulting in zero thermal expansion of PT self-supported films. However, the P_s value of BiT starting powders calculated by ionic model is 1.7 μC/cm^2. Hence, small P_s value cannot provide contribution to the upshift of the T_C of BiT self-supported films. On the other hand, small P_s value has no effect on the unit cell volume of BiT self-supported films, leading to the volume of BiT self-supported films is approximately the same as the volume of BiT starting powders.

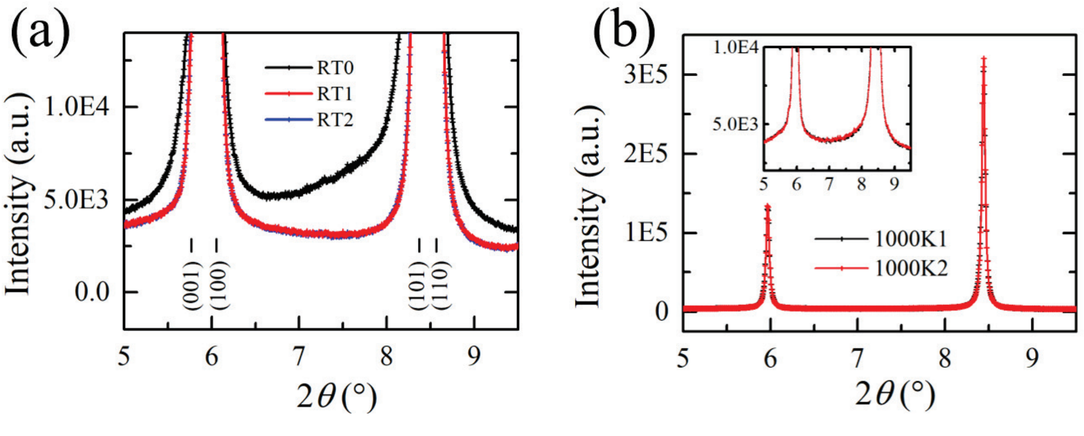

Fig. 4-28. Enlarged SXRD profiles of $PbTiO_3$ self-supported films at (a) RT and (b) 1000 K. RT in the as-deposited state shown in black line, labeled as RT0. While RT after the first heating/cooling process shown in red line, labeled as RT1. And RT after the second heating/cooling process shown in blue line, labeled as RT2. 1000 K during the first heating / cooling process shown in black line, labeled as 1000 K1. While 1000 K during the second heating / cooling process shown in red line, labeled as 1000 K2.

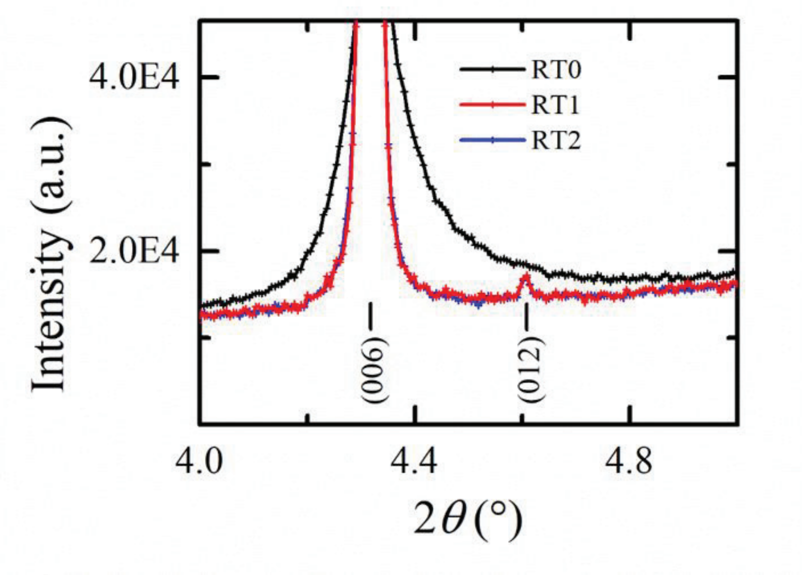

Fig. 4-29. Enlarged SXRD profiles of $Bi_4Ti_3O_{12}$ self-supported films at RT. RT in the as-deposited state shown in black line, labeled as RT0. While RT after the first heating/cooling process shown in red line, labeled as RT1. And RT after the second heating/cooling process shown in blue line, labeled as RT2.

Diffuse scattering also plays an important role in increasing the phase transition temperature of PT self-supported films and BiT self-supported films. As shown in Fig. 4-28 (a), Huang-diffuse scattering of PT self-supported films is clearly observed in the peak tail at RT0, especially for (101) peak. However, the Huang-diffuse scattering vanishes at RT1 and RT2 as shown in red and blue lines. In this case, the Huang-diffuse scattering comes from lattice distortion around the Pb vacancy defect and O vacancy defect due to their partial vaporization during the deposited process. Thus, as shown in Fig. 4-28 (b), the Huang-diffuse scattering cannot be observed at 1000 K. In addition, the Huang-diffuse scattering of BiT self-supported films shown Fig. 4-29 is clearly observed at the (006) peak tail at RT0. Meanwhile, as shown in red and blue lines, the Huang-diffuse scattering of BiT self-supported films also disappears at RT1 and RT2. Since the diffuse scattering suppresses the change of the crystal lattice during the 1st heating process, leading to a higher T_C.

These observations provide a string for further understanding the phase transition behavior of the self-supported films. The upshift of T_C of the self-supported films deposited by AD method is attributed to the Huang-diffuse scattering, spontaneous polarization, and residual stress in the films. During the first heating process, the Huang-diffuse scattering and residual stress are gradually released, hence, the phase transition behavior of the self-supported films is the same of the powders during the subsequent cooling process and heating processes.

4.3 Crystal structure of $PbTiO_3$ self-supported films

As mentioned above, during the first heating process, both PT AD film and PT self-supported films exhibit a weakening of peak intensity, a broadening of peak width and the upward shift of T_C. While during the subsequent cooling and heating processes, these two films also show the same features, i.e., strong peak intensity, narrow peak width and the same T_C value as that of the powder samples. In addition, the peak positions of the (002) diffraction peaks of both the PT AD film and the PT self-supporting films are shifted to the right side during the second heating compared to the first heating process, indicating that the lattice parameter *c* is contracted. Thus, the crystal characteristics of the PT self-supported films and the PT AD film maintain a high degree of consistency, which supports our assumption that we can use the self-supported films to study the structural characteristics of the AD film.

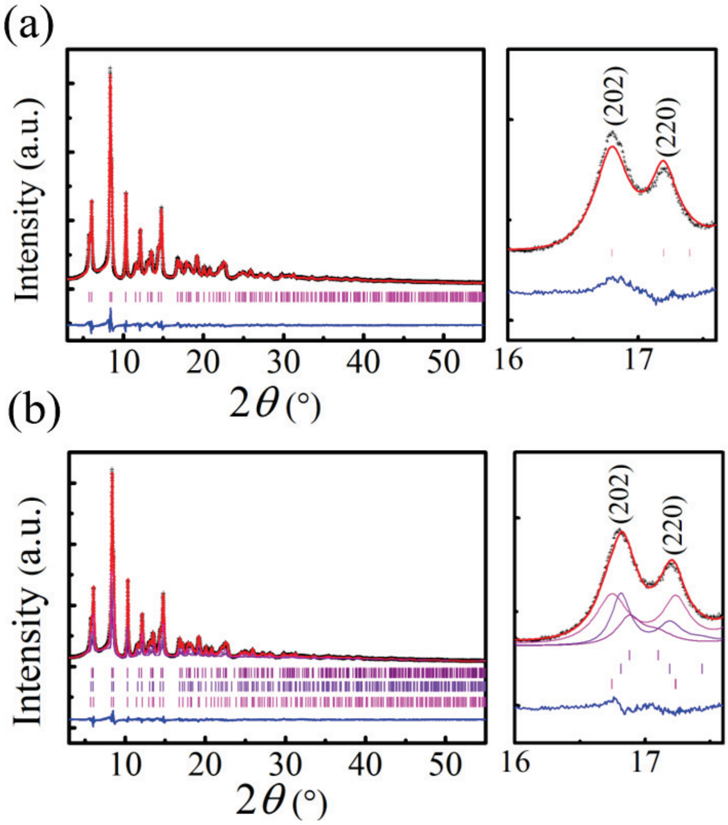

Fig. 4-30. Diffraction profiles of SXRD patterns of $PbTiO_3$ self-supported films analyzed by Rietveld refinement using (a) single phase and (b) three-phases.

Based on aforementioned analysis, the starting powders and the self-supported films were refined by the Rietveld refinement at RT. For PT self-supported films, RT means RT in the as-deposited state, i.e., RT0. We note, as shown in Fig. 4-30 (a), there are some mismatches of the peak intensities between the experiment and the fitting results when we use single-phase to refine PT self-supported films, such as (202) and (220) peaks. The inset of Fig. 4-7(a) shows that the single-phase fitting results of the starting powders are well matched. Due to the crystal size effect, which affects the peak intensity and width distribution, it is necessary to consider that the Rietveld multi-phases refinement method to analyze the self-supported films. Therefore, as shown in Fig. 4-30 (b), PT self-supported films analyzed by three-phases Rietveld refinement exhibit a good fitting results, suggesting that the self-supported films are composed of crystallites of different sizes. The details of fitting results refined by three-phases Rietveld refinement method are listed in Table 4-5. As illustrated in Table 4-5, the phase 1 with a large *c*/*a* (1.061) corresponds to a coarse size, while phase 3 with a small *c*/*a* (1.027) corresponds to a fine size. The average crystallite size of the self-supported films is about 100 nm. The volume ratio of phase1, phase2 and phase 3 are also detailed in Table 4-5.

Table 4-5. Structural parameters of $PbTiO_3$ self-supported films analyzed by three-phases Rietveld refinement method at RT in the as-deposited state (RT0). Space group: *P*4*mm*, $R_{wp} = 3.25\%$, $R_I = 2.81\%$, $R_F = 2.27\%$. The volume ratio of Phase1 : Phase2 : Phase3 = 54.3% : 27.5% :18.2%. The structural parameters of $PbTiO_3$ powders also were listed to compare with the self-supported films.

	Atom	***x***	***y***	***z***	**U (10^{-2}Å^2)**	***c*/*a***
Phase1 *a* = 3.904(2) (Å) *c* = 4.141(3) (Å)	Pb	0	0	0	1.10(5)	1.061
	Ti	0.5	0.5	0.536(8)	0.21(3)	
	O1	0.5	0.5	0.13(1)	4.6(3)	
	O2	0.5	0	0.64(1)	0.85(9)	
Phase2 *a* = 3.909(3) (Å) *c* = 4.088(2) (Å)	Pb	0	0	0	1.10(5)	1.046
	Ti	0.5	0.5	0.541(7)	0.21(3)	
	O1	0.5	0.5	0.11(1)	4.6(3)	
	O2	0.5	0	0.57(1)	0.85(9)	
Phase3 *a* = 3.927(2) (Å) *c* = 4.031(3) (Å)	Pb	0	0	0	1.10(5)	1.027
	Ti	0.5	0.5	0.537(9)	0.21(3)	
	O1	0.5	0.5	0.09(1)	4.6(3)	
	O2	0.5	0	0.54(2)	0.85(9)	
Powder *a* = 3.90000 (1) (Å) *c* = 4.15266 (2) (Å)	Pb	0	0	0	0.756 (4)	1.065
	Ti	0.5	0.5	0.5392 (6)	0.34 (2)	
	O1	0.5	0.5	0.115 (1)	0.7 (1)	
	O2	0.5	0	0.617(1)	0.72 (8)	

4.4 Conclusions

We are comprehensively investigated the mechanism of *c*-oriented PT AD film and BiT AD film to elucidate the mechanism of film growth. Based on the structural characteristics of the AD film and the chemical bonding of the starting powders, we revealed that the *c*-oriented of PT AD film and BiT AD film are due to the layered structure. In the deposited process, as shown in Fig. 4-31, due to the strong 2D covalent bonding of PT increases the binding force along the *ab* plane, the highest probability of recombination occurs when particles recombine and grow along the *ab* plane. We further point out that not only the AD method, but also other methods with deposited temperature below Curie temperature, such as hydrothermal method, result in the formation of *c*-oriented PT film. The phase transition behavior study shows that the T_C of PT self-supporting film is 860 K, which are close to 100 K higher than that of PT starting powders. The upshift of T_C in the self-supported films comes from Huang-diffuse scattering, spontaneous polarization, and residual stress. In addition, our work also reveals that PT AD film is composed of crystallites with different sizes. We believe that these results will be useful for further understanding and design ferroelectric films.

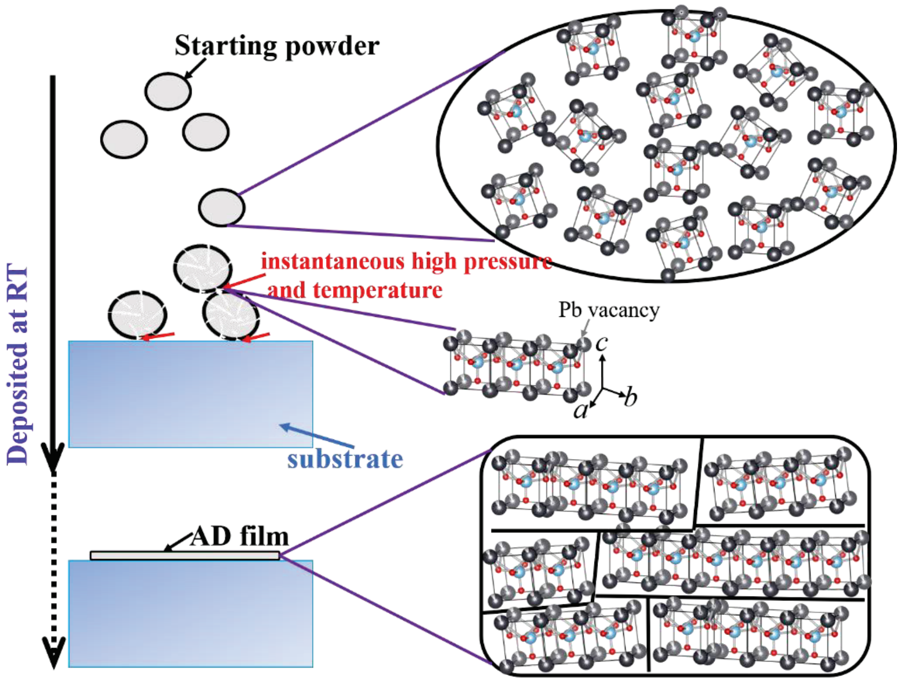

Fig. 4-31. Schematic image of film growth deposited by the AD process.

Chapter 5

Crystal structure and phase transition in $Pb(Zr_{1-x}Ti_x)O_3$

Piezoelectric material lead zirconate titanate $Pb(Zr_{1-x}Ti_x)O_3$ (PZT), which has a perovskite-type structure, is known for its application in electronic devices and microdevices such as transducer and electromechanical, and is one of the most widely used materials in industry.[19-24] Various methods such as conventional solid-state reaction method, sol-gel method and hydrothermal synthesis method have been proposed to synthesize the PZT ceramics.[1,7-10,105-108] Among them, a mechanochemical solid-state reaction using a ball milling is a unique method, which synthesizes PZT fine ceramic powders in air at RT without any post-annealing.[1,2,6] In this study, the validity of PZT powder synthesis from a mixture of PZ ($PbZrO_3$) and PT powders by the mechanochemical solid-state reaction using a ball milling has been investigated by SXRD experiments, revealing the quantitative crystal structure and the phase transition behavior for PZT powder synthesized by ball milling.

5.1 $Pb(Zr_{1-x}Ti_x)O_3$ Synthesis

A mixture of PZ powder and PT powder in a molar ratio of 1 : 1 was ball-milled for 4, 8, 16 and 32h, and named 4h PZ-PT, 8h PZ-PT, 16h PZ-PT and 32h PZ-PT, respectively. Figures 5-1(a), (b) and (c) show SEM-EDX images of the mixture of PZ and PT powders with ball milling times of 0, 4 and 8 h, respectively. As shown in Fig. 5-1(a), since the mixture has not undergone any ball milling, the starting powder is naturally consisting of PT (red) and PZ (green) powders with a molar ratio of 1:1. We note, after 4 h of grinding, most of the red and green were transformed into the yellow area. Figure 5-1(b) also clearly displays some unreacted PZ and PT powders as the minor phase of the 4h PZ-PT sample. Meanwhile, as the ball milling time was further increased to 8 h as shown in Fig. 5-1(c), all PZ and PT powders completely converted to yellow. In addition, we also find that the particle size of the 8h PZ-PT sample is larger than that of the 4h PZ-PT sample. In this case, there are two possibilities for the yellow area, the first one is the new phase PZT we want and the second one is a mixture of very fine PZ and PT particles.

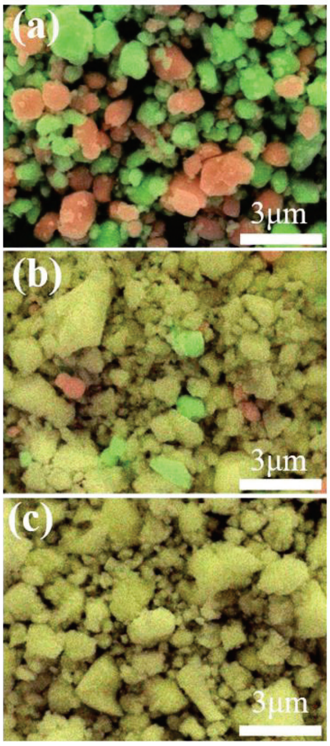

Fig. 5-1. SEM images of mixture of PZ and PT powders. Ball milling for (a) 0 h (starting powders), (b) 4 h and (c) 8 h. The red and green particles colored by SEM-EDX indicate PT and PZ powders, respectively.

SXRD experiments were conducted to examine the validity of PZT synthesis. As can be observed in Fig. 5-2, the SXRD profiles of the ball-milled PZ–PT samples are at RT in the as-synthesized state without any post-annealing. Here, we should explain that the diffraction intensity of the reference material PZT ceramic was divided by 5 in order to obtain a good visualizing contrast. Firstly, we observed that the diffraction patterns, such as peak positions and peak intensities, of all milled PZ-PT samples match very well with those of the reference material PZT ceramic sample. This observation implies that all milled PZ-PT samples have the similar diffraction patterns to the PZT sample. Therefore, we concluded that PZT synthesized by ball milling a mixture of PZ and PT powders can be synthesized. To illustrate the effect of ball milling time, the intensity of the (110) peak versus milling time is plotted in the inset. We note, the intensities of the (110) peaks firstly increase at the milling time of 0 to 8 h and then decrease at the milling time of 8 to 32 h, while the highest intensity of the (110) peak occurs at 8 h of ball milling. This observation confirms that a new phase of PZT was generated during the ball milling process. That is, the new phase of the PZT powder is generated and grows with the increase of the grinding time from 0 to 8 h, leading to an increase in the intensity of the (110) peak with the increase of the grinding time. Meanwhile, after

8 h of ball milling, all PZ and PT powders were completely converted to PZT phase, leading to the particle size of PZT powder decreases with the increase of milled time. The change in intensity of the (110) peak provides a reasonable evidence that the PZT sample has been successfully synthesized by the mechanochemical solid-state reaction using a ball milling, which confirms that the yellow part in the SEM-EDX is consisting of PZT phase.

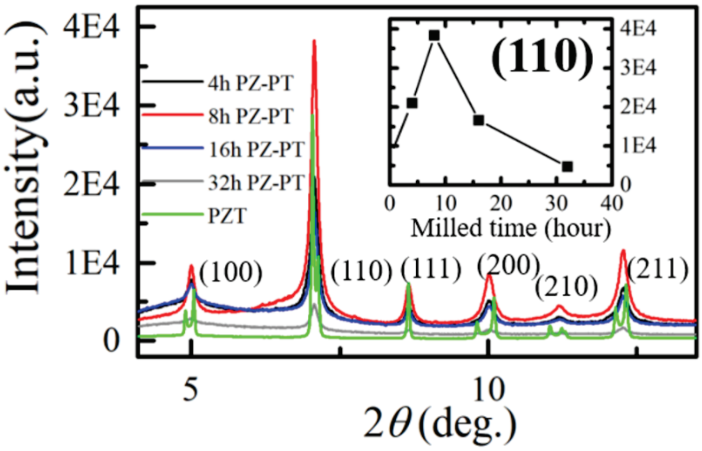

Fig. 5-2. SXRD patterns of milled PZ-PT samples and reference PZT sample at RT. Black, red, blue, gray and green lines indicate the samples of 4h PZ-PT, 8h PZ-PT, 16h PZ-PT, 32h PZ-PT, and reference material PZT, respectively. The insert shows the intensities of (110) peaks of these milled PZ-PT samples.

To further validate the synthesis of PZT ceramic powders, the structural characteristics of ball-milled PZ-PT samples were investigated. Figure 5-3(a) shows the enlarged SXRD profiles of the 4h PZ-PT, reference material PZT, starting powders of PT and PZ samples at RT. Here, black, green, orange and cyan lines denote the samples of 4h PZ-PT, reference material PZT, PT and PZ, respectively. Clearly, the enlarged (110) peak of the 4h PZ-PT sample exhibits two weak impurity peaks, indicated by the arrows from unreacted PZ and PT, which also coincides with the observation of the SEM-EDX shown in Fig. 5-1(b). Figure 5-3(b) shows the enlarged (110) peaks of the 8h PZ-PT, 16h PZ-PT, 32h PZ-PT and reference material PZT samples in red, blue, gray and green, respectively. Conversely, the 8h PZ-PT, 16h PZ-PT and 32h PZ-PT samples exhibit pure PZT diffraction patterns, indicating that all PZ and PT reacted into PZT phase. As the samples were ball-milled for a long time, the particle sizes or crystallite sizes became smaller and the peak profile of the SXRD broadened. Therefore, it is natural to consider that the pure PZT phase has been successfully synthesized by the mechanochemical solid-state reaction using dry ball milling in a short time.

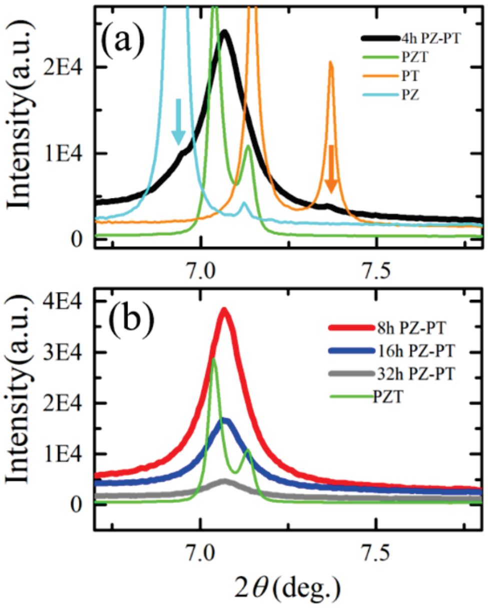

Fig. 5-3. (a) enlarged (110) peaks of PZ, PT, PZT and 4h PZ-PT samples at RT. (b) enlarged (110) peaks of 8h PZ-PT, 16h PZ-PT, 32 PZ-PT and PZT samples at RT.

Next, to further examine the structural characteristics, the SXRD patterns of ball-milled PZ-PT, reference material PZT, starting powders of PZ and PT samples at 1000 K are displayed in Fig. 5-4. The PZT, PZ and PT samples are a cubic structure at 1000 K. Therefore, as shown in Fig. 5-4, the peak profile observed at 1000 K is a single peak with symmetrical profile. As shown in Fig. 5-4(a), all observed peak positions in the ball-milled PZ-PT samples at 1000 K are in good agreement with those of the reference material PZT sample, indicating that the ball-milled PZ-PT samples are PZT phase. The highest intensity of the (110) peak appears at 8 h of ball milling, which was observed in the insert of Fig. 5-4 (a). This observation also coincides with the highest intensity that occurs at 8 h of ball milling at RT. Furthermore, the (110) peak of the 4h PZ-PT sample also exhibits weak diffraction peaks of unreacted PZ and PT, as shown in Figure 5-4(b), while the 8h PZ-PT, 16h PZ-PT and 32h PZ-PT samples are pure PZT structural characteristics, as shown in Figure 5-4(c). These results also validate that the analysis in Fig. 5-2 and Fig. 5-1 is correct. That is, we can conclude that PZT could be synthesized in a short time. Therefore, the present experiments show that PZT can be synthesized by ball milling a mixture of PZ and PT powders in a sufficiently short time compared to that ball milling a mixture of PbO, TiO_2 and ZrO_2 powders.[109]

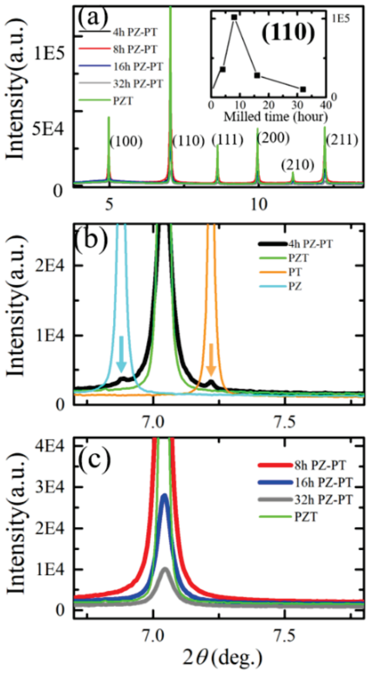

Fig. 5-4. SXRD profiles of the ball-milled PZ–PT and sintered PZT samples at 1000 K in the cubic phase. (a) SXRD profiles of the ball-milled 4h, 8h, 16h, and 32h PZ–PT samples along with the sintered PZT sample as a reference. (b) Comparison of the (110) peak profile of the 4h PZ–PT sample and those of the PZT, PT, and PZ samples. (c) (110) peak profiles of the 8h, 16h, and 32h PZ–PT samples and PZT sample.

5.2 Crystal structure of Pb(Zr$_{1-x}$Ti$_x$)O$_3$

Next task is to investigate the crystal structure of the ball-milled PZ-PT samples. In this work, due to PZT phase was synthesized within 8 h, the samples of 4h PZ-PT and 8h PZ-PT were chosen to analyze the crystal structure. PZT should have a pure *P*4*mm* symmetry or *P*4*mm* + *R*3*m* symmetry at RT when the molar ratio of Ti over Zr close to 1.[142,143] However, as shown in Fig. 5-2, the ball-milled PZ-PT samples look like a pseudocubic structure at RT. Therefore, to avoid this confused phenomenon, first, the crystal structure was analyzed by the Rietveld method at 1000 K above T_C,.

5.2.1 Crystal structure of 8h PZ-PT powder

As analyzed above, the 8h PZ-PT sample is pure PZT phase. Thus, as shown in Fig. 5-5, the crystal structure of the 8h PZ–PT sample has been successfully analyzed using the Rietveld method at 1000 K. Due to the molar ratio of PZ and PT is 1 : 1, it is natural to assume that the composition of the 8h PZ-PT sample is $Pb(Zr_{0.5}Ti_{0.5})O_3$.

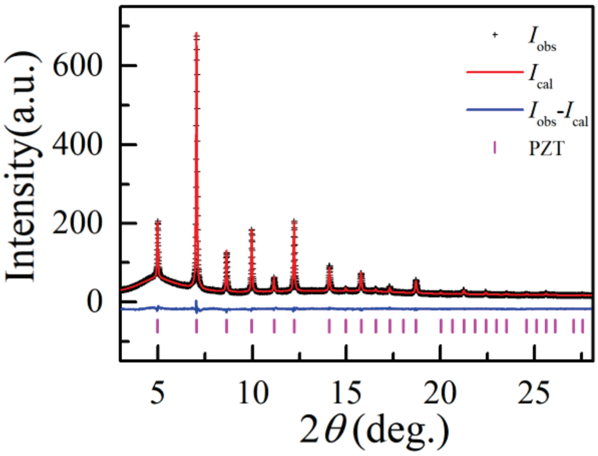

Figure 5-5. Rietveld fitting results of the 8h PZ-PT sample at 1000 K in a cubic system. The values of R_{WP}, R_I and R_F are 2.97 %, 5.95 % and 6.53 %, respectively.

To determine the accurate composition of the 8h PZ-PT sample, the occupancy of Ti and Zr was analyzed by Rietveld refinement. First, the occupancy of Pb and O was fixed at 1. Then, as shown in Fig. 5-6, by varying the value of x from 0 to 1, the lowest R_{WP} value of $Pb(Zr_{1-x}Ti_x)O_3$ is obtained when x is 0.515 (1), indicating that the composition of $Pb(Zr_{1-x}Ti_x)O_3$ is $Pb(Zr_{0.485(1)}Ti_{0.515(1)})O_3$. However, since the molar ratio of PZ and PT is 1 : 1, the content of Ti cannot exceed 0.5 if we assume that the content of Pb is 1. Thus, we speculate that a small amount of unreacted PZ powder may exist in the amorphous form and show no diffraction peaks, resulting in no contribution to the synthesis of PZT.

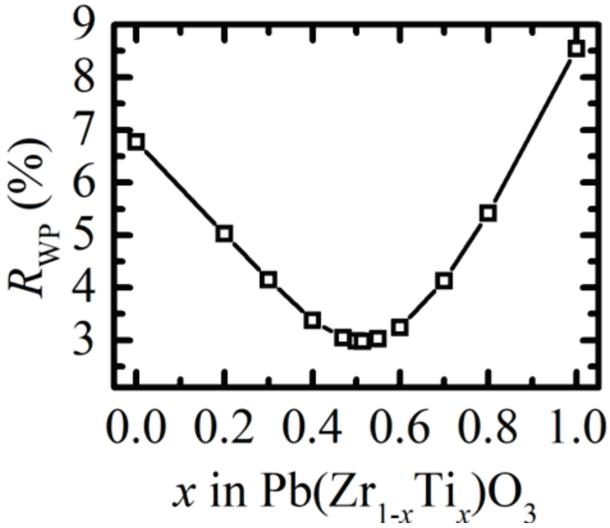

Fig. 5-6. R_{WP} values as a function of Ti content in the 8h PZ-PT sample at 1000 K.

Since the 8h PZ-PT powders with a Ti-rich composition, the crystal systems of the 8h PZ-PT can be assumed as a cubic ($Pm\bar{3}m$) at 1000 K and a tetragonal ($P4mm$) at RT. Based on the Rietveld analysis, as shown in Fig. 5-7(a) and (b), the crystal structure of the 8h PZ-PT sample has been successfully analyzed at RT in the as-synthesized state (RT0) and after the first heating/cooling process (RT1). While the lattice parameter a of 8h PZ-PT sample is 4.0801(4) Å at 1000 K, which is consistent with those of PZT bulk ceramics published in other papers, the lattice parameters a and c of 8h PZ-PT sample are 4.052(2) Å and 4.096(5) Å at RT0, and 4.056(2) Å and 4.072(2) Å at RT1, implying that the spontaneous strain at RT0 and RT1 are significantly small compared to those of PZT bulk ceramics. Meanwhile, we observed that the values of the isothermal vibration factor U_{iso} of Pb and O are quite larger at RT0 compared to those at RT1 and the PZT bulk ceramics. The structure parameters of the 8h PZ-PT sample at RT0, 1000 K and RT1 are detailed in Table 5-1.

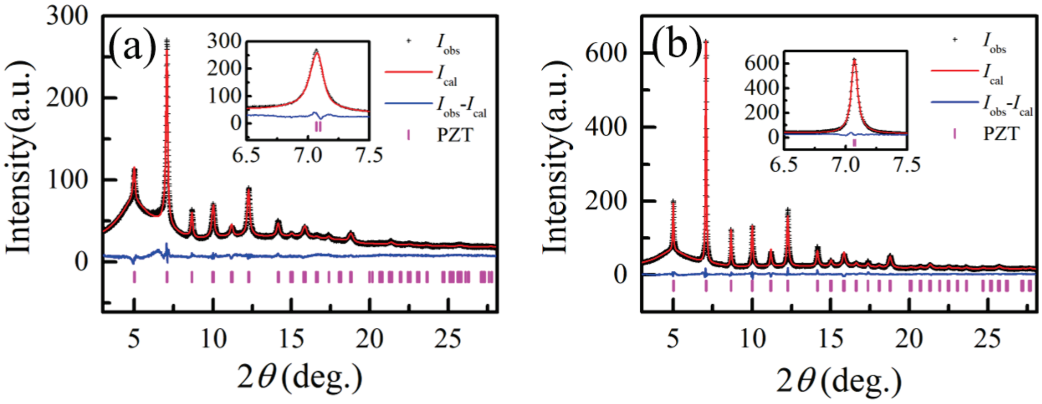

Fig. 5-7. Rietveld fitting results of the 8h PZ-PT sample at (a) RT0 and (b) RT1. AT RT0, the values of R_{WP}, R_{I} and R_{F} are 3.44 %, 6.63 % and 5.84 %, respectively. At RT1, the values of R_{WP}, R_{I} and R_{F} are 3.86 %, 3.27 % and 2.63 %, respectively.

Table 5-1. Structural parameters of the 8h PZ-PT sample at RT0, 1000 K and RT1.

	Atom	x	y	z	U_{iso} (10^{-2}Å^2)
RT0	Pb	0	0	0	3.41(1)
a = 4.052(2) Å	Ti/Zr	0.5	0.5	0.529(3)	0.46(2)
c = 4.096(5) Å	O1	0.5	0.5	0.086(4)	8.0(2)
c / a = 1.011	O2	0.5	0	0.588(6)	7.1(1)
1000 K	Pb	0	0	0	4.86(3)
a = 4.0801(4) Å	Ti/Zr	0.5	0.5	0.5	1.6(4)
	O	0.5	0.5	0	4.8(4)
RT1	Pb	0	0	0	1.57(6)
a = 4.056(2) Å	Ti/Zr	0.5	0.5	0.531(1)	0.91(5)
c = 4.072(2) Å	O1	0.5	0.5	0.090(2)	2.7(2)
c / a = 1.004	O2	0.5	0	0.591(6)	2.6(3)

5.2.2 Crystal structure of 4h PZ-PT powder

As mentioned above, the 4h PZ-PT sample has some unreacted PZ and PT as impurity phases at 1000 K. Hence, in this Rietveld refinement, multi-phase model, i.e., PZT, PZ and PT phases, all with the space group of $Pm\bar{3}m$, was considered to analyze the crystal structure. The Rietveld profile fitting result is illustrated in Fig. 5-8. Red, cyan and green denote PZT, PZ and PT phases, respectively. The enlarged Rietveld fitting profile of the (110) peak is plotted in the insert, exhibiting a good fitting result, demonstrating that the 4h PZ-PT sample has been successfully analyzed at 1000 K using a multi-phase model. The lattice parameters *a* of PZT, PZ and PT phases with cubic structure are 4.0801(4) Å, 4.1790(4) Å and 3.9808(1) Å, respectively, in agreement with other published articles. In addition, we observe that the volume ratio of PZT phase is greater than 97 % in the 4h PZ-PT sample, which implies that most of PZ and PT powders were transformed into PZT phase. The composition of PZT phase in the 4h PZ-PT sample has also been analyzed by the Rietveld method. As shown in Fig. 5-9, with the occupancy of Pb and O fixed at 1, by changing the value of x from 0 to 1, the lowest R_{WP} value of $\mathrm{Pb(Zr_{1\text{-}}{}_{x}Ti_{x})O_3}$ is obtained when x is 0.509 (1), indicating that the composition of $\mathrm{Pb(Zr_{1\text{-}}{}_{x}Ti_{x})O_3}$ is $\mathrm{Pb(Zr_{0.491(1)}Ti_{0.509(1)})O_3}$. The Zr content in the 4h PZ-PT sample is higher than that in the 8h PZ-PT sample, due to the larger ionic radius of the Zr ion, resulting in a larger lattice parameter *a* (4.08244(1) Å) for the 4h PZ-PT sample than the lattice parameter *a* (4.08025(1) Å) for the 8h PZ-PT sample. In addition, the ratios of Zr/Ti in both the 4h PZ-PT sample and the 8h PZ-PT sample are very close to 1 : 1, which is the nominal molar ratio of PZ and PT, indicating no obvious deviation in the Zr/Ti ratio during the ball milling process. This implies that the PZT with any Zr/Ti composition ratio we want can be synthesized by changing the molar ratio of PZ and PT powders.

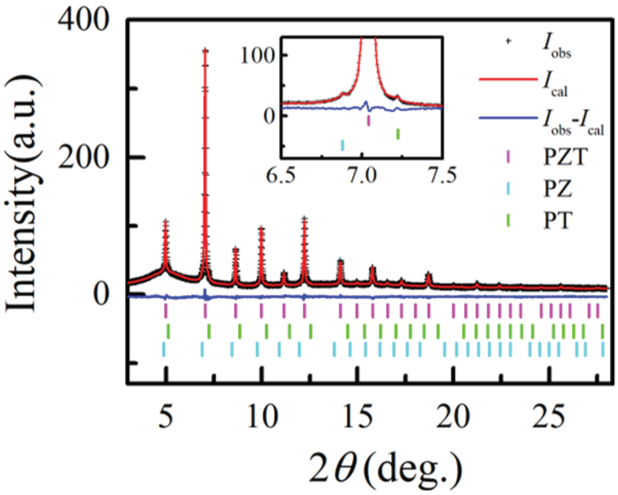

Fig. 5-8. Rietveld fitting results of the 4h PZ-PT sample at 1000 K. The values of R_{WP}, R_{I} and R_{F} are 3.623 %, 5.74 % and 8.39 %, respectively. Volume ratio of PZT : PZ : PT = 97.3(1)% : 1.5(1)% : 1.2(1)%.

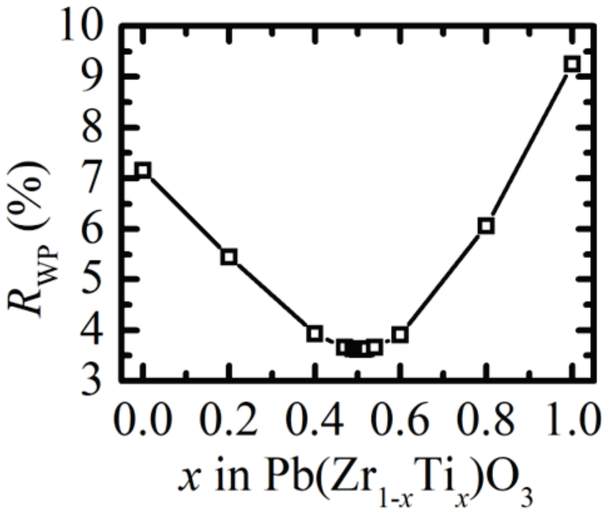

Fig. 5-9. R_{WP} values as a function of Ti content in the 4h PZ-PT sample at 1000 K.

Since the 4h PZ-PT sample with a Ti-rich composition, the crystal systems of the 4h PZ-PT can be assumed as a cubic at 1000 K and a tetragonal at RT. According to the Rietveld analysis, the 4h PZ-PT sample has been successfully analyzed by multi-phase model, i.e., PZT, PZ and PT phases, at RT. The space groups of PZT, PZ and PT are *P*4*mm*, *Pbam* and *P*4*mm*, respectively. Meanwhile, the lattice parameters *a* and *c* of PZT are 4.047(2) Å and 4.080(2) Å, indicating that the spontaneous strain of 4h PZ-PT is also significantly small compared to those of bulk PZT ceramics. While the lattice parameters *a* and *c* of PT are 3.903(1) Å and 4.162(3) Å. The lattice parameters *a*, *b* and *c* of PZ are 5.8781(3) Å, 11.7774(7) Å and 8.2225(5) Å, respectively. The details of the structure parameters are shown in Table 5-2.

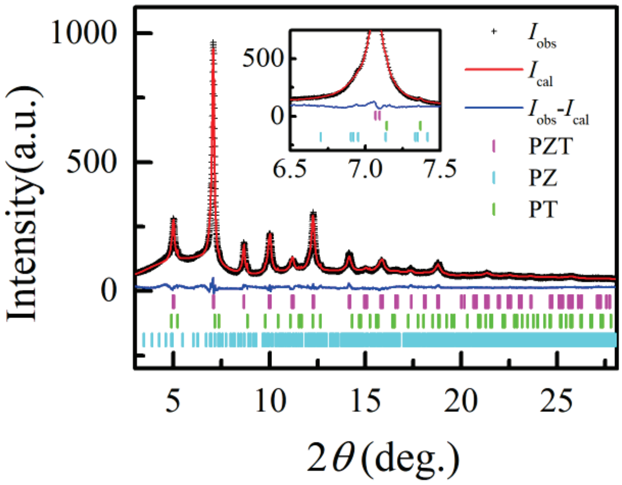

Fig. 5-10. Rietveld fitting results of the 4h PZ-PT sample at RT. The values of R_{WP}, R_I and R_F are 3.841 %, 4.922 % and 4.28 %, respectively.

Table 5-2. Structural parameters of the PZT phase in 4h PZ-PT sample at RT0 and 1000 K.

	Atom	x	y	z	U_{iso} (10^{-2}Å^2)
RT0	Pb	0	0	0	3.15(3)
a = 4.047(2) Å	Ti/Zr	0.5	0.5	0.529(2)	0.25(1)
c = 4.080(2) Å	O1	0.5	0.5	0.087(5)	6.1(1)
c / a = 1.008	O2	0.5	0	0.590(6)	4.7(3)
1000 K a = 4.0824(5) Å	Pb	0	0	0	4.75(6)
	Ti/Zr	0.5	0.5	0.5	1.3(3)
	O	0.5	0.5	0	4.4(5)

5.3 Phase transition of 8h PZ-PT powder

5.3.1 Upshift of phase transition temperature

As described in Fig. 5-2, the diffraction pattern of the 8h PZ-PT sample looks like that of a cubic or pseudocubic symmetry at RT. Temperature dependence SXRD experiments were performed to investigate this confused phenomenon. Diffraction data were collected on the detector at 5 K intervals from RT to 1000K to obtain accurate phase transition behavior. The 2D image around (110) peak of the 8h PZ-PT sample is displayed in Fig. 5-11. As a contrast experiment, changes in crystal structure of the reference material PZT sample were also plotted in Fig. 5-11. Obviously, as shown in Fig. 5-11(e) and (f), from high temperature to low temperature, the single (110) peak splits into two peaks, the (101) peak and the (110) peak, at 640 K, indicating that the T_{C} of the reference material PZT sample is 640 K for both heating and cooling processes. We observe, although there is no clear peak splitting of the (110) peak from high temperature to low temperature during heating and cooling processes, the (110) peak position of the 8h PZ-PT sample shifts more rapidly to the left when temperature is above a certain temperature (T_{C}). Therefore, we consider that the pseudocubic structure of the 8h PZ-PT sample at RT maybe come from the small particle size and the small value of tetragonality (c/a), which can cause the (101) peak and the (110) peak to overlap at low temperature, resulting in the (110) peak looking like a single peak at RT.

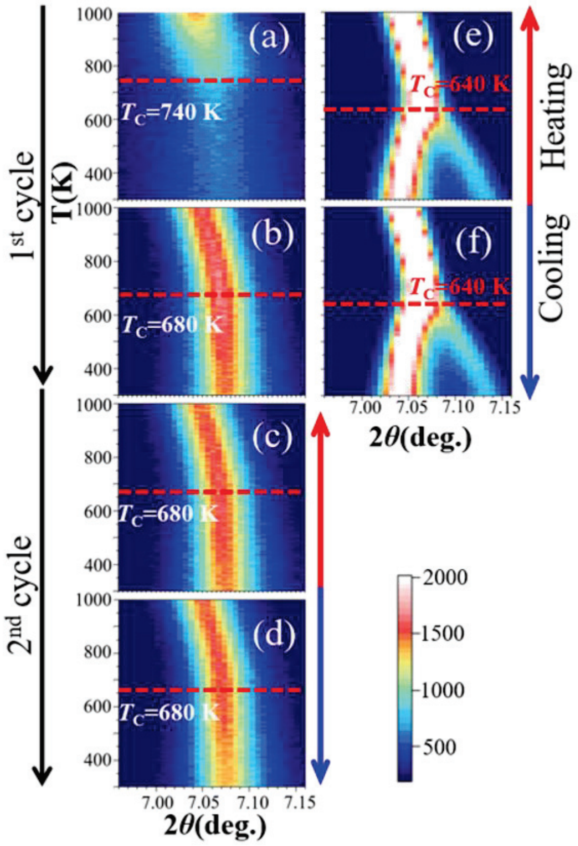

Fig. 5-11. Temperature dependence SXRD patterns of the 8h PZ-PT sample and the reference material PZT sample. (a) the 1st heating, (b) 1st cooling, (c) 2nd heating and (d) 2nd cooling processes for the 8h PZ-PT sample. (e) the heating and (f) cooling processes for the reference material PZT sample.

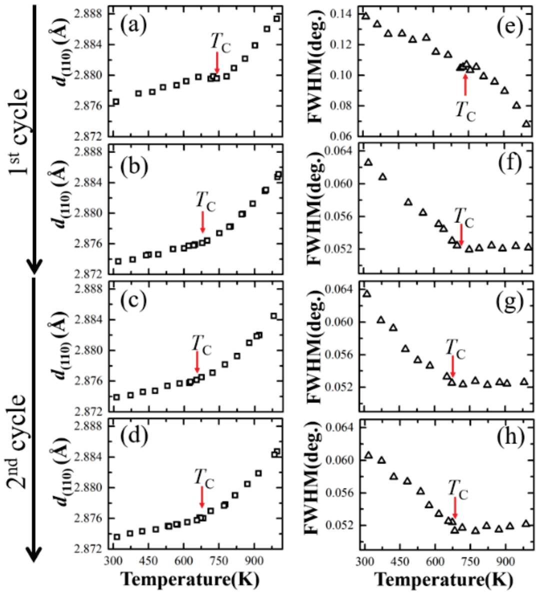

Fig. 5-12. Changes in the *d*-value and full width at half maximum (FWHM) of (110) peak of the 8h

PZ–PT sample as a function of the temperature during the (a) and (e) first heating, (b) and (f) first cooling, (c) and (g) second heating, and (d) and (h) second cooling processes, respectively. These data are derived by analyzing the (110) pattern of the 8h PZ–PT shown in Fig. 5-11. The T_C determined in each process is indicated by a red arrow in each figure.

Compared to the cooling process, we note, the peak intensity of the (110) peak is weakened during the first heating process, accompanied by broaden peak width. In addition, we also find that the diffraction intensity of the (110) peak increases rapidly above T_C during the first heating process. Since there is no peak splitting in the temperature range from RT to 1000 K, the *d*-value of the (110) peak and the peak width (full width at half maximum, FWHM) of the (110) peak are plotted in Fig. 5-12 in order to accurately determine the T_C of the 8h PZ-PT sample. First, as shown in Fig. 5-12(f), (g) and (h), the peak width of the (110) peak is a constant above T_C in the paraelectric phase, while the peak width gradually broadens with decreasing temperature below T_C in the ferroelectric phase. Therefore, it can be clearly seen that all T_C for the first cooling, second heating and second cooling processes are 680 K, as shown in Fig. 5-12(f), (g) and (h), respectively. Meanwhile, as shown in Fig. 5-12(b), (c) and (d), the changes in the *d*-value show a bend at T_C. Thus, the change in *d*-value also confirms that the T_C of the 8h PZ-PT sample is 680 K during the first cooling, second heating and second cooling processes. Then, based on the same analysis method, we carefully investigate the T_C during the first heating process. As shown in Fig. 5-12(e), we note that the peak width of the (110) peak is not a constant at temperature above T_C, but decreases more rapidly in the first heating. As described in Fig. 5-11(a), the peak intensity of the (110) peak increases more rapidly at temperature above T_C in the first heating. Thus, we consider that the increase in grain size of the 8h PZ-PT sample at temperature above T_C leads to an increase in peak intensity and a decrease in peak width. Therefore, the T_C of the 8h PZ-PT sample can be confirmed at 740 K during the first heating process, which also can be validated by the change of the *d*-value, as shown in Fig. 5-12(a). We note, the T_C of the 8h PZ-PT sample is upshifted compared to that of the reference material PZT sample, especially in the first heating process.

5.3.2 Mechanism of phase transition temperature upshift

According to the above analysis, the first heated T_C of the 8h PZ-PT sample is 60 K higher than the first cooled T_C and 100 K higher than that of the reference material PZT ceramic. To explore the origin of T_C upshift in the 8h PZ-PT sample, our studies are shown the following. According to the Landau theory relationship $T_C = \alpha P_S^2$,[49] T_C is strongly coupled with tetragonality (c/a), indicating that high T_C means large c/a. However, as aforementioned analysis, the tetragonality of 8h PZ-PT sample is significantly small ($c / a = 1.011$ at RT0 and 1.004 at RT1) compared to other published articles.[98] The temperature dependences of the lattice parameters of the 8h PZ-PT sample and the reference material PZT sample are shown in Fig. 5-13. As can be observed in Fig. 5-13, tetragonality of 8h PZ-PT is significantly small compared to that of reference material PZT shown in Fig. 5-13(a).

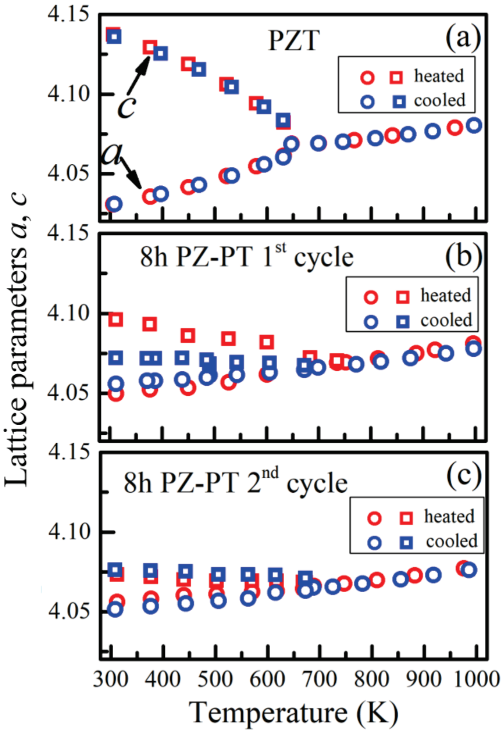

Fig. 5-13. Lattice parameters of *a* and *c* as a function of temperature for the sintered PZT and 8h PZ-PT samples; (a) sintered PZT during the heating/cooling process, 8h PZ-PT during (b) the first heating/cooling process and (c) second heating/cooling process. Red exhibits the heating process while blue indicates the cooling process; the circle represents lattice parameter *a* while the rectangle represents lattice parameter *c*.

Therein, to explore the origin of the T_C upshift, we first consider the contribution of residual stresses in the 8h PZ-PT sample to the T_C enhancement since the synthesis method is a mechanochemical solid-state reaction using dry ball milling. The residual stress in the 8h PZ-PT sample at RT0, RT1 and RT after the second heating (RT2) were analyzed by the Williamson-Hall method. In the Williamson-Hall method, the slope and intercept of the straight line indicate the residual strain and grain size, respectively. As shown in Fig. 5-14(a), we note, the slope ratios of the black, red and blue lines are close to 1, indicating that the strain ratios at RT0, RT1 and RT2 are close to 1. Therefore, since the residual stress at RT1 and RT2 are zero, there is no stress contribution at RT0. In addition, according to the Williamson-Hall method, the grain sizes of the 8h PZ-PT sample at RT0, RT1 and RT2 are 0.2, 1.6 and 1.7 μm, respectively, indicating that the grain size of the 8h PZ-PT sample increases rapidly during the first heating process.

The enlarged SXRD profiles of the (101) and the (110) peaks of the 8h PZ-PT sample at RT0, RT1 and RT2 are plotted in Fig. 5-14(b). As a comparison experiment, Fig. 5-14(b) also shows the enlarged plots of the (101) and (110) peaks of the reference material PZT sample at RT, indicated by the green line. Diffuse scattering of the 8h PZ-PT sample at the tail of the (101) and the (110) peaks can be clearly observed at RT0, RT1 and RT2, especially at RT0. Compared to the low and constant background levels of the reference material PZT sample, the background level of the 8h PZ–PT sample is increased by the diffuse scattering, especially at RT0, which is significantly higher. The degree of diffuse scattering in the 8h PZ-PT sample was partially improved at RT1 and RT2, resulting in lower background levels at RT1 and RT2 than at RT0, but higher than at the PZT sample. In this scenario, we consider that Huang-diffuse scattering comes from lattice distortion around lattice defects produced by the ball milling. The crystallinity of the 8h PZ-PT sample is incomplete due to deformation, fracture and recombination of the particles formed in the ball milling process. Therefore, in the first heating, the incompletely crystallized 8h PZ-PT sample requires more thermal energy to increase the crystallinity, which leads to an upward shift of T_C. After increasing the temperature to 1000 K, the lattice defects were reduced and the crystallite size increased from submicron (RT0) to micron, indicating improved crystallinity. Thus, the first cooled T_C of the 8h PZ-PT sample decreases compared to the first heated T_C. Here, what should be emphasized is the highest heated temperature is only 1000 K, which is far below the sintering temperature (usually above1000 °C), thus, the crystallinity of the 8h PZ-PT sample after heating is partially improved compared to the as-synthesized 8h PZ-PT sample, but not perfectly. As evidence to explain the partial improvement of the crystallinity, the (101) and the (110) peaks also overlap at RT1 and RT2, indicating that the tetragonality (c/a) remain a small value at RT1 and RT2. Thus, the small spontaneous strain of the 8h PZ-PT sample at RT1 and RT2 can be compared with the spontaneous strain at RT0, indicating that the crystallinity of the 8h PZ-PT sample is partially, but not completely, improved.

To improve the crystallinity, the 32h PZ-PT sample was sintered at 1090 °C for 4 h and was named as 32h PZ-PT ceramic. As can be observed in Fig. 5-15, both the reference material PZT and the 32h PZ-PT ceramic clearly exhibit a tetragonal structure, while the 32h PZ-PT sample shows a pseudocubic symmetry. Meanwhile, the lattice parameters a and c of the 32h PZ-PT ceramic are 4.0283(7) Å and 4.14181(7) Å at RT (c/a = 1.028), which coincides with those of the reference material PZT (a = 4.02793(5) Å, c = 4.14448(9) Å and c/a = 1.029) and other published papers,[98] indicating that the spontaneous strain of the 32h PZ-PT ceramic is significantly improved compared to that of the 32h PZ-PT, and implying that the crystallinity of the 32h PZ-PT ceramic is complete. Therefore, the spontaneous strain is strongly coupled to the crystallinity, with small spontaneous strain coming from incomplete crystallinity and large spontaneous strain coming from complete crystallinity.

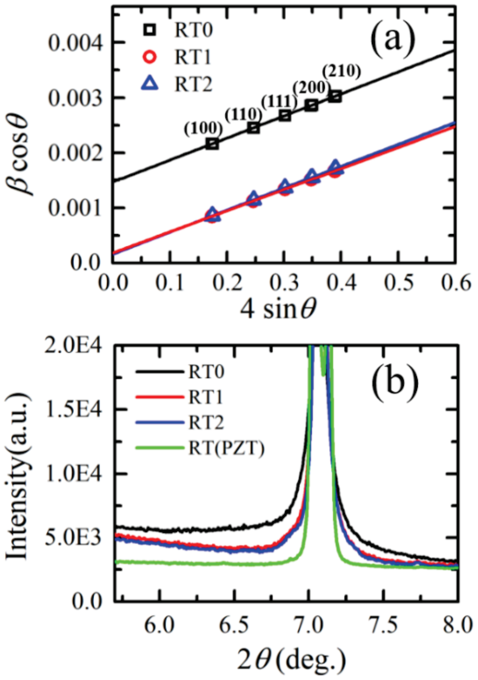

Fig. 5-14. Evaluation of the internal strain and lattice distortion of the PZT synthesized in the 8h PZT–PT sample. (a) Williamson–Hall plot for evaluating internal residual strain and crystallite size. The slope of the graph corresponds to the degree of internal strain, whereas the crystallite size can be estimated from the intercept on the vertical axis. (b) Diffuse scattering observed around the (110) peak at RT, which resembles the Huang scattering around the Bragg peaks caused by the lattice distortion around lattice defects.

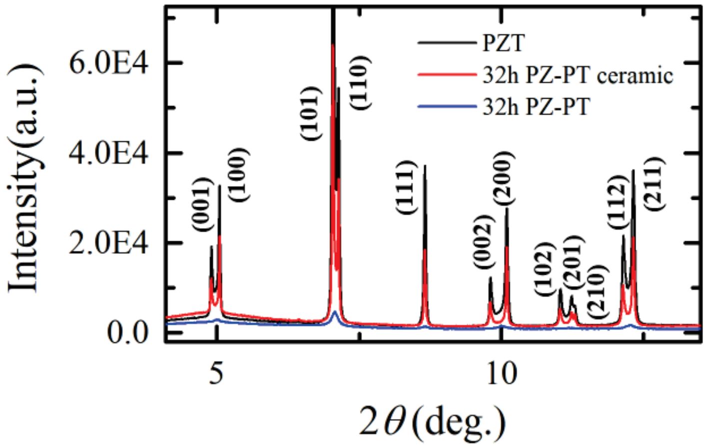

Fig. 5-15. SXRD patterns of reference material PZT, 32h PZ-PT and 32h PZ-PT ceramic samples at RT. The labeled 32h PZ-PT ceramic indicates that the 32h PZ-PT sample was sintered at 1090 ℃ for 4 h. Black, red and blue lines indicate the samples of reference material PZT, 32h PZ-PT ceramic and 32h PZ-PT, respectively.

Finally, to clarify the original reason , the schematic image was shown in Fig. 5-16. As shown in Fig. 5-16(a), since the instantaneous high pressure generated at the collision point on the particle surface exceeds the hardness of the powders, the starting materials of PZ and PT powders were deformation and fracture into small pieces by ball milling. Then, as shown in the enlarged image of the collision point of the small pieces, the instantaneous high-temperature induced by the instantaneous high pressure provides the activation energy for synthesizing the PZT phase. The crystallinity of the synthesized PZT phase is incomplete because the origin of activation energy is mechanical rather than continuous thermal energy. Meanwhile, the lattice crystal of the as-synthesized PZT phase has some lattice defects, such as vacancy defect of Pb and O atoms. Therefore, as shown in Fig. 5-16(b), more thermal energy is required to improve the crystallinity of the as-synthesized PZT phase in the heating process, leading to a higher T_{C}. Since the highest heated temperature 1000 K is far below sintering temperature, which is above 1000 ℃, the crystallinity of the as-synthesized PZT phase is partially improved, resulting in the cooled T_{C} of as-synthesized PZT sample is lower than the heated T_{C} but higher than that of the reference material PZT sample.

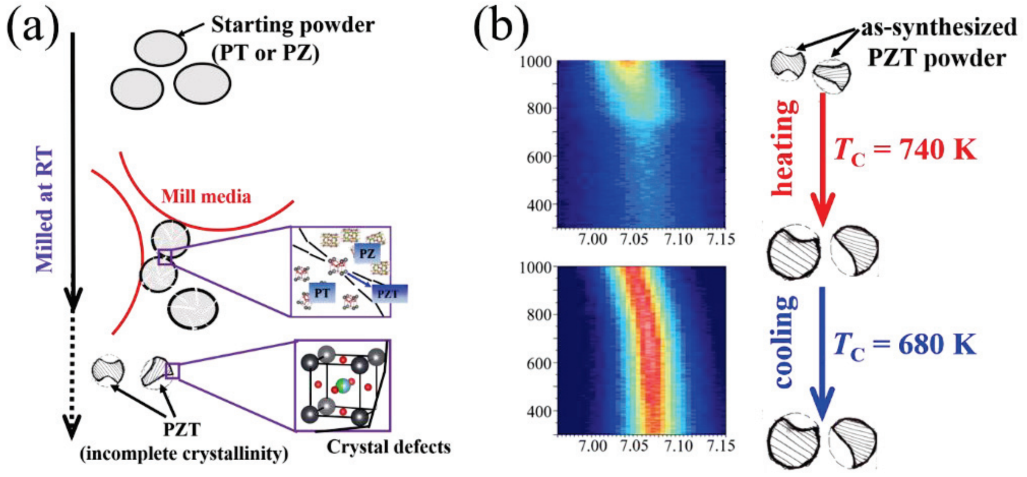

Fig. 5-16. Schematic images of (a) the synthesized process and (b) the origin of the T_{C} enhancement.

5.4 Conclusions

Fine ceramic powder $Pb(Zr_{1-x}Ti_x)O_3$ synthesized by mechanochemical solid-state reaction has been studied by high-energy synchrotron radiation X-ray powder diffraction. SXRD experiments quantitatively confirmed that PZT powder can be synthesized at RT by ball milling a mixture of PZ and PT powders in a considerably short time. In the 8h sample, only single phase of PZT with a composition of $Pb(Zr_{0.485(1)}Ti_{0.515(1)})O_3$ can be detected. The spontaneous lattice strain of PZT synthesized by ball milling at RT is significantly smaller than that of the PZT synthesized by sintering with the same Zr/Ti composition ratio, which resembles a cubic structure even at RT. However, the phase transition temperature is approximately 100 K higher in the first heating process from the as-synthesized state. We consider that the common features of ferroelectric materials fabricated using mechanical energy are mainly low ferroelectricity, but high T_C. The poor crystallinity by the reduction of crystallite size and the increase of lattice distortion is strongly relatively with the upshift of T_C. The physical mechanism as to poor crystallinity increases the T_C needs to be further studied in the future.

Acknowledgement

Time is flying. Although my first day at Hiroshima University is still fresh in my mind, I am now about to complete three years of doctoral studies. First, I am very grateful to my supervisor, Prof. Yoshihiro Kuroiwa, for providing me with an important opportunity to study in a friendly environment and for teaching me how to think from a physical viewpoint. Meanwhile, I would like to give the same thanks to Prof. Chikako Moriyoshi. During the three years, Moriyoshi sensei not only offered the expert advice on my studies, but also helped me to adopt to daily life in Japan. Also, I would like to thank Assistant Prof. Sangwook Kim for his meaningful suggestions in preparing the paper and kind assistance in submitting it. In addition, I also want to thank the co-authors in AIST, including Dr. Muneysu Suzuki, Dr. Kentaro Shinoda, Dr. Rintaro Aoyagi and Dr. Jun Akedo.

I also like to appreciate all members in our lab. I would like to thank Dr. Qing Zhao for his help in learning the skills of the analysis program and in daily life. I also want to thank Dr. Yuki Nakahira for her kindness help with my studies. I also want to appreciate Dr. Tomohiro Abe, who provided much useful help in researching the analysis skills of AD film. Then, I also would like to thank the following members of our lab: S. Tsugita, S. Noda, K. Hagura, Mao Hattori, Misato Muta, Yusuke Yatabe, Reiji Yamauchi, Hikaru Kaneshima, Haduki Yoshida, Takayasu Shigemasu, Takahiro Kokii. As an international student, I would like to thank them very much again for helping me to adopt to life in Japan and spend three happy years.

The experience in SPring-8 is impressive. Naturally, I would like to acknowledge Dr. S. Kawaguchi, a beamline scientist at SPring-8, for supporting my experiments on the beamline station of BL02B2.

I would also want to thank the staffs in the physical science office and the student support office for their help in my university life.

Finally, I would like to thank my family and my girlfriend very much for their great spiritual and economic support.

References

[1] P. Balaz, M. Achimovicova, M. Balaz, P. Billik, Z. Cherkezova-Zheleva, J.M. Criado, F. Delogu, E. Dutkova, E. Gaffet, F.J. Gotor, R. Kumar, I. Mitov, T. Rojac, M. Senna, A. Streletskii and K. Wieczorek-Ciurowa, Chem. Soc. Rev. **42**, 7571 (2013).

[2] X. Liu, E.K. Akdogan, A. Safari and R.E. Riman, Appl. Phys. A **81**, 531 (2005).

[3] K. Kubota, Y. Pang, A. Miura and H. Ito, Science **366**, 1500 (2019).

[4] Y. Pang, J. W. Lee, K. Kubota and H. Ito, Angew. Chem. Int. Ed. Engl. **59**, 22570 (2020).

[5] K. Užarević, V. Štrukil, C. Mottillo, P.A. Julien, A. Puškarić, T. Friščić and I. Halasz, Cryst. Growth Des. **16**, 2342 (2016).

[6] L. Kong, J. Ma, H. Huang, W. Zhu and O. Tan, Mater. Lett. **50**, 129 (2001).

[7] J. Xue, D. Wan, S. E. Lee and J. Wang, J. Am. Ceram. Soc. **82**, 1687 (1999).

[8] L. B. Kong, T. S. Zhang, J. Ma and F. Boey, Prog. Mater. Sci. **53**, 207 (2008).

[9] S. F. Wang, Y. R. Wang, T. Mahalingam, J.P. Chu and K.U. Lin, Mater. Chem. Phys. **87**, 53 (2004).

[10] S. Linardos, Q. Zhang and J.R. Alcock, J. Eur. Ceram. Soc. **26**, 117 (2006).

[11] M. Veith, M. Bender, T. Lehnert, M. Zimmer and A. Jakob, Dalton Trans. **40**, 1175 (2011).

[12] M. Oikawa and K. Toda, Appl. Phys. Lett. **29**, 491 (1976).

[13] R. Frunza, D. Ricinschi, F. Gheorghiu, R. Apetrei, D. Luca, L. Mitoseriu and M. Okuyama, J. Alloys Compd. **509**, 6242 (2011).

[14] J. R. Gatabi, S. Rahman, A. Amaro, T. Nash, J. Rojas-Ramirez, R. Pandey and R. Droopad, Ceram. Int. **43**, 6008 (2017).

[15] R. Kagimura and D.J. Singh, Phys. Rev. B **77**, 104113 (2008).

[16] M. A. Khan, M.A. Nadeem and H. Idriss, Surf. Sci. Rep. **71**, 1 (2016).

[17] G. Liu, S. Zhang, W. Jiang and W. Cao, Mater. Sci. Eng., R **89**, 1 (2015).

[18] S. Zhang and F. Li, J. Appl. Phys. **111**, 031301 (2012).

[19] T. R. Shrout and S.J. Zhang, J. Electroceram. **19**, 113 (2007).

[20] M. D. Nguyen, E. P. Houwman and G. Rijnders, Sci. Rep. **7**, 12915 (2017).

[21] D. S. L. Pontes, L. Gracia, F.M. Pontes, A. Beltrán, J. Andrés and E. Longo, J. Mater. Chem. **22**, 6587 (2012).

[22] Q.-M. Wang, Y. Ding, Q. Chen, M. Zhao and J. Cheng, Appl. Phys. Lett. **86**, 162903 (2005).

[23] M. Zheng, Y. Hou, S. Wang, C. Duan, M. Zhu, H. Yan and C. Randall, J. Am. Ceram. Soc. **96**, 2486 (2013).

[24] G. Shilpa, K. Sreelakshmi and M. Ananthaprasad: IOP Conference Series, Mater. Sci. Eng. **149**, 012190 (2016).

[25] J. Valasek, Phys. Rev. **17**, 475 (1921).

[26] H. D. Megaw, Proc. Phys. Soc. **58**, 133 (1946).

[27] E. J. Huibregtse, D. Barker and G. Danielson, Phys. Rev. **84**, 142 (1951).

[28] Y. Kuroiwa, S. Aoyagi, A. Sawada, J. Harada, E. Nishibori, M. Takata and M. Sakata, Phys. Rev. Lett. **87**, 217601 (2001).

[29] S. J. Kim, C. Moriyoshi, S. Kimura, Y. Kuroiwa, K. Kato, M. Takata, Y. Noguchi and M. Miyayama, Appl. Phys. Lett. **91**, 062913 (2007).

[30] H. Kay and P. Bailey, Acta Crystallogr. **10**, 219 (1957).

[31] J. F. Dorrian, R. E. Newnham, D. K. Smith and M. I. Kay, Ferroelectrics **3**, 17 (1972).

[32] A. D. Rae, J. G. Thompson, R. Withers and A. C. Willis, Acta Crystallogr., Sect. B: Struct. Sci. **46**, 474 (1990).

[33] M. Krzhizhanovskaya, S. Filatov, V. Gusarov, P. Paufler, R. Bubnova, M. Morozov and D.C. Meyer, Zeitschrift für anorganische und allgemeine Chemie. **631**, 1603 (2005).

[34] C. H. Hervoches and P. Lightfoot, Chem. Mater. **11**, 3359 (1999).

[35] Q. Zhou, B.J. Kennedy and C.J. Howard, Chem. Mater. **15**, 5025 (2003).

[36] J. C. Slater, Phys. Rev. **78**, 748 (1950).

[37] J. Axe, Phys. Rev. **157**, 429 (1967).

[38] R. E. Cohen and H. Krakauer, Ferroelectrics **136**, 65 (1992).

[39] X. Ye, J. Zhao, H. Das, D. Sheptyakov, J. Yang, Y. Sakai, H. Hojo, Z. Liu, L. Zhou, L. Cao, T. Nishikubo, S. Wakazaki, C. Dong, X. Wang, Z. Hu, H.J. Lin, C.T. Chen, C. Sahle, A. Efiminko, H. Cao, S. Calder, K. Mibu, M. Kenzelmann, L.H. Tjeng, R. Yu, M. Azuma, C. Jin and Y. Long, Nat. Commun. **12**, 1917 (2021).

[40] Y. Sakai, J. Yang, R. Yu, H. Hojo, I. Yamada, P. Miao, S. Lee, S. Torii, T. Kamiyama, M. Lezaic, G. Bihlmayer, M. Mizumaki, J. Komiyama, T. Mizokawa, H. Yamamoto, T. Nishikubo, Y. Hattori, K. Oka, Y. Yin, J. Dai, W. Li, S. Ueda, A. Aimi, D. Mori, Y. Inaguma, Z. Hu, T. Uozumi, C. Jin, Y. Long and M. Azuma, J. Am. Chem. Soc. **139**, 4574 (2017).

[41] C. Qiu, B. Wang, N. Zhang, S. Zhang, J. Liu, D. Walker, Y. Wang, H. Tian, T.R. Shrout, Z. Xu, L. Q. Chen and F. Li, Nature **577**, 350 (2020).

[42] R. D. Shannon, Acta Crystallogr., Sect. A: Cryst. Phys., Diffr., Theor. Gen. Crystallogr. **32**, 751 (1976).

[43] X. Liu, R. Hong and C. Tian, J. Mater. Sci.: Mater. Electron. **20**, 323 (2008).

[44] H. Yu, Z. Qingchun, L. Shengguo, Z. Qifa, Z. Lingying and Y. Xi, Ferroelectrics **156**, 153 (1994).

[45] J. Ryu, G. Han, T.K. Song, A. Welsh, S. Trolier-McKinstry, H. Choi, J.P. Lee, J.W. Kim, W.H. Yoon, J.J. Choi, D.S. Park, C.W. Ahn, S. Priya, S.Y. Choi and D.Y. Jeong, ACS Appl. Mater. Interfaces **6**, 11980 (2014).

[46] G. A. Rossetti Jr, L. E. Cross and K. Kushida, Appl. Phys. Lett. **59**, 2524 (1991).

[47] E. T. Ritz and N. A. Benedek, Phys. Rev. Lett. **121**, 255901 (2018).

[48] Z. Pan, J. Chen, R. Yu, L. Patra, P. Ravindran, A. Sanson, R. Milazzo, A. Carnera, L. Hu, L. Wang, H. Yamamoto, Y. Ren, Q. Huang, Y. Sakai, T. Nishikubo, T. Ogata, X.a. Fan, Y. Li, G. Li, H. Hojo, M. Azuma and X. Xing, Chem. Mater. **31**, 1296 (2019).

[49] J. Chen, K. Nittala, J.S. Forrester, J.L. Jones, J. Deng, R. Yu and X. Xing, J. Am. Chem. Soc. **133**, 11114 (2011).

[50] R. E. Cohen, Nature **358**, 136 (1992).

[51] J. D. Axe, Phys. Rev. **157**, 429 (1967).

[52] T. Abe, S. Kim, C. Moriyoshi, Y. Kitanaka, Y. Noguchi, H. Tanaka and Y. Kuroiwa, Appl. Phys. Lett. **117**, 252905 (2020).

[53] Y. Y. Guo, A. S. Gibbs, J. M. Perez-Mato and P. Lightfoot, IUCrJ. **6**, 438 (2019).

[54] J. M. Perez-Mato, P. Blaha, K. Schwarz, M. Aroyo, D. Orobengoa, I. Etxebarria and A. García, Phys. Rev. B **77**, 184104 (2008).

[55] N. Setter, D. Damjanovic, L. Eng, G. Fox, S. Gevorgian, S. Hong, A. Kingon, H. Kohlstedt, N. Park and G. Stephenson, J. Appl. Phys. **100**, 051606 (2006).

[56] Y. Wang, H. Zhao, L. Zhang, J. Chen and X. Xing, Phys. Chem. Chem. Phys. **19**, 17493 (2017).

[57] P. Gao, Z. Zhang, M. Li, R. Ishikawa, B. Feng, H.J. Liu, Y.L. Huang, N. Shibata, X. Ma, S. Chen, J. Zhang, K. Liu, E.G. Wang, D. Yu, L. Liao, Y.H. Chu and Y. Ikuhara, Nat. Commun. **8**, 15549 (2017).

[58] H. J. Lee, E.-J. Guo, J. H. Kwak, S. H. Hwang, K. Dörr, J. H. Lee and J. Young Jo, Appl. Phys. Lett. **110**, 032901 (2017).

[59] L.W. Martin, Y.H. Chu and R. Ramesh, Mater. Sci. Eng., R **68**, 89 (2010).

[60] L. Li, L. Miao, Z. Zhang, X. Pu, Q. Feng, K. Yanagisawa, Y. Fan, M. Fan, P. Wen and D. Hu, J. Mater. Chem. A **7**, 16046 (2019).

[61] L. Yang, D.-Y. Zheng, K.-X. Guo, W.-N. Zhao, Z.-H. Peng, G.-G. Peng and T. Zhou, J. Mater. Sci.: Mater. Electron. **29**, 18011 (2018).

[62] M.-G. Kang, M.-S. Noh, J.J. Pyeon, W.-S. Jung, H.G. Moon, S.-H. Baek, S. Nahm, S.-J. Yoon and C.-Y. Kang, Chem. Mater. **32**, 6483 (2020).

[63] C. Kwamen, M. Rössle, W. Leitenberger, M. Alexe and M. Bargheer, Appl. Phys. Lett. **114**, 162907 (2019).

[64] H. Zhao, X. Peng, L. Zhang, J. Chen, W. Yan and X. Xing, Appl. Phys. Lett. **103**, 082904 (2013).

[65] S. Cheng, C. Kam, Y. Zhou, W. Que, Y. Lam, Y. Chan and W. Gan, Thin Solid Films **375**, 109 (2000).

[66] T. Ohno, B. Malič, M. Kosec, N. Wakiya, H. Suzuki and T. Matsuda, Trans. Mater. Res. Soc. Jpn. **34**, 113 (2009).

[67] S.-H. Lee, H.M. Jang, S.M. Cho and G.-C. Yi, Appl. Phys. Lett. **80**, 3165 (2002).

[68] F. Borodavka, I. Gregora, A. Bartasyte, S. Margueron, V. Plausinaitiene, A. Abrutis and J. Hlinka, J. Appl. Phys. **113**, 187216 (2013).

[69] D. D. Fong, A.M. Kolpak, J.A. Eastman, S.K. Streiffer, P.H. Fuoss, G.B. Stephenson, C. Thompson, D.M. Kim, K.J. Choi, C.B. Eom, I. Grinberg and A.M. Rappe, Phys. Rev. Lett. **96**, 127601 (2006).

[70] T. Abe, L. Wu, C. Moriyoshi, Y. Kuroiwa, M. Suzuki, K. Shinoda, R. Aoyagi and J. Akedo, Jpn. J.Appl. Phys. **59**, SPPA04 (2020).

[71] J. Akedo, J. Am. Ceram. Soc. **89**, 1834 (2006).

[72] J. Akedo, J. Therm. Spray Technol. **17**, 181 (2008).

[73] J. Akedo, J.-H. Park and Y. Kawakami, Jpn. J.Appl. Phys. **57**, 07LA02 (2018).

[74] M. Lebedev, J. Akedo and T. Ito, J. Cryst. Growth **275**, e1301 (2005).

[75] N. Seto, K. Endo, N. Sakamoto, S. Hirose and J. Akedo, J. Therm. Spray Technol. **23**, 1373 (2014).

[76] M. Schubert, N. Leupold, J. Exner, J. Kita and R. Moos, J. Therm. Spray Technol. **27**, 870 (2018).

[77] R. Sakamaki, T. Hoshina, H. Kakemoto, K. Yasuda, H. Takeda, J. Akedo and T. Tsurumi, J. Ceram. Soc. Jpn. **116**, 1299 (2008).

[78] J. Akedo and M. Lebedev, Appl. Phys. Lett. **77**, 1710 (2000).

[79] N.H. Khansur, U. Eckstein, K. Riess, A. Martin, J. Drnec, U. Deisinger and K.G. Webber, Scr. Mater. **157**,86 (2018).

[80] M. Nakada, K. Ohashi and J. Akedo, Jpn. J. Appl. Phys. **44**, 6918 (2005).

[81] M. Suzuki, J. Ceram. Soc. Jpn. **123**, 9 (2015).

[82] K. Iijima, Y. Tomita, R. Takayama and I. Ueda, J. Appl. Phys. **60**, 361 (1986).

[83] Y. F. Chen, T. Yu, J.X. Chen, L. Shun, P. Li and N.B. Ming, Appl. Phys. Lett. **66**, 148 (1995).

[84] M. Kojima, M. Okuyama, T. Nakagawa and Y. Hamakawa, Jpn. J. Appl. Phys. **22**, 14 (1983).

[85] T. Morita and Y. Cho, J. Korean Phys. Soc. **46**, 10 (2005).

[86] G. Vats, H.S. Kushwaha, R. Vaish, N.A. Madhar, M. Shahabuddin, J.M. Parakkandy and K.M. Batoo, J. Adv. Dielectr. **04**, 1450029 (2014).

[87] M. Suzuki, T. Tsuchiya and J. Akedo, Jpn. J. Appl. Phys. **56**, 06GH02 (2017).

[88] S. Teslic and T. Egami, Acta Crystallogr., Sect. B: Struct. Sci. **54**, 750 (1998).

[89] M.F. Kuprianov, S.M. Zaitsev, E.S. Gagarina and E.G. Fesenko, Phase Transitions **4**, 55 (2006).

[90] H. Fujishita, Y. Ishikawa, S. Tanaka, A. Ogawaguchi and S. Katano, J. Phys. Soc. Jpn. **72**, 1426 (2003).

[91] Z. G. Fthenakis and I. Ponomareva, Phys. Rev. B **96**, 184110 (2017).

[92] A. K. Tagantsev, K. Vaideeswaran, S.B. Vakhrushev, A.V. Filimonov, R.G. Burkovsky, A. Shaganov, D. Andronikova, A.I. Rudskoy, A.Q. Baron, H. Uchiyama, D. Chernyshov, A. Bosak, Z. Ujma, K. Roleder, A. Majchrowski, J.H. Ko and N. Setter, Nat. Commun. **4**, 2229 (2013).

[93] P. Vales-Castro, R. Faye, M. Vellvehi, Y. Nouchokgwe, X. Perpiñà, J.M. Caicedo, X. Jordà, K. Roleder, D. Kajewski, A. Perez-Tomas, E. Defay and G. Catalan, Phys. Rev. B **103**, 054112 (2021).

[94] A. Glazer, K. Roleder and J. Dec, Acta Crystallogr., Sect. B: Struct. Sci. **49**, 846 (1993).

[95] S. Aoyagi, Y. Kuroiwa, A. Sawada, H. Tanaka, J. Harada, E. Nishibori, M. Takata and M. Sakata, J. Phys. Soc. Jpn. **71**, 2353 (2002).

[96] R. Gao, S.E. Reyes-Lillo, R. Xu, A. Dasgupta, Y. Dong, L.R. Dedon, J. Kim, S. Saremi, Z. Chen, C.R. Serrao, H. Zhou, J.B. Neaton and L.W. Martin, Chem. Mater. **29**, 6544 (2017).

[97] J. A. Rodriguez, A. Etxeberria, L. González and A. Maiti, J. Chem. Phys. **117**, 2699 (2002).

[98] M. Soares, A. Senos and P. Mantas, J. Eur. Ceram. Soc. **20**, 321 (2000).

[99] J. Joseph, T. Vimala, V. Sivasubramanian and V. Murthy, J. Mater. Sci. **35**, 1571 (2000).

[100]S. N. Kallaev, G.G. Gadzhiev, I.K. Kamilov, Z.M. Omarov, S.A. Sadykov and L.A. Reznichenko, Phys. Solid State **48**, 1169 (2006).

[101]B. Noheda, J. Gonzalo, L. Cross, R. Guo, S.-E. Park, D. Cox and G. Shirane, Phys. Rev. B **61**, 8687 (2000).

[102]N. Sahu, S. Panigrahi and M. Kar, Adv. Powder Technol. **22**, 689 (2011).

[103]A. Bouzid, E.M. Bourim, M. Gabbay and G. Fantozzi, J. Eur. Ceram. Soc. **25**, 3213 (2005).

[104]D. M. Hatch, H.T. Stokes, R. Ranjan, Ragini, S.K. Mishra, D. Pandey and B.J. Kennedy, Phys. Rev. B **65**, 212101 (2002).

[105]S. Lee, J. Xue, D. Wan and J. Wang, Acta Mater. **47**, 2633 (1999).

[106]F. Bortolani and R.A. Dorey, J. Eur. Ceram. Soc. **30**, 2073 (2010).

[107]K. Raju and P. Venugopal Reddy, Curr. Appl. Phys. **10**, 31 (2010).

[108]Z. Branković, G. Branković, Č. Jovalekić, Y. Maniette, M. Cilense and J.A. Varela, Mater. Sci. Eng. A **345**, 243 (2003).

[109]L. Kong, J. Ma, W. Zhu and O. Tan, J. Mater. Sci. Lett. **21**, 25 (2002).

[110]S. Kawaguchi, M. Takemoto, K. Osaka, E. Nishibori, C. Moriyoshi, Y. Kubota, Y. Kuroiwa and K. Sugimoto, Rev. Sci. Instrum. **88**, 085111 (2017).

[111]G. Rosenbaum, K.C. Holmes and J. Witz, Nature **230**, 434 (1971).

[112]S. Ueno, A. Minato, H. Seto, Y. Amemiya and K. Sato, J. Phys. Chem. B **101**, 6847 (1997).

[113]Y. Meng, R. Hrubiak, E. Rod, R. Boehler and G. Shen, Rev. Sci. Instrum. **86**, 072201 (2015).

[114]H. Cheng, C. Lu, J. Liu, Y. Yan, X. Han, H. Jin, Y. Wang, Y. Liu and C. Wu, Prog. Nat. Sci. **27**, 66 (2017).

[115]F. Izumi and T. Ikeda, Mater. Sci. Forum **321**, 198 (2000).

[116]R. Hill and C. Howard, J. Appl. Crystallogr. **20**, 467 (1987).

[117]D. T. Wiles and R. Young, J. Appl. Crystallogr. **14**, 149 (1981).

[118]Q. Zhao, T. Abe, C. Moriyoshi, S. Kim, A. Taguchi, H. Moriwake, H.-T. Sun and Y. Kuroiwa, J. Appl. Phys. **59**, 095505 (2020).

[119]H. Rietveld, Acta Crystallogr. **22**, 151 (1967).

[120]H. M. Rietveld, J. Appl. Crystallogr. **2**, 65 (1969).

[121]C. E. Shannon, Bell Syst. Tech. J. **27**, 379 (1948).

[122]C .E. Shannon, Proc. IRE **37**, 10 (1949).

[123]R. Willingale, Mon. Notices Royal Astron. Soc. **194**, 359 (1981).

[124]M. Takata, Acta Crystallogr. A **64**, 232 (2008).

[125]M. Sakata and M. Sato, Acta Crystallogr. A **46**, 263 (1990).

[126]K. Kato and H. Tanaka, Adv. Phys.: X **1**, 55 (2016).

[127]R. De Vries, W.J. Briels and D. Feil, Acta Crystallogr. A **50**, 383 (1994).

[128]K. Huang, Proc. Roy. Soc. Lond A **190**, 102, (1947).

[129]H. Peisl, H. Spalt and W. Waidelich, Phys. Stat. Sol. **23**, K75 (1967).

[130]D. Nath, F. Singh and R. Das, Mater. Chem. Phys. **239**, 122021 (2020).

[131]V. Mote, Y. Purushotham and B. Dole, J. Theor. Appl. Phys. **6**, 1 (2012).

[132]Y. Tang, Y. Zhu, X. Ma, Z. Hong, Y. Wang, W. Wang, Y. Xu, Y. Liu, B. Wu, L. Chen, C. Huang, L. Chen, Z. Chen, H. Wu and S.J. Pennycook, Adv. Funct. Mater. **29**, 1901687 (2019).

[133]L. Sun, Y.F. Chen, W.H. Ma, L.W. Wang, T. Yu, M.S. Zhang and N.B. Ming, Appl. Phys. Lett. **68**, 3728 (1996).

[134]C. Lu, A. Kuang and G. Huang, J. Appl. Phys. **80**, 202 (1996).

[135]K. Kushida and H. Takeuchi, Appl. Phys. Lett. **50**, 1800 (1987).

[136]H. Tabata, O. Murata, T. Kawai, S. Kawai and M. Okuyama, Appl. Phys. Lett. **64**, 428 (1994).

[137]R. M. Wood and G.J. Palenik, Inorg. Chem. **37**, 4149 (1998).

[138]W. Liu and H.H. Thorp, Inorg. Chem. **32**, 4102 (1993).

[139]N. Sicron, B. Ravel, Y. Yacoby, E.A. Stern, F. Dogan and J.J. Rehr, Phys. Rev. B **50**, 13168 (1994).

[140]L. Zhang, J. Chen, L. Fan, O. Dieguez, J. Cao, Z. Pan, Y. Wang, J. Wang, M. Kim, S. Deng, J. Wang, H. Wang, J. Deng, R. Yu, J.F. Scott and X. Xing, Science. **361**, 494 (2018).

[141]M. De Keijser, G. Dormans, P. Van Veldhoven and D. De Leeuw, Appl. Phys. Lett. **59**, 3556 (1991).

[142]N. Zhang, H. Yokota, A.M. Glazer, Z. Ren, D.A. Keen, D.S. Keeble, P.A. Thomas and Z.G. Ye, Nat. Commun. **5**, 5231 (2014).

[143]F. Cordero, F. Trequattrini, F. Craciun and C. Galassi, J. Phys.: Condens. Matter **23**, 415901 (2011).